Tailored synchrotron light pulses in the THz domain

Dissertation

zur Erlangung des Grades eines
Doktors der Naturwissenschaften
(Dr. rer. nat.)

vorgelegt
der Fakultät Physik
der Technischen Universität Dortmund
von

Carsten Mai

2025

Datum der Prüfung: 27. Oktober 2025
Vorsitzender der Prüfungskommission: Prof. Dr. Markus Betz
Erstgutachter: Prof. Dr. Shaukat Khan
Zweitgutachter: Prof. Dr. Andreas Jankowiak
weiteres Mitglied der Prüfungskommission: JProf. Dr. Benedikt Fauseweh

Zusammenfassung

Bei DELTA, dem 1,5-GeV-Elektronen-Speicherring, der von der TU Dortmund als Synchrotronstrahlungsquelle betrieben wird, wird die Ablenkung eines hochrelativistischen Elektronenstrahls genutzt, um Strahlung im Spektralbereich des harten Röntgenbereichs bis zum Terahertz (THz)-Bereich zu erzeugen. Die Kurzpulsquelle von DELTA stellt auf der Basis einer Laser-Elektronen-Wechselwirkung Pulse im Vakuum-Ultraviolett (VUV) und THz-Bereich bereit. Im Rahmen dieser Arbeit wurde die Erzeugung von THz-Strahlung systematisch in Experimenten und Simulationen untersucht. Der Frequenzbereich zwischen Radiowellen und Infrarotstrahlung wurde lange Zeit als Terahertz-Lücke bezeichnet, da die Verfügbarkeit von Quellen und Detektoren sehr begrenzt war. Heutzutage haben Teilchenbeschleuniger und moderne Lasertechnologie begonnen, die Lücke der THz-Quellen zu schließen. Bei DELTA wurde die Kurzpulsquelle um die Möglichkeit erweitert, THz-Pulse von nahezu beliebiger spektro-temporaler Form zu erzeugen. Hierbei moduliert ein Titan-Saphir-Kurzpulslaser die Elektronenenergie innerhalb eines Teils des Elektronenpakets mittels einer Laser-Elektronen-Wechselwirkung in einem Undulator. Die dispersiven Eigenschaften des Speicherrings führen zur Bildung einer Senke in der longitudinalen Elektronendichte. Dies führt zu einer kohärenten Emission von Synchrotronstrahlung im THz-Bereich. Während die Wechselwirkung mit einem ultrakurzen Laserpuls zu einer breitbandigen Emission von THz-Strahlung führt, führt ein längerer Laserpuls mit einem periodischen zeitlichen Profil zu einer schmalbandigen Emission. Um dies zu realisieren, wurde durch Interferenz des gechirpten Laserpulses mit einer verzögerten Kopie eine Intensitäts-Schwebung des Laserpulses erzeugt. Durch eine Änderung der Schwebungsfrequenz kann die zentrale Frequenz des emittierten THz-Spektrums zwischen $50\,\mathrm{GHz}$ und $6.5\,\mathrm{THz}$ mit einer relativen Bandbreite von etwa $10\,\%$ eingestellt werden. In einem nächsten Schritt wurde eine direkte Manipulation der spektralen Phase der Laserpulse mit einem Flüssigkristall-basierten räumlichen Lichtmodulator implementiert, der es erlaubt, die Laserpulse nahezu beliebig zu formen. Auf diese Weise konnte durchstimmbare schmalbandige THz-Strahlung mit einer noch besseren relativen Bandbreite von unter $2\,\%$ erzeugt werden. Außerdem wurden zweifarbige Pulse und Spektren mit rechteckigem und trapezförmigem Spektrum erzeugt. Die Messungen der spektralen Eigenschaften wurden mit einem im Rahmen dieser Arbeit in Betrieb genommenen Fourier-Transformations-Spektrometer durchgeführt. Neben der spektralen Formung von THz-Pulsen wurde auch die zeitliche Entwicklung der laserinduzierten Energiemodulation untersucht. Reste der Energiemodulation wurden für mehr als 350 Umläufe im Speicherring aufgezeichnet, nachdem die ursprüngliche Laser-Elektronen-Wechselwirkung stattgefunden hatte.

Abstract

At DELTA, a 1.5-GeV electron storage ring operated as a synchrotron light source by the TU Dortmund University, the deflection of a highly relativistic electron beam is used to generate radiation in the spectral range from hard X-rays to terahertz (THz) radiation. The short-pulse facility of DELTA provides pulses in the vacuum ultra violet (VUV) and THz range based on a laser-electron interaction. Within the scope of this thesis, the generation of THz radiation was systematically studied in experiments and simulations. The frequency range between radio waves and infrared radiation has been referred to as the terahertz gap for a long time because the availability of sources and detectors was very limited. Nowadays, particle accelerators and modern laser technology have started to close the gap. At DELTA, the short-pulse facility was improved by the ability to generate THz pulses of nearly arbitrary shape. Here, a short-pulse Ti:sapphire laser modulates the electron energy within a slice of the electron bunch via a laser-electron interaction in an undulator. The dispersive properties of the storage ring lead to the formation of a dip in the longitudinal electron density which gives rise to the coherent emission of synchrotron radiation in the THz regime. While an interaction with an ultrashort laser pulse leads to a broadband emission of THz radiation, a longer laser pulse with a periodic temporal profile leads to a narrowband emission. To realize that, an intensity beating of the laser pulse was generated by interference of the chirped laser pulse with a delayed copy. Here, a change of the beating frequency allows to control the central frequency of the emitted THz spectrum ranging between $50\,\mathrm{GHz}$ and $6.5\,\mathrm{THz}$ with a relative bandwidth of about $10\,\%$. In a next step, a direct manipulation of the spectral phase of the laser pulses was implemented using a liquid-crystal based spatial light modulator, allowing to almost arbitrarily shape the laser pulses. Using this setup, tunable narrowband THz radiation with an improved relative bandwidth below $2\,\%$ was generated. Furthermore, two-colored pulses and spectra of rectangular and trapezoidal shape were produced. Measurements of the spectral properties were conducted using a Fourier-transform spectrometer commissioned within the scope of this thesis. Besides the spectral shaping of THz pulses, the temporal evolution of the laser-induced energy modulation was explored. Remainders of the energy modulation were recorded after more than 350 revolutions in the storage ring after the initial laser-electron interaction had happened.

Contents

1 Introduction

Shortly after the invention of the laser by Maiman in 1960 [1], it was experimentally shown that certain materials change their optical properties in the presence of intense light. Franken et al. [2] generated electric fields of $10^7\,\mathrm{V/m}$ by focusing the light of a ruby laser in crystalline quartz and were able to emit light at the second harmonic of the original wavelength – an effect that strongly depends on the laser intensity. This frequency doubling from $694.3\,\mathrm{nm}$ to $347.2\,\mathrm{nm}$ was the first experimental use of the nonlinear behavior of dielectrics, like crystalline quartz, exposed to high electric fields. Later, the peak electric field of laser sources was drastically increased by the invention of pulsed lasers in mode-locked operation. Notably, the titanium-sapphire (Ti:sapphire) laser, invented in 1982 [3] by Moulton, and the amplification of chirped pulses (CPA) [4] were important contributions. Changing the wavelength over a wide range and introducing pulsed operation opened up many new applications for laser radiation.

At about the same time as laser technology made these major discoveries, another emerging field of physics entered a new era. Although the acceleration of charged particles had already been pioneered in 1928 with Wideröe's invention of the linear accelerator [5] at RWTH Aachen University, it was not until 1967 that the first circular electron storage ring dedicated to the production of intense electromagnetic radiation, the Tantalus [6] ring, was built. The demand for this type of light source arose from the advantages of synchrotron light regarding wavelength range and intensity for spectroscopy and diffraction experiments. Several early accelerator facilities had served as sources for synchrotron radiation in parasitic operation for users from materials science and condensed-matter physics before. Lasers and synchrotron light sources are both used to generate intense, short light pulses with photon energies in the soft-X-ray range and above. Synchrotron radiation was theoretically predicted as early as 1944 [7], and it was known that the radiation spectrum ranges from the far infrared regime to hard X-rays. Today, free-electron lasers (FELs) at modern linear electron accelerators offer the possibility to generate short and intense X-ray pulses.

Although the doubling of the photon energy of laser radiation was demonstrated shortly after the invention of the laser, it took much longer for laser technology to reach considerably higher harmonics. Today, it is possible to increase the photon energy of an

ultrashort laser pulse by at least two orders of magnitude [8, 9] by applying the so-called high-harmonic generation scheme (HHG). In this process, an intense ultrashort laser pulse is focused into a gas or plasma target. If the peak electric field of the laser pulse is comparable to the binding electric field within a single atom, the probability of an electron leaving the atom by tunneling is non-zero. The subsequent radiative recombination of the electron and ion is supported by the laser after the electric field changes its sign. In recombination, both the kinetic energy of the electron and the ionization potential contribute to the energy of the emitted photon. Since this process can occur after each of the two field extrema per laser cycle, only odd harmonics of the laser frequency are generated for symmetry reasons [10]. Laser-based sources employing the HHG scheme serve as table-top soft-X-ray sources, today [11].

A few years ago, a process very similar to HHG was observed with photons of much lower energy. In an experiment by Zaks et al. [12], terahertz (THz) radiation was used to manipulate excitons that were created in a semiconductor by a near-infrared (NIR) continuous-wave (CW) laser. Excitons are bound states of an electron and an electron hole that attract each other by the Coulomb force [13]. In many ways, their arrangement behaves like a hydrogen atom if the temperature is well below $10\,\mathrm{K}$ and thermal excitation is negligible [14]. However, the binding energy is in the meV range, which allows field-induced ionization [15] with photons of that energy, i.e., THz radiation. Similar to the generation of high harmonics by intense laser pulses, Zaks et al. observed many THz sidebands to harmonics of the driving NIR laser with slowly decreasing intensity. In contrast to the HHG process, the harmonics arise as integer sidebands of the NIR radiation used to create the excitons. This process is called harmonic-sideband generation (HSG). These high-order sidebands imprint an ultrafast modulation onto the continuous-wave NIR light. Combining the concept of harmonic sideband generation with fast electronic switches allows the development of ultrafast modulators of NIR light for data transmission at rates of terabits per second in future optical communication systems. Zaks et al. carried out their experiment at the THz FEL of the University of California, Santa Barbara (UCSB) [16]. In the THz regime, FELs are among the most flexible radiation sources, since high pulse energies above the microjoule level and wavelength tunability are achieved [17]. Further infrared FELs are, for example, CLIO [18] in France, FELIX [19] in the Netherlands, FELBE [20] and FHI-FEL [21] in Germany, NovoFEL [22] in Russia, KAERI-FEL [23] in Korea, and ISIR FEL [24] in Japan. Usually, FELs provide few beamlines per facility, and the beam time requests by users far exceed the availability. On the other hand, table-top sources based on laser difference-frequency generation exist, but they cannot supply frequency-tunable radiation in a range [25] as wide as that supplied by FELs. Therefore, additional concepts

for THz generation are needed, which provide wavelength tunability or even allow the control of the spectro-temporal pulse properties in an arbitrary manner.

The diversity of different radiation sources proves that the manipulation of pulse length and spectrum is crucial for the study of matter in physics, chemistry, biology, and other research fields. In this thesis, two technological achievements – a modern short-pulse laser and an electron accelerator facility – were combined to develop a frequency-tunable THz source. At the electron storage ring DELTA, operated by the TU Dortmund University, the short-pulse facility was commissioned in 2011 [26]. Here, the intense electric field of a short laser pulse is used to modulate the energy of a fraction of the electrons within a bunch in the storage ring. The working principles of particle accelerators and modern lasers are discussed in greater detail in Chap. 2 of this thesis. A detailed description of how this energy modulation from a laser-electron interaction leads to the coherent emission of THz radiation and vacuum-ultraviolet (VUV) radiation is provided in Chap. 3. To analyze the properties of the THz source, a spectrometer based on a polarizing Michelson interferometer – a so-called Martin-Puplett interferometer [169] – was designed and commissioned. The characteristics of this device are explained in Chap. 4. The tunable THz source relies on precise control of the laser pulse shape. Different approaches to induce a temporal modulation of the laser intensity, based on an interferometer and a modern, computer-controlled spatial light modulator, are covered in Chap. 5. Measurements of nearly arbitrarily shaped THz spectra are presented. Furthermore, the optical diagnostics used to detect and tune the desired pulse shape are explained. In addition to the goal of implementing a highly flexible THz source, the radiation process also provides insight into the longitudinal dynamics of the electrons in the storage ring, which is discussed in Chap. 6. Prospective applications of the source and possible further improvements are described in Chap. 7. More detailed information on device parameters and mathematical derivations can be found in the appendices.

2 Basic concepts

The experiments described in this thesis use various techniques from accelerator physics, laser physics as well as generation and detection of terahertz (THz) radiation. An introduction to the relevant concepts of these fields is given in this Chapter.

2.1 Relativistic electrons in storage rings

As pointed out in Chap. 1, particle accelerators have become versatile research tools for many fields in physics, but also affect our every day life in medical applications. Large particle colliders, being many kilometers long, nowadays dominate particle physics research [27]. On the other hand, more than 50 accelerator facilities [28] exist which are dedicated to the generation of synchrotron light. An in-depth view of the physics of particle accelerators can be found in [29,30]. In the following sections, a brief overview of the physics of electrons in storage rings of synchrotron light sources is given. In electron storage rings, the motion of the particles is confined to a closed path by external magnetic fields. The intention is to store the electrons, which form a beam, for many hours. Moving almost with the velocity of light c, their total energy E_{tot} exceeds their rest energy E_{r} by far. In the relativistic description of the electron properties, this is expressed by the Lorentz factor

$$\gamma = E_{\mathrm{tot}}/E_{\mathrm{r}} \qquad \text{with} \qquad E_{\mathrm{r}} = m_0 c^2 \tag{2.1}$$

and m_0 denoting the rest mass of the electron. The Lorentz force

$$\vec{F}_{\mathrm{L}} = -e\,(\vec{\mathcal{E}} + \vec{v} \times \vec{\mathcal{B}}) \tag{2.2}$$

determines the motion of electrons in a storage ring. Here, $\vec{\mathcal{E}}$ is the electric field, $\vec{\mathcal{B}}$ is the magnetic field, $\vec{v}$ is the electron velocity and e is the elementary charge. In natural units, the velocity is expressed as $\beta = v/c$.

2.1.1 Transverse Beam Dynamics

The position of each electron can be described by the coordinates x, y and z in a co-moving frame which is also known as the Frenet-Serret coordinate system [31, 32]. As shown in Fig. 2.1, x and y describe the transverse deviation of the electron from a reference particle and the longitudinal position along this reference orbit (green) is given by s. The reference orbit is defined by an imagined reference electron about which all other electrons oscillate transversely and longitudinally.

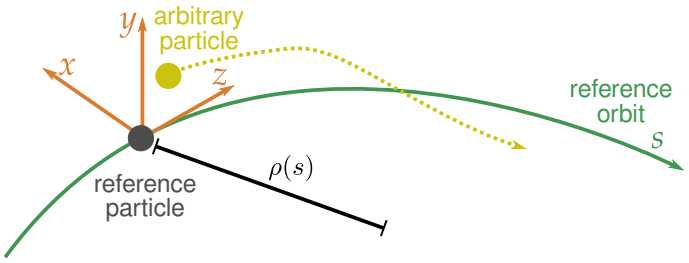

Figure 2.1: The Frenet-Serret coordinate system describes the position of the electron in a co-moving coordinate system as the relative deviation from an ideal particle following the orbit.

A common way to define the properties of an electron is the six-dimensional vector

$$\vec{X}_s = \begin{pmatrix} x \\ x' = \frac{\mathrm{d}x}{\mathrm{d}s} \\ y \\ y' = \frac{\mathrm{d}y}{\mathrm{d}s} \\ z \\ \Delta p/p_0 \end{pmatrix} \widehat{=} \begin{pmatrix} \text{horizontal displacement} \\ \text{horizontal angle} \\ \text{vertical displacement} \\ \text{vertical angle} \\ \text{longitudinal displacement} \\ \text{relative momentum deviation} \end{pmatrix} . \tag{2.3}$$

The transformation of $\vec{X}_{s_0}$ from a position s_0 to s_1 is described by the 6×6-matrix

$$\begin{pmatrix} x \\ x' \\ y \\ y' \\ z \\ \Delta p/p_0 \end{pmatrix}_{s_1} = \begin{pmatrix} r_{11} & r_{12} & 0 & 0 & 0 & r_{16} \\ r_{21} & r_{22} & 0 & 0 & 0 & r_{26} \\ 0 & 0 & r_{33} & r_{34} & 0 & 0 \\ 0 & 0 & r_{43} & r_{44} & 0 & 0 \\ r_{51} & r_{52} & 0 & 0 & 1 & r_{56} \\ 0 & 0 & 0 & 0 & 0 & 1 \end{pmatrix} \cdot \begin{pmatrix} x \\ x' \\ y \\ y' \\ z \\ \Delta p/p_0 \end{pmatrix}_{s_0} . \tag{2.4}$$

The matrix is not fully populated because, for simplicity, it is assumed that coupling between horizonal and vertical plane and between longitudinal and vertical motion can be neglected.

For the application in a storage ring, it is intended to store electrons on a predetermined orbit for many hours. Hence, magnetic fields are used to focus the electron beam to achieve a closed orbit. In good approximation, the behavior of the electrons in a beam can be treated as an independent motion of single particles in a first step. However, collective effects need to be studied for real storage rings, when a large number of electrons is stored [33,34]. From the balance of Lorentz and centripetal force, the local transverse bending radius ρ_m can be deduced as

$$\frac{1}{\rho_\mathrm{m}} = \frac{q}{p_0}\mathcal{B}_y(x) = \frac{q}{p_0}\left(\mathcal{B}_y(0) + \frac{\mathrm{d}\mathcal{B}_y(x)}{\mathrm{d}x}\cdot x + \frac{1}{2}\frac{\mathrm{d}^2\mathcal{B}_y(x)}{\mathrm{d}x^2}\cdot x^2 + \ \ldots\right) \tag{2.5}$$

which can be rewritten as

$$\frac{q}{p}\mathcal{B}_y(x) = \underbrace{\frac{1}{\rho}}_{\text{dipole term}} + \underbrace{kx}_{\text{quadrupole term}} + \underbrace{\frac{1}{2}\cdot m x^2}_{\text{sextupole term}} + \ \ldots\ . \tag{2.6}$$

The expansion splits the description of the magnetic field into multipole components which are used to define the properties of the storage ring magnets. An analogous expansion holds for $\mathcal{B}_x(y)$. Taking multipole contributions up to linear order into consideration leads to the equations of motion

$$x''(s) + \left(\frac{1}{\rho^2(s)} - k(s)\right)x(s) = \frac{1}{\rho(s)}\frac{\Delta p}{p_0} \tag{2.7}$$

$$\text{and} \qquad y''(s) + k(s)y(s) = 0 \tag{2.8}$$

with the nominal electron momentum p_0 and the restriction that all dipole magnets cause a horizontal deflection. Equation (2.7) and Eq. (2.8) form so-called Hill-type linear ordinary differential equations [35,36]. The position $x(s)$ and its second derivative $x''(s) = \mathrm{d}x/\mathrm{d}s$ depend on the dipole bending radius $\rho(s)$, the relative momentum deviation $\Delta p/p_0$, and the quadrupole strength $k(s)$, whereas the vertical position only depends on $k(s)$.

Solutions of Eqs. (2.7) and (2.8) are

$$x(s) = \sqrt{\epsilon_x\beta_x(s)}\cdot\cos\left(\mu_x(s)\right) + D(s)\cdot\frac{\Delta p}{p_0} \tag{2.9}$$

$$\text{and} \qquad y(s) = \sqrt{\epsilon_y\beta_y(s)}\cdot\cos(\mu_y(s))\ . \tag{2.10}$$

with the betatron phase $\mu_{x,y}(s)$, the envelope $E_{x,y}(s) = \sqrt{\epsilon_{x,y}\beta_{x,y}(s)}$ defined by the so-called Courant-Snyder invariant $\epsilon_{x,y}$ [37] and the position-dependent betatron function $\beta_{x,y}(s)$. The oscillation can be regarded as quasi-harmonic with a non-constant oscillation frequency. The momentum-dependent horizontal displacement in the bending magnets is accounted for by the dispersion function

$$D(s) = \frac{x}{\Delta p/p_0} \tag{2.11}$$

which is also the particular solution of Eqs. 2.7. In general, Hill-type differential equations are solved by two complex conjugate equations which means that the conjugates of Eqs. 2.9 and 2.10 are solutions to be considered, too.

The cosine terms in Eqs. 2.9 and 2.10 represent an oscillatory motion about the reference orbit which is referred to as betatron oscillation [38,30] with the frequencies f_x and f_y. The beta functions $\beta_{x,y}(s)$ can be used to express the betatron phase $\mu_{x,y}(s)$ as

$$\mu_{x,y}(s) = \int_0^s \frac{1}{\beta_{x,y}(\hat{s})} \mathrm{d}\hat{s}. \tag{2.12}$$

Integration along s' and dividing by 2π yields the number of oscillations per revolution as

$$Q_{x,y} = \frac{1}{2\pi}\mu_{x,y}(s) \tag{2.13}$$

which defines the horizontal and vertical betratron tune Q_x and Q_y. The frequencies f_x and f_y with revolution frequency f_{rev} read

$$f_x = Q_x \cdot f_{\mathrm{rev}} \qquad \text{and} \qquad f_y = Q_y \cdot f_{\mathrm{rev}}. \tag{2.14}$$

To prevent the occurence of so-called betatron resonances which counteract a stable operation, the configurations

$$m \cdot Q_x + n \cdot Q_y = p \qquad \text{with } m, n, p \in \mathbb{N}^+ \tag{2.15}$$

have to be avoided. The destabilizing effect decreases with the order $|m| + |n|$ of the resonance and in practice only resonances up to the 5th order are considered [29].

Since the focusing of quadrupole magnets is energy-dependent, the energy spread of the electrons leads to a variation of the horizontal and vertical focusing and hence the respective tune of the electrons. The chromaticity

$$\eta_{x,y} = \frac{\Delta Q_{x,y}}{\Delta p/p} \tag{2.16}$$

describes the shift $\Delta Q_{x,y}$ of the betatron tune normalized to the relative momentum deviation. Typically, the so-called natural chromaticity is negative. Even small momentum deviations cause tune shifts towards resonances and lead to an unstable beam. Furthermore, with negative chromaticity the so-called head-tail instability is excited, a collective effect giving rise to an intra-bunch oscillation [33] which limits the maximum bunch charge. For a stable operation, especially in operation modes with high bunch current, it is advisable to increase the chromaticity to a value slightly above zero which is achieved by installing sextupole magnets at locations with dispersion. The chromaticity then reads

$$\eta_{x,y} = \frac{1}{4\pi} \oint \left[m(s) D_{x,y}(s) - k(s) \right] \beta_{x,y}(s) \, \mathrm{d}s \tag{2.17}$$

with the sextupole strength $m(s)$ and a cyclic integration along one turn.

The geometrical placement of different magnets, i.e., the lattice, needs to be studied carefully when designing a new storage ring. For a given lattice, it is often possible to apply different settings to the strength of groups of magnets to realize special operation modes. This can, for example, be a different beam energy, a special short-bunch mode or a different tune. These settings are distinguished as different optics.

2.1.2 Longitudinal beam dynamics

One special operation mode implemented at several electron storage rings is the so-called low-alpha optics [39, 40, 41, 42]. The coupling between the transverse and longitudinal plane is caused by the dispersion $D(s)$ which leads to changes of the orbit length ΔL depending on the electron momentum. This effect is described by the momentum compaction factor α_c [43] with

$$\frac{\Delta T}{T_0} = \left(\alpha_c - \frac{1}{\gamma^2} \right) \frac{\Delta p}{p_0} \qquad \text{and} \qquad \alpha_\mathrm{c} = \frac{\Delta L / L_0}{\Delta p / p_0}. \tag{2.18}$$

Here, $\Delta T/T_0$ and $\Delta L/L_0$ are the relative change of the revolution time the ring circumference, respectively, with the design length L_0. The Lorentz factor γ in relation to α_c

distinguishes between two effects: For relativistic values of γ, a positive deviation in momentum Δp will no longer increase the electron velocity significantly, but will increase the accelerator circumference due to the larger bending radii. For low values of γ, a momentum change Δp increases the electron velocity significantly which leads to a decrease of the revolution time. The transition between these two scenarios is given by the transition energy E_t and the respective Lorentz factor γ_t as

$$E_\mathrm{t} = \gamma_\mathrm{t} m_0 c^2 = \frac{1}{\sqrt{\alpha_\mathrm{c}}} m_0 c^2, \tag{2.19}$$

if α_c is positive. However, machines (temporarily) operated with negative α_c exist [44, 45]. The momentum compaction factor is derived from the accelerator optics as

$$\alpha_\mathrm{c} = \frac{1}{L_0} \oint \frac{D(s)}{\rho(s)} \,\mathrm{d}s. \tag{2.20}$$

As will be outlined in this section, reducing the momentum compaction factor leads to shorter electron bunches which is beneficial for the generation of short synchrotron radiation pulses.

The longitudinal motion of electrons in a storage ring is determined by three major effects:

- gain of energy due to acceleration in the electric field of a radiofrequency (RF) resonator (also referred to as RF cavity)
- loss of energy due to emission of synchrotron radiation (see Sect. 2.2) by the electrons
- momentum dependence of the orbit length

On average, the energy loss per electron per turn [29] is

$$W_0 = \frac{e^2}{3\epsilon_0 \rho} \cdot \left(\frac{E}{E_\mathrm{r}} \right)^4 \tag{2.21}$$

with the beam energy E, the bending radius ρ and the vacuum permittivity ϵ_0. The energy loss is recovered if

$$W_0 = e \cdot V_0 \cdot \sin(\Psi_\mathrm{s}) \,. \tag{2.22}$$

Here, V_0 is the peak cavity voltage and Ψ_s denotes the synchronous phase. Electrons which lost more than the average energy W_0 are still stored because the acceleration voltage is higher than needed to compensate the mere losses. The overcompensation

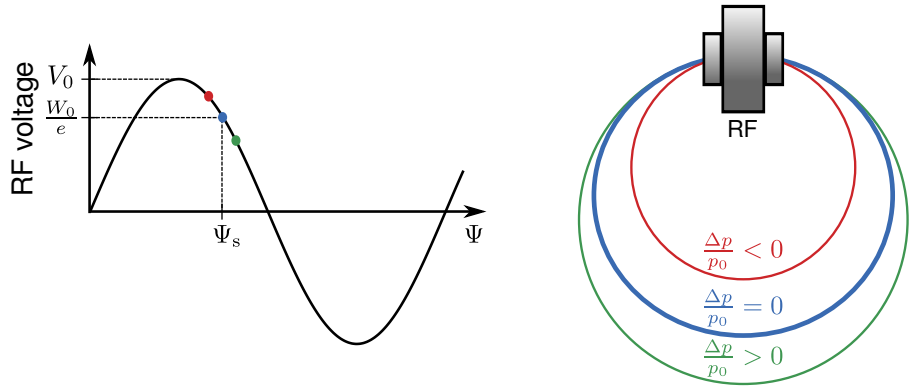

Figure 2.2: The energy gain of an electron depends on its arrival time at the RF cavity. The correct phase to compensate for the average loss per turn W_0, is Ψ_s. A relativistic particle with a positive momentum deviation will move on a longer orbit. This will cause the electron to arrive later at the cavity and it will be accelerated by a lower voltage. The opposite effect occurs for a particle with negative momentum deviation. Hence, using the trailing edge of the RF potential for acceleration causes a longitudinal focusing effect, the so-called phase focusing.

leads to an oscillation of the arrival time at the cavity which is referred to as synchrotron oscillation [39].

Figure 2.2 shows the effect of phase focusing leading to the synchrotron oscillation. Electrons with a momentum smaller than the nominal momentum are deflected to a shorter trajectory in the bending magnets, leading to an earlier arrival at the cavity (red trajectory) after the subsequent revolution. This leads to a stronger acceleration (see Fig. 2.2, left) and hence, a mitigation of the energy loss. The effect opposing the energy loss causes the synchrotron oscillation. The synchrotron frequency f_s is given by [39,43]

$$f_s = \frac{1}{T_0}\sqrt{-\frac{2\pi e V_0 h \cos\Psi_s}{\beta^2 E}\left(\alpha_c - \frac{1}{\gamma^2}\right)}\,. \tag{2.23}$$

Here, $h = f_{RF}/f_{rev}$ is the so-called harmonic number which is the ratio of RF frequency f_{RF} and revolution frequency f_{rev}. It determines the maximum number of bunches that can be stored. The corresponding synchrotron tune is defined as $Q_s = f_s/f_{rev}$. It is typically of the order of 10^{-2} because the oscillation in the longitudinal plane traverses much less than one oscillation period per turn. The longitudinal size of an electron bunch, i.e., the bunch length, is given by

$$\sigma_z = \left|\frac{c\alpha_c \sigma_{\Delta p/p_0}}{2\pi f_s}\right|, \tag{2.24}$$

where $\sigma_{\Delta p/p_0}$ is the relative momentum spread.

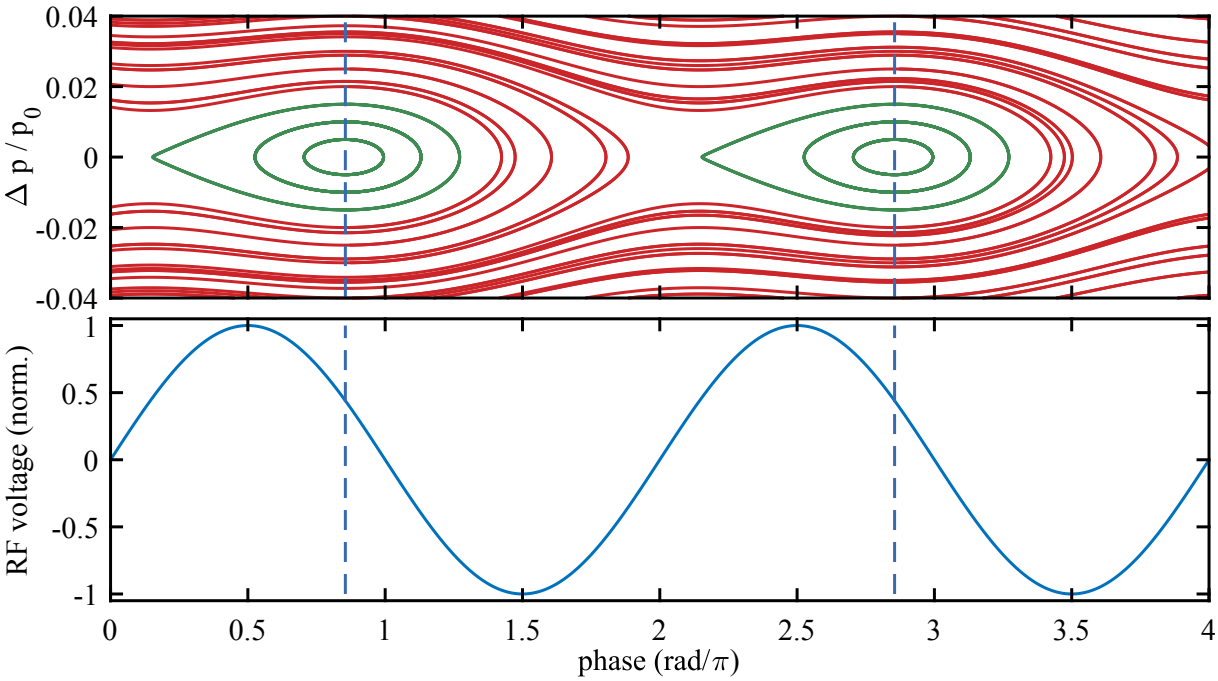

Figure 2.3: Longitudinal phase space of an electron storage ring (top). Storing electrons is possible at distinct areas in phase space. Stable trajectories are plotted in green. Bottom: RF voltage versus phase. The blue dashed lines indicate the synchronous phase which is the center of a stable area in phase space.

The coordinates of the longitudinal phase space are the RF phase Ψ and the relative momentum deviation $\Delta p/p$ as depicted in Fig. 2.3. Here, the range of stable trajectories is shown in green, whereas unstable trajectories, with phase or momentum deviations being too large, are plotted in red. In addition, the RF voltage is plotted below. The blue dashed lines indicate the synchronous phase Ψ_s. For small deviations from the phase Ψ_s and the nominal momentum $\Delta p/p_0 = 0$, the stable trajectories in phase space form ellipses. For larger amplitudes these trajectories become asymmetric in the phase coordinate.

The width along the $\Delta p/p_0$ axis of the stable region expresses the momentum acceptance of the accelerator. As $Q_s \ll 1$ holds for the synchrotron tune, the turn-by-turn advance of an electron in the longitudinal phase space is only a small step along a green curve. The longitudinal electron motion is an oscillation between off-energy and off-phase states over a number of turns equal to $1/Q_s$. Measurements of the longitudinal motion of electrons, which were energy-modulated by an optical laser, are presented in Chap. 6.

2.2 Radiation from charged particles

The characteristics of the electromagnetic field caused by an electron bunch which is seen by an observer strongly depends on the distance between bunch and observer. An observer being close to the electron bunch (near-field observer), detects a dominating Coulomb field. Far away from the bunch, synchrotron radiation is observable. This section will give an overview of the two regimes and radiation effects employed at synchrotron radiation sources.

2.2.1 Near-field regime

The electric field at a distance r of a particle with charge q being at rest is given by

$$\vec{\mathcal{E}}_C = \frac{1}{4\pi\epsilon_0}\frac{q}{r^2}\frac{\vec{r}}{r}. \tag{2.25}$$

The magnetic field is zero and hence, the Poynting vector [46]

$$\vec{S} = \frac{1}{\mu_0}\vec{\mathcal{E}} \times \vec{B} \tag{2.26}$$

is zero, too. In consequence, no electromagnetic radiation is emitted in the case of the charge being at rest. However, for an observer in a stationary laboratory frame, a moving charge causes a current, which leads to a non-zero magnetic field and a non-zero Poynting vector. It is then necessary to replace the classical potentials by Liénard-Wiechert potentials

$$\Phi(r,t) = \left.\frac{1}{4\pi\epsilon_0}\cdot\frac{q}{r}\cdot\frac{1}{1-\vec{n}\cdot\vec{\beta}}\right|_{t_\mathrm{r}} \tag{2.27}$$

$$\text{and} \qquad \vec{A}(r,t) = \left.\frac{\mu_0}{4\pi}\cdot\frac{q}{r}\cdot\frac{\vec{\beta}}{1-\vec{n}\cdot\vec{\beta}}\right|_{t_\mathrm{r}} \quad . \tag{2.28}$$

Here, $\vec{\beta} = \vec{v}/c_0$ is the relative velocity and $\vec{n}$ is the unit vector pointing from the charge towards the observer. The quantities are evaluated at the retarded time $t_\mathrm{r} = t - R(t_\mathrm{r})/c_0$ where $R(t_\mathrm{r})$ is the distance between the observer and the charged particle.

The electric field $\vec{\mathcal{E}}(r,t)$ and the magnetic field $\vec{\mathcal{B}}(r,t)$ can be calculated from these potentials, which leads to

$$\vec{\mathcal{E}}(r,t) = \frac{-e}{4\pi\epsilon_0}\left[\underbrace{\frac{(1-\beta^2)(\vec{n}-\vec{\beta})}{r^2(1-\vec{n}\cdot\vec{\beta})^3}}_{\text{Coulomb regime}} + \underbrace{\frac{[n\times((\vec{n}-\vec{\beta})\times\dot{\vec{\beta}})]}{cr(1-\vec{n}\cdot\vec{\beta})^3}}_{\text{radiation regime}}\right]\Bigg|_{t_\mathrm{r}} \tag{2.29}$$

$$\vec{\mathcal{B}}(r,t) = \frac{[\vec{n}\times\vec{\mathcal{E}}]}{c}\Bigg|_{t_\mathrm{r}}. \tag{2.30}$$

Here, the temporal change of the velocity is expressed as $\dot{\vec{\beta}} = \frac{\mathrm{d}\vec{\beta}}{\mathrm{d}t}$. Equation 2.29 contains a sum of two different contributions to the electric field. The Coulomb regime is described by the first term. The second term decreases only linearly with distance r and is proportional to the acceleration $\dot{\vec{\beta}}$. It is referred to as the far-field regime and describes the radiation phenomenon known as synchrotron radiation. In the static case with $\vec{\beta} = \dot{\vec{\beta}} = 0$, Eq. 2.29 simplifies to the Coulomb field (cf. Eq. 2.25).

2.2.2 Far-field regime

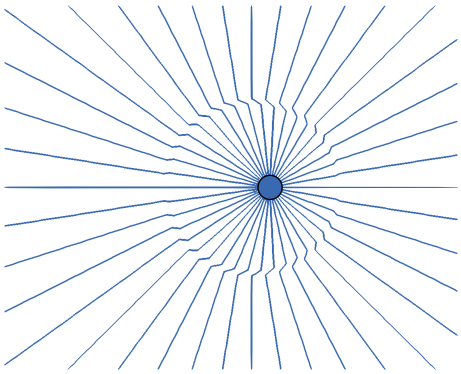

Figure 2.4: The electric field lines (blue) from a point charge (black circle) which was accelerated after being at rest are distorted because the change of the electric field expands with the speed of light. These distortions are time-dependent transverse components of the electric field which form an electromagnetic wave. This illustration is based on a simulation performed with the code Radiation2D [47,48].

Far away from the charge, the Coulomb term of Eq. 2.29 can be neglected and the expression for the electric field reduces to [46]

$$\vec{\mathcal{E}} = -\frac{e}{4\pi\epsilon_0}\frac{1}{cr}\left[\vec{n}\times(\vec{n}\times\dot{\vec{\beta}})\right]_{t_\mathrm{r}}. \tag{2.31}$$

With the Poynting vector

$$\vec{S} = \epsilon_0 c|\vec{\mathcal{E}}|^2\vec{n} \tag{2.32}$$

the radiation power emitted from an accelerated charge can be calculated as

$$P_\mathrm{S} = \frac{e^2 c}{6\pi\epsilon_0}\frac{1}{E_\mathrm{r}^2}\frac{E^4}{\rho^2}. \tag{2.33}$$

The reciprocal dependence on the rest energy E_r and the proportionality to the fourth power of the energy E lead to strong emission in the case of relativistic particles. A simplified model of the radiation emission is illustrated in Fig. 2.4. Here, a point charge formerly being at rest is accelerated to a relativistic speed. The change of the electric field which originates from the position change propagates with the speed of light. This causes distortions of the electric field lines which are time-dependent transverse components of the electric field and hence can be regarded as an electromagnetic wave traveling away from the charge.

2.2.3 Bending magnet radiation

As can be seen in Eq. 2.33, a relativistic electron beam deflected by a bending magnet in a storage ring emits synchrotron radiation. The emission spectrum is given by [29]

$$\frac{\mathrm{d}P}{\mathrm{d}\omega}(\omega) = \frac{2}{3}\frac{I}{e}\frac{r_e m_0 c^3\beta^4\gamma^4}{\omega_c\rho^2}\cdot S\left(\frac{\omega}{\omega_c}\right) \tag{2.34}$$

with the classical electron radius $r_c = e/(4\pi\epsilon_0 m_0 c^2)$, the beam current $I = q/T_0$, the critical frequency

$$\omega_c = \frac{3}{2}\frac{c\gamma^3}{\rho} \qquad \text{and} \qquad S(x) = \frac{9\sqrt{3}}{8\pi}x\int_x^\infty K_{5/3}(x)\mathrm{d}x, \tag{2.35}$$

where K_α is the modified Bessel function of the second kind.

Bending magnet radiation is predominantly polarized horizontally because the electron motion is confined to the horizontal plane. However, an observer with a vertical offset from the bending plane detects elliptical polarization, too.

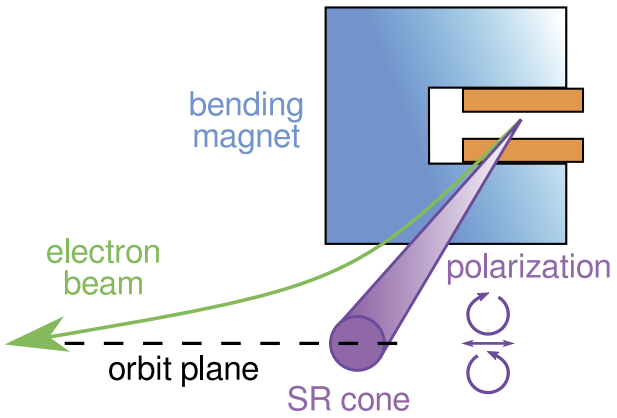

Figure 2.5: The polarization of synchrotron radiation (SR) from a bending magnet is linearly polarized in the plane of motion. An elliptical radiation polarization of opposite handedness can be observed above and below the orbit plane respectively.

The polarization of synchrotron radiation emitted from a bending magnet is depicted in Fig. 2.5 for different vertical observation angles. Here, due to the direction of the bending curvature, above the electron beam an additional right-handed polarization component is observed and below the electron beam, an additional left-handed polarization component is observed, respectively. A precise calculation of the angular integration can be found in [30]. The integrated polarization fractions after the projection to horizontal polarization and vertical plane are

$$P_\mathrm{h} = \frac{7}{8} P_\mathrm{tot} \qquad \text{and} \qquad P_\mathrm{v} = \frac{1}{8} P_\mathrm{tot} \,. \tag{2.36}$$

In Chap. 4, a spectrometer for synchrotron radiation using polarizing beam splitters is presented. The polarization fraction $P_\mathrm{h}/(P_\mathrm{h} + P_\mathrm{v})$ is an important figure for the design of the spectrometer.

2.2.4 Undulator radiation

An undulator (cf. Fig. 2.6) consists of a periodic sequence of alternating bending magnets. The on-axis field is described by the undulator period λ_u and the field amplitude $\mathcal{B}_0$ as

$$\mathcal{B}_y(s) = \mathcal{B}_0 \cos(k_\mathrm{u} s) \qquad \text{with} \qquad k_\mathrm{u} = \frac{2\pi}{\lambda_\mathrm{u}}. \tag{2.37}$$

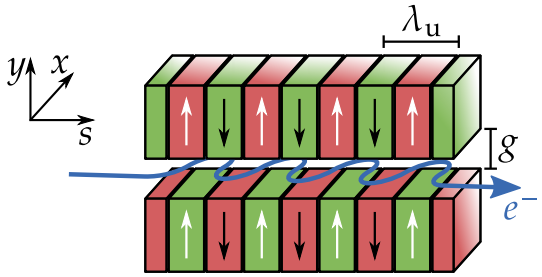

Figure 2.6: Sketch of an undulator and the electron orbit (blue). The set of alternating magnets with fixed period length λ_u and pole gap g leads to an oscillatory horizontal electron motion (see text for details).

The solution of the equations of motion of an electron moving along the axis are [29]

$$x(t) = -\frac{K}{k_u \gamma} \cos(\omega_u t) \tag{2.38}$$

$$\text{and} \qquad s(t) = \beta^* c t + \frac{K^2}{8 k_u \gamma^2} \sin(2\omega_u t) \tag{2.39}$$

$$\text{with} \qquad K = \frac{\lambda_u e B_0}{2\pi m_0 c} \quad \text{and} \quad \beta^* = 1 - \frac{1}{2\gamma^2}\left(1 + \frac{K^2}{2}\right), \tag{2.40}$$

where the angular frequency $\omega_u = k_u \beta^* c$ modulates the longitudinal speed with $2\omega_u$.

Since the electron motion in an undulator has a non-zero horizontal velocity component v_x, an acceleration or deceleration caused by the external field is possible and an energy exchange with the external electromagnetic wave travelling along the undulator occurs. The on-axis electron in a horizontal electric field $\vec{\mathcal{E}}_L(t) = (E_L(t), 0, 0)$ experiences an energy change of

$$\Delta W = -e \int \vec{\mathcal{E}}_L(t)\, \mathrm{d}\vec{s} = -e \int v_x E_L \, \mathrm{d}t \qquad \text{with} \tag{2.41}$$

$$v_x = \dot{x} = \frac{\mathrm{d}x(t)}{\mathrm{d}t} = \frac{\beta^* c K}{\gamma} \sin(\omega_u t). \tag{2.42}$$

Considering an electric field of an external laser

$$E_L(t) = E_{L,0} \cos\left(k_L s - \omega_L t + \phi_L\right) \tag{2.43}$$

the energy exchange is

$$\Delta W = -\frac{ceE_{L,0K}}{2\gamma} \int \left[\sin(\Psi_+) - \sin(\Psi_-)\right] \mathrm{d}t \qquad \text{with} \tag{2.44}$$

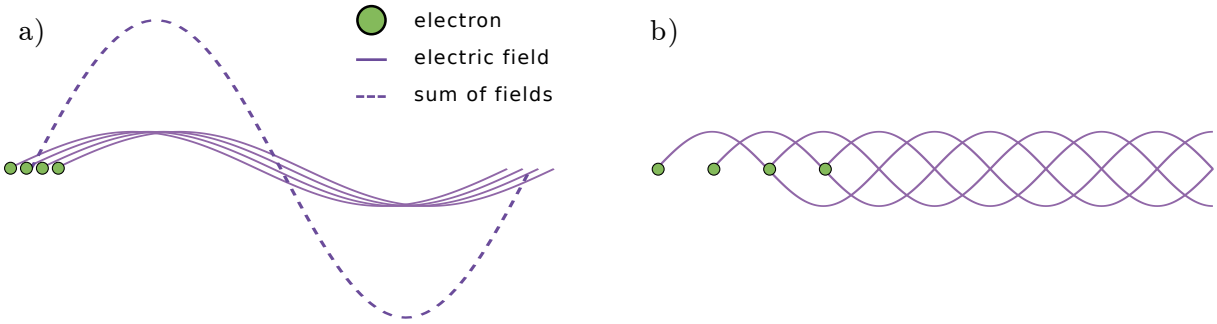

Figure 2.7: a) If the bunch length and the emitted wavelength are on the same order, the electric fields interfere constructively and the emission is coherent. b) If the wavelength is shorter than the bunch length, there is no constant phase relation between the wave trains and the emission is incoherent.

$$\Psi_{\pm} = (k_{\mathrm{L}} \pm k_{\mathrm{u}})s - \omega_{\mathrm{L}} t + \phi_{\mathrm{L}} \tag{2.45}$$

and the field amplitude $E_{\mathrm{L},0}$, the wavenumber $k_{\mathrm{L}} = 2\pi/\lambda_{\mathrm{L}}$ and start phase ϕ_{L}. A net energy change ΔW requires at least one of the two phases Ψ_+ and Ψ_- to be constant. The condition $\frac{\mathrm{d}\Psi_+}{\mathrm{d}t} = 0$ is fulfilled by the resonance condition

$$\lambda_{\mathrm{L}} = \frac{\lambda_{\mathrm{u}}}{2\gamma^2}\left(1 + \frac{K^2}{2}\right). \tag{2.46}$$

Here, the oscillating motion of the electron reduces the effective longitudinal electron velocity such that the electron lags behind one field period per undulator period which causes the term $E_{\mathrm{L}} v_x$ to always have the same sign.

Equation 2.46 is not only the condition for an energy transfer from an external electric field to an electron traveling through an undulator, but it is also the on-axis emission wavelength of an undulator set to an undulator strength K.

2.2.5 Temporal coherence

The emission of radiation by a single charged particle was described in the previous section. The emission characteristics changes if bunches of charged particles containing many particles are considered. The intensity of the radiation emission from a bunch of N_e particles scales with the number of particles, as long as the emitted wavelength is much shorter than the bunch length, which resembles the case of incoherent emission. If the emission wavelength is longer than the bunch length, the emission from different electrons occurs in a phase-stable way, which leads to an intensity increase.

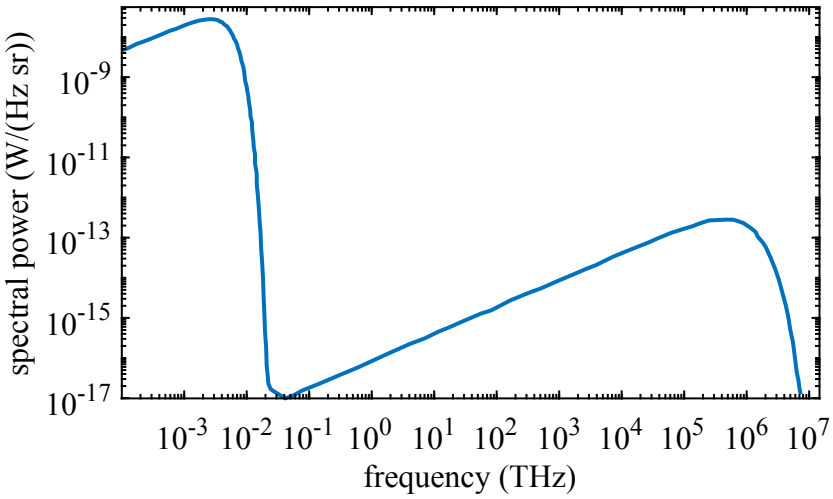

Figure 2.8: Calculated emission spectrum from a bending magnet at DELTA at a beam current of $10\,\mathrm{mA}$.

Figure 2.7 depicts the emission from short electron bunches. Phase differences much smaller than 2π (see Fig. 2.7a) lead to an in-phase summation of the electric field and (cf. Eq. 2.32) a quadratic increase of the intensity. The incoherent emission at wavelengths being short compared to the bunch length is shown in Fig. 2.7b).

Mathematically, this can be described by considering the radiation field $\mathcal{E}_i(\omega)$ from an electron at the longitudinal position z_i

$$\mathcal{E}_i(\omega) \propto e^{j(\omega t + \frac{2\pi}{\lambda} z_i)} \tag{2.47}$$

The total radiation power from a bunch with N_e electrons is then

$$P(\omega) \propto \sum_{k,l}^{N_e} \mathcal{E}_k \mathcal{E}_l^\star \propto \sum_{k,l}^{N_e} e^{j\frac{2\pi}{\lambda}(z_k - z_l)} = N_e + \sum_{k \neq l}^{N_e} e^{j\frac{2\pi}{\lambda}(z_k - z_l)}. \tag{2.48}$$

Here, the remaining sum can be expressed by the form factor $g(\omega) = \mathcal{F}(\rho(z))$ which is the Fourier transform of the longitudinal electron density $\rho(z)$ leading to

$$P(\omega) = P_e(\omega) N_e \left[1 + (N_e - 1) g^2(\omega)\right] \tag{2.49}$$

with P_e being the radiation power emitted from a single electron. Figure 2.8 shows a calculated spectrum of the synchrotron radiation emitted by a bending magnet at the DELTA storage ring. Here, coherent emission causes a strong contribution around $5\,\mathrm{GHz}$.

2.3 Terahertz radiation

In 1800, astronomer William Herschel dispersed sunlight with an optical prism and measured the light-induced temperature change at different positions of the spectrum [49]. The observation of a temperature increase from blue light to red light and even beyond led to the discovery of both, heat radiation and the infrared region of the electromagnetic spectrum [50]. Energy transport through electromagnetic waves was later predicted by James Clerk Maxwell in 1867 [51] and was experimentally verified by Heinrich Hertz in 1887 [52]. The experiments of Hertz included the discovery of radio wave concepts already known from optics like polarization, diffraction, refraction and also standing waves. In the 20th century, the spectral range between these two discovered regimes, the far-infrared region and the micro-wave region, was still referred to as the THz gap. This term expresses the lack of experimental access to frequencies in the THz range because for a long time neither suitable detectors nor efficient sources were available [53].

The technical challenges in the THz range are inherently connected to the photon energy $E_{\mathrm{ph}} = hc/\lambda$ with Planck's constant h, speed of light c and wavelength $\lambda = 0.3\,\mathrm{mm}$ which is $4\,\mathrm{meV}$ at a frequency $\nu = 1\,\mathrm{THz}$. This energy lies far below a typical thermal excitation $k_{\mathrm{B}}T \approx 26\,\mathrm{meV}$ with room temperature $T = 300\,\mathrm{K}$ and the Boltzmann constant k_{B}. This makes handling THz radiation sensitive to thermal influence of the detector or the radiation source itself. The macroscopic wavelength makes the beam transport sensitive to diffraction losses. Metal conductors suffer from increased electrical resistance in the THz range due to the skin effect: The frequency is high enough such that the effective thickness of the conductor is decreased [46] which reduces the conductivity. Further challenges regarding the radiation emission from THz sources, radiation detection and the description of transverse beam properties are given in this section. A comprehensive overview of the topic can be found in [53].

2.3.1 THz sources

Historically, the first THz sources were based on thermal emission of heated material. A continuous-wave (CW) source commonly used for laboratory applications is the so-called Globar[1], which emits thermal radiation following Planck's law [54]. Globars are usually made of silicon carbide which is electrically heated to about $1200\,\mathrm{K}$ to cover a spectral range from about $20\,\mathrm{THz}$ to $75\,\mathrm{THz}$ [53].

[1] The word is a registered trademark which resembles the words "glow" and "bar" as a portmanteau word.

Lower frequencies, namely the region from $0.3\,\mathrm{THz}$ to $10\,\mathrm{THz}$ [55], are reached by plasma sources like gas-discharge lamps. One example for this kind of THz emitter are water-cooled mercury-based arc lamps. Both, Globars and gas-discharge lamps are still used today in spectroscopic applications. Many spectrometers comprise these incoherent emitters as internal sources which are used for measurements as well as reference purposes.

Today's scientific applications also demand pulsed THz radiation to study time-dependent phenomena. This especially holds for pump-probe experiments where a time-dependent process in a sample is excited by a radiation pulse which is followed by another pulse to analyze the state of the sample after an adjustable delay. An overview of state-of-the-art THz generation schemes used for pump-probe experiments is given in [56]. Among the most popular methods are optical rectification (OR) and the use of photo-conductive antennas (PCA). The OR scheme employs crystals consisting of a material with a non-linear electric susceptibility $\chi^{(2)}$. The non-linearity causes sum- and difference-frequency generation within the laser pulse which leads to a broadband emission ranging from the quasi-DC region to many THz. Dispersion and phase-matching conditions in the crystal limit the emission bandwidth typically to the inverse of the incoming pulse duration such that a $100\,\mathrm{fs}$ long pulse will generate broadband radiation up to $10\,\mathrm{THz}$. The intrinsic synchronization between laser pulse and THz pulse is beneficial for spectroscopic application where a portion of the initial laser pulse is also used by the THz diagnostics equipment which is often the case for time domain spectrometers.

A PCA can be regarded as a laser-driven and simultaneously laser-gated THz oscillator. The antenna consists of two metal contacts which are fabricated on a semiconductor layer by lithography. These two antenna parts are biased with a DC voltage, but since the semiconductor is undoped no current flows through the micrometer-sized gap between them. Focusing a femtosecond laser pulse of sufficient photon energy onto the gap between the metal contacts bridges the semiconductor's band gap and the laser pulse excites electrons into the conduction band. The resistivity of the gap drastically decreases and consequently, a rapid current flow between the metallized antenna regions occurs which either leads to pulsed broadband or narrowband CW radiation emission. The bandwidth depends on the laser pulse shape and the antenna response defined by the antenna geometry. The laser pulse shape mainly determines the maximum emission frequency, but apart from that the emission spectrum is not adjustable.

It was shown before that synchrotron radiation features a continuous spectrum ranging over a broad frequency range which even covers the THz range at the low-frequency end. As discussed in Sec. 2.2, coherent emission is the key to increase the emission

intensity. Besides the generation of short bunches directly, sub-picosecond structures in the longitudinal charge density can arise naturally from the so-called microbunching instability (MBI) [57]. Here, a random density fluctuation radiates coherently and the radiation acts back on the electron which leads to an amplification of the density structure. Since a certain charge density threshold has to be overcome before the emission starts, the MBI is typically used for THz generation in the low-alpha mode, where the bunches are short. The broadband radiation is emitted in so-called THz bursts at a repetition rate equal to the revolution rate. While the high repetition rate is beneficial, the shot-to-shot stability in terms of spectrum and intensity is not as good as given by laser-powered THz emitters. A comparison of laser-based and accelerator-based sources shows that a THz source with high repetition rate, tunable spectrum and tunable pulse length would lie inbetween these solutions. A source fulfilling these requirements is developed in this thesis and is presented in Chap. 3. Improvements to this source are explained in detail in Chap. 5.

2.3.2 THz detectors

Detectors for THz radiation in general shall transduce the incident electromagnetic wave properties into a different physical quantity which can be recorded for further analysis. Information about amplitude and phase is required to fully describe the properties of the electromagnetic wave. However, not every type of detector can resolve both pieces of information. Direct or incoherent detectors only resolve the amplitude, whereas coherent detectors resolve amplitude and phase. Generally, the low photon energy of THz radiation competes with thermal excitations in the detector material which makes cooling necessary in many cases. The output is not necessarily an electrical signal. Golay cells, for example, are operated as pneumatic THz detectors which convert the energy of the THz pulse into a pressure change inside a small gas volume. The deformation of a membrane is then measured with an optical readout system [58, 59].

Two coherent detection schemes of THz pulses are electro-optic sampling (EOS) and electro-optic spectral decoding (EOSD) [60,61]. Here, the field of the THz pulse changes the polarization of a laser pulse in an optical crystal with pronounced nonlinear susceptibility due to the linear electro-optic effect, the Pockels effect. Measuring the influence on the laser pulse polarization reveals the properties of the THz pulse. Since the polarization change is proportional to the electric field, this method offers information about phase and amplitude. A setup implementing EOS and EOSD techniques is under commissioning at DELTA but was not yet in operation for use within this thesis [62, 63]. More information on these techniques can be found in [64, 65].

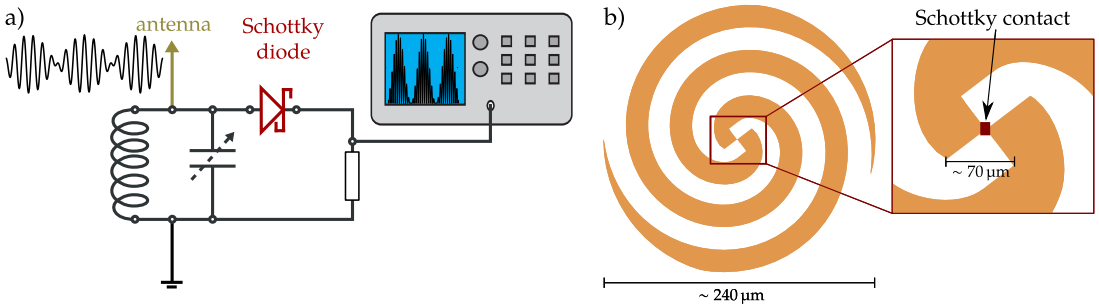

Figure 2.9: a) A Schottky-barrier detector receives an RF signal and rectifies the field. The rectification introduces a DC component at the detector output which serves the incoherent detection signal. b) The antenna of many broadband Schottky-barrier detectors is implemented as a log-spiral which has the Schottky-diode in its center. Often, the barrier is coupled to a bow-tie shaped inner antenna region (see inset)

Long before the challenge to detect THz radiation was considered, radio waves were received through RF rectifiers based on Schottky-type hot-carrier diodes. These were made of point-contacted lead crystals [66]. The non-linear voltage-to-current relation in these devices introduces a DC component which is related to the power of the electromagnetic wave (cf. Fig. 2.9a). The rectification process needs to be intrinsically fast which is also the reason why semiconductor-based p-n diodes are not suitable for this purpose. The so-called reverse recovery time of a diode characterizes the switching time from the conducting to the non-conducting state. P-n junctions typically reach a shortest value of $t_{\mathrm{rr}} \approx 10\,\mathrm{ns}$ which means that the charge-carriers are not able to follow the electric field fast enough at frequencies much higher than about $100\,\mathrm{MHz}$ [67]. Schottky diodes do not suffer from a recovery time because the junction is not depleted of charge carriers. The bandwidth of Schottky-based rectifiers is limited to frequencies around 4 THz [68] mainly because of capacitive loading. In consequence, Schottky detectors for THz receivers use small-area junctions to reduce this effect.

The antenna has a strong influence on the spectral sensitivity. Narrowband detectors make use of coupling to a low-bandwidth antenna [69]. To reduce the sensitivity to the polarization direction, the most common receiver type uses the so-called log-spiral antenna [70] which is sometimes combined with a bow-tie antenna in the center. Figure 2.9b shows a sketch of a log-spiral antenna matched to a frequency of $1\,\mathrm{THz}$. Narrowband detectors often use exchangeable horn-shaped antennas to define the spectral sensitivity. Many of the measurements presented in this thesis were carried out with the Schottky-barrier detector shown in Fig. 2.10. Details about the device can be found in A.1.

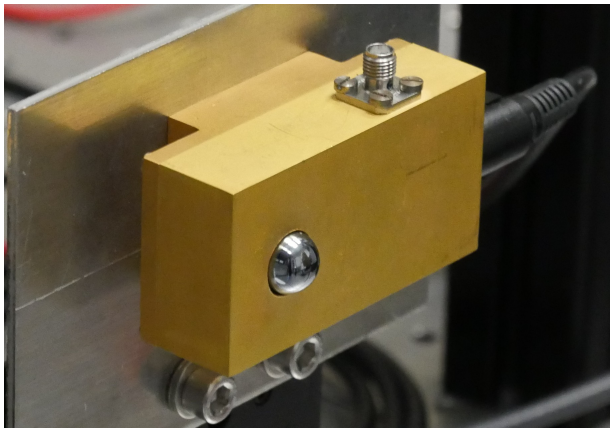

Figure 2.10: Commercially available Schottky detector used for the observation of THz radiation. The detector case houses the bias circuit for the detector and an amplifier with a bandwidth of $4\,\mathrm{GHz}$. The THz radiation is focused by a ball lens made of silicon. The output signal is coupled by a $2.92\,\mathrm{mm}$/K-type connector which offers better RF properties than a standard SMA connector [71] but is intermateable with it.

Detectors with a much weaker frequency-dependent response are semiconductor-based bolometers. Bolometers are thermal detectors which react to a temperature change with a changing electrical resistance. At DELTA, a Si bolometer is used which is cooled with liquid helium (temperature of $4.2\,\mathrm{K}$) to improve the signal-to-noise ratio. Furthermore, the speed of the detector is increased because the heat capacity of the detector head is decreased at low temperature. While a classical bolometer makes use of the temperature change of the atomic lattice, Si bolometers are so-called hot-electron bolometers (HEBs) which directly convert a thermally induced change of the electron mobility to the output signal. The Si-based HEB used for THz spectroscopy at DELTA has a response time of about $1\,\mathrm{ms}$. This leads to an integration over roughly 2600 revolutions in the storage ring. Further properties of the detector are summarized in A.2.

A much faster device employed at DELTA is the liquid-nitrogen cooled YBCO [72, 73] (Yttrium barium copper oxide) detector. It features a response time of less than $17\,\mathrm{ps}$ and a sensitive frequency range from $100\,\mathrm{GHz}$ to about $2.5\,\mathrm{THz}$. In this frequency range, a direct observation of the incidient field is possible, allowing to perform phase-sensitive measurements. However, the complete readout chain including amplifier, transmission cables and oscilloscope has to provide a very high bandwidth to make use of this feature. Key parameters of the device can be found in A.3.

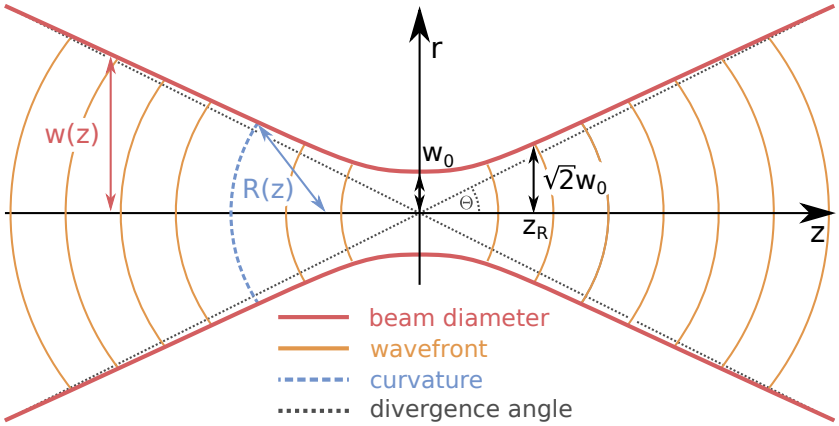

Figure 2.11: The beam waist of a Gaussian beam is the location at which the curvature of the wavefront is infinite. In the limit of infinitely short wavelength λ, the waist radius w_0 decreases and the radius $w(z)$ converges to the dashed line.

2.3.3 Transverse beam properties of electromagnetic radiation

To describe the transverse beam properties of THz radiation, the concept of geometrical optics is insufficient. The wavelength being in the (sub-)millimeter is not negligible in comparison to the beam diameter and the dimensions of relevant optical elements. Therefore, diffractive effects have to be considered. A concept combining ray- and wave optics is the Gaussian beam. The most noticeable difference is that in geometrical optics a beam can be focused to a diameter of $w(z = z_0) = 0$ which is not realistic. Instead, the transverse beam profile is assumed to have an intensity distribution of Gaussian shape with a $1/e^2$ width w and a minimum defined as w_0.

Figure 2.11 shows a sketch of a beam waist of a Gaussian beam. The direction of propagation is along the z axis. In cylindrical coordinates with $r = \sqrt{x^2 + y^2}$, the electrical field $\mathcal{E}(r, z)$ is described as a solution to the paraxial approximation of the wave equation [74] with

$$\mathcal{E}(r,z) = \frac{w_0 \cdot \mathcal{E}_0}{w(z)} \exp\left\{j(\omega t - kz\right\} \exp\left\{j\xi(z)\right\} \exp\left\{-j\frac{kr^2}{2R(z)}\right\} \exp\left\{-\frac{r^2}{w^2(z)}\right\}. \quad (2.50)$$

Away from the beam waist at $z = 0$, the beam diameter grows as [75]

$$w(z) = w_0 \sqrt{1 + \frac{z^2}{z_R^2}} \quad (2.51)$$

with $w_0 = w(0)$. The curvature of the wavefronts varies as

$$R(z) = z\left(1 + \frac{z_R^2}{z^2}\right). \tag{2.52}$$

The Rayleigh length

$$z_R = \frac{\pi\omega_0^2}{\lambda} \tag{2.53}$$

is the distance from the beam waist to the point where the beam area has doubled. The beam divergence is defined by half the far-field opening angle of the beam envelope as

$$\Theta = \arctan\left(\frac{w_0}{z_R}\right) = \arctan\left(\frac{\lambda}{\pi w_0}\right) \tag{2.54}$$

From ray optics, a matrix formalism is known which describes the light propagation by the distance r from the optical axis and the angle r'. A simple matrix formalism describes the transformation of rays from z_1 to z_2 as

$$\begin{pmatrix} r(z_2) \\ r'(z_2) \end{pmatrix} = \begin{pmatrix} A & B \\ C & D \end{pmatrix} \cdot \begin{pmatrix} r(z_1) \\ r'(z_1) \end{pmatrix}. \tag{2.55}$$

A Gaussian beam, however, has to be transformed slightly differently. Instead of (r, r'), the complex beam parameter

$$q(z) = z + q_0 = z + jz_R \tag{2.56}$$

with the imaginary unit j is transformed. Often, the reciprocal definition

$$\frac{1}{q(z)} = \frac{1}{R(z)} - j\frac{\lambda}{\pi w^2(z)} \tag{2.57}$$

is used. It transforms from one position to the other as

$$q_2(z_2) = \frac{Aq_1(z_1) + B}{Cq_1(z_1) + D}, \tag{2.58}$$

with the same matrix elements as in ray optics.

The beam radius at any position is given as function of $q(z)$ as

$$w(z) = \sqrt{-\frac{\mathrm{Im}(1/q(z)) \cdot \lambda}{\pi}} \tag{2.59}$$

In the matrix formalism, a thin lens with focal length f, for example, is modeled by

$$T_f = \begin{pmatrix} 1 & 0 \\ -\frac{1}{f} & 0 \end{pmatrix}. \tag{2.60}$$

and a free-space section of length L is described by

$$T_d = \begin{pmatrix} 1 & L \\ 0 & 1 \end{pmatrix}. \tag{2.61}$$

THz beam paths generally tend to diverge fast due to the large wavelength. In Chap. 4, calculations of THz beam diameters are shown which are based on the matrix formalism for Gaussian beams. The DELTA THz beamline described in Chap. 3 and also the beam transportation to the spectrometers used for the diagnostics of THz radiation rely on these assumptions.

2.3.4 Materials for THz optics

The description of the transverse beam properties of THz radiation leads to the question how to actually influence the transverse beam shape and which materials can be used for focusing optics. Lenses made of Polymethylpentene (TPX) [76] or high-resistivity float zone silicon (HRFZ-Si) [77] are commercially available. Here, $5\,\mathrm{mm}$ thick TPX lenses offer a transmission of $90\,\%$ at a wavelength of $\lambda = 1\,\mathrm{mm}$ while silicon absorbs more radiation and has a typical transmission of $55\,\%$. Both materials are nontransparent for visible radiation and especially for infrared radiation around $10\,\mu\mathrm{m}$ which is important when THz optics is used together with optics of CO_2 lasers of this wavelength. Optics suitable for both, the THz range and the visible regime, are made of z-cut quartz with $30\,\%$ transmission or diamond with a transmission of about $50\,\%$. All transmission values given here were normalized to a thickness of $5\,\mathrm{mm}$ which is typical for lenses but rather thick for windows or beam splitters. Of all these materials, diamond results in the most flat transmission spectrum with only weak absorption around $5\,\mu\mathrm{m}$ wavelength and strong absorption below $225\,\mathrm{nm}$.

Another commonly used method to focus THz light is to use (off-axis) parabolic mirrors or (off-axis) toroidal mirrors made from aluminium with or without gold plating. These mirrors are used to reflect THz light at a given angle of incidence while simultaneously focusing the light. Here, a symmetric concave mirror holding a spherical cut would introduce an astigmatism because the effective focal lengths differ in the horizontal and vertical plane. To avoid that, different radii of curvature are needed horizontally and vertically, respectively, which leads to the use of paraboloidal or toroidal mirrors. These mirrors have different radii of curvature in the meridional plane (defined by the incoming and outgoing optical axis) and the sagittal plane (the plane perpendicular to the meridional plane). To achieve the same focusing strength in both planes, a toroidal mirror for an angle of incidence $\theta = 45°$, for example, has the radii of curvature

$$R_\mathrm{s} = 2\sqrt{2}f \qquad \text{and} \qquad R_\mathrm{m} = \sqrt{2}f \ . \tag{2.62}$$

In Chap. 4, a THz spectrometer is presented which uses polarizing beamsplitters. In the THz range, the use of dielectric beamsplitters is not advisable due to absorption losses in the material, but highly efficient linear polarizers can be made of grids comprising free-standing, conducting wires. Typically, gold-plated tungsten is used because tungsten ensures the mechanical stability and the conductivity of gold leads to a reflectivity of close to $100\,\%$ [78, 79]. Figure 2.12 illustrates the reflection of THz radiation being polarized parallel to the wire orientation while the perpendicular polarization component passes the filter. The reflectivity of the radiation component parallel to the wire direction is [80, 81]

$$R_p = \frac{1}{1 + (S/\lambda)^2)\ln(S/(\pi d)} \tag{2.63}$$

and the orthogonal reflectivity reads

$$R_n = \frac{(\pi d)^4}{(2S\lambda)^2[1 + (\pi d)^4/(2S\lambda)^2]} \tag{2.64}$$

with the wire diameter d, the wire pitch S and the radiation wavelength λ. For an angle of incidence of $45°$, a ratio $S/d = 5$ is optimal [81]. Lower values lead to a strong high-pass frequency characteristic since the fraction of the polarizer aperture covered by metal is larger.

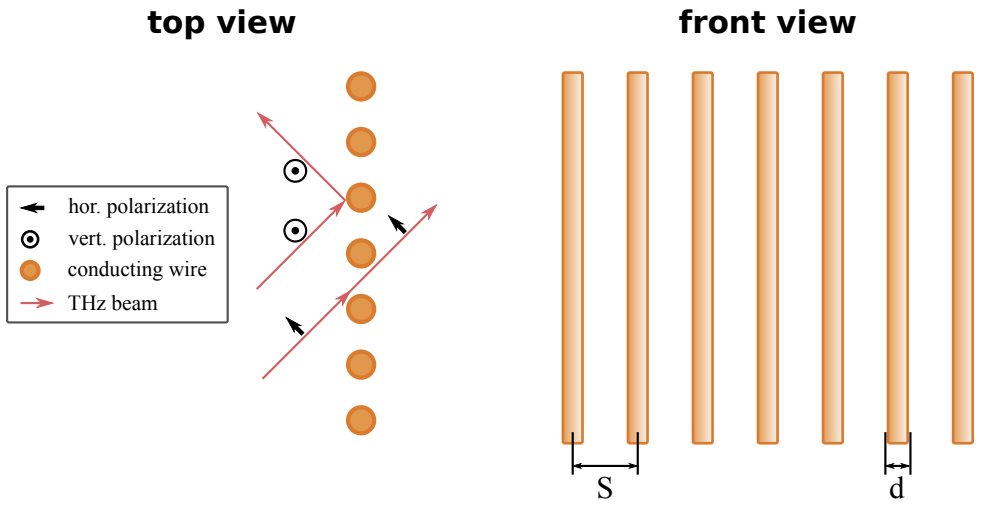

Figure 2.12: Free-standing wire grid used as a THz polarizer. The conducting wires (typically made of gold-plated tungsten) reflect light with polarization parallel to the wire orientation. The orthogonal polarization is transmitted. The ratio of wire distance and wire thickness determines the spectral high-pass characteristics of the polarizer (see text for details).

2.4 Lasers

The development of pulsed lasers has strongly influenced new developments in accelerator physics. In this thesis, experiments were carried out in which the electrical field of a laser pulse modulates the energy of relativistic electrons in a storage ring. The invention of pulsed lasers led to a drastically increased peak field in laser pulses. Shortest laser pulses are generated by the so-called mode-locked operation which is explained in this section.

2.4.1 Pulsed Lasers

The laser system used in the scope of this thesis is an $800\,\mathrm{nm}$ short-pulse laser system based on Ti:sapphire as laser medium. The emission spectrum of Ti:sapphire ranges from $650\,\mathrm{nm}$ to $1050\,\mathrm{nm}$ [82]. Hence, a large number of longitudinal modes fulfill the standing-wave condition which restricts lasing to wavelengths λ_j which are an integer divider k of twice the cavity length L. These wavelengths are given by

$$\lambda_j = \frac{2L}{k} \,. \tag{2.65}$$

The emission of the light from the these modes occurs with random phase in the first place. However, it was experimentally proven in 1986 [82] that a Ti:sapphire laser can

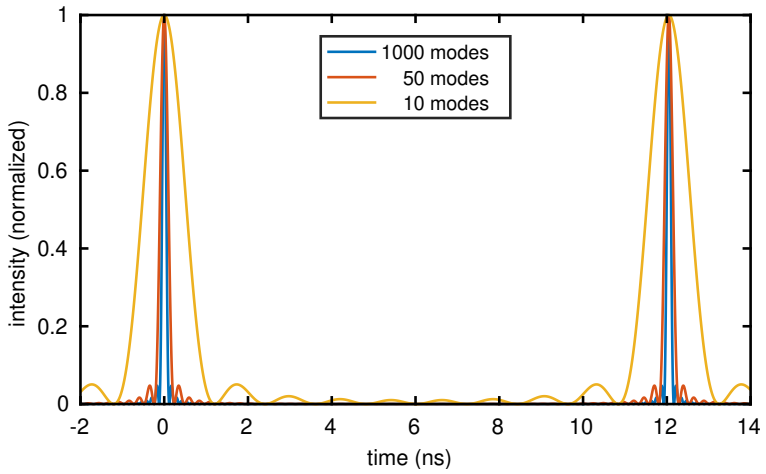

Figure 2.13: Train of laser pulses generated from few phase-locked longitudinal laser modes. Ten modes (yellow), 50 modes (red) and 1000 modes (blue) are summed up at correct phase and the normalized intensity is calculated. The pulse duration shrinks with an increasing number of modes. The constant phase relation leads to constructive interference at delays of the pulse period. For better visibility, only few laser modes contribute. Broadband lasers, like the Ti:sapphire laser, can reach phase locking of up to 850000 modes.

be operated with fixed phase relationship of the laser modes. This concept called mode-locking leads to constructive interference and the formation of ultrashort pulses. The repetitiion rate f_{rep} of the pulses is given by

$$f_{\mathrm{rep}} = \delta\nu = \frac{c}{2L} \,. \tag{2.66}$$

Active methods to achieve mode-locking are, e.g., acousto-optic or electro-optic modulators. Passive mode-locking is realised through the Kerr-lens effect or saturable absorbers which introduce cavity losses that depend on the peak laser power [83,84]. The Ti:sapphire laser oscillator at DELTA employs a Kerr-lens which favors the modelocked operation due to increased losses in CW mode. Passive mode-locking techniques can achieve much stronger pulses than active techniques, but startup problems of the mode-locking formation are common.

Figure 2.13 shows a simplified illustration of the mode-locking process and the laser pulse evolution. Here, different numbers of modes are summed up at correct phase and the normalized intensity is calculated. The pulse duration shrinks with an increasing number of modes.

Ultrashort laser pulses can be described as time- and space-dependent electromagnetic waves. The spatial dependence of the beam is modeled very well by a Gaussian beam

(see Sec. 2.3.3) which was already used to characterize THz beams. The ideal temporal distribution is of a Gaussian shape in time domain which necessarily requires a Gaussian shape in frequency domain. In a real laser, shape and duration of the pulse depend on the emission spectrum of the laser medium, the bandwidth of the cavity optics and the dispersive properties of the cavity setup. The electric field of a Gaussian pulse $\mathcal{E}(t)$ reads

$$\mathcal{E}(t) = \mathcal{E}_0 \cdot \exp(-\Gamma t^2) \cdot \exp(j\omega_0 t) \tag{2.67}$$

with the $\Gamma = a - jb$ and the temporal phase $\varphi(t) = \omega_0 t + bt^2$. In the course of this thesis, the laser phase is treated in spectral domain and the temporal phase has to be distinguished from that phase.

The parameter a is determined by the rms pulse according to $a = 1/(4\sigma_t^2)$, which can be expressed as the full width at half maximum duration (FWHM) $\Delta t = 2\sqrt{2\ln 2}\,\sigma_t$. The parameter b determines the so-called chirp which is the variation of the instantaneous frequency along the temporal coordinate of the pulse. A more common expression for the chirp in the spectral domain is given later in this chapter. The time derivative of the temporal phase

$$\omega(t) = \frac{\mathrm{d}\varphi(t)}{\mathrm{d}t} = \omega_0 + 2 \cdot t \tag{2.68}$$

defines the instantaneous frequency $\omega(t)$ of the pulse.

2.4.2 Pulse complexity

A laser pulse is fully characterized by its electric field $\mathcal{E}(t)$. However, for laser radiation near the visible range of the electromagnetic spectrum it is often technically impossible to experimentally access $\mathcal{E}(t)$. In these cases, pulse diagnostics in the spectral domain is much more feasible. The Fourier transform

$$\mathcal{E}(t) = \frac{1}{2\pi} \int_{-\infty}^{\infty} \tilde{\mathcal{E}}(\omega) \exp(-j\omega t)\,\mathrm{d}\omega \tag{2.69}$$

defines the relation between spectral domain and time domain as a mathematical base change to sine and cosine as a set of orthogonal functions. Hence, the full information about the pulse is contained in $\tilde{\mathcal{E}}(\omega)$ as well. Here, the pulse is defined by the spectral amplitude $A(\omega)$ and spectral phase $\phi(\omega)$ with $\tilde{\mathcal{E}}(\omega) = A(\omega)\exp\{j\phi(\omega)\}$. If the spectral phase $\phi(\omega)$ is a linear function of ω, the shortest possible pulse length is achieved and

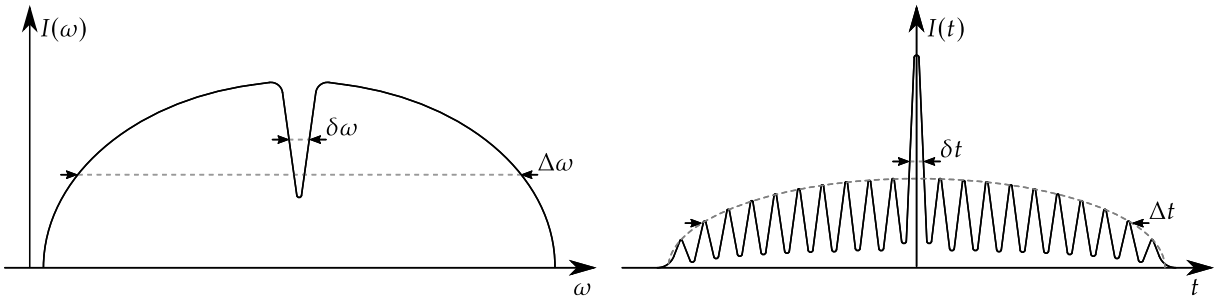

Figure 2.14: The complexity of a laser pulse is the ratio of the smallest and largest structure either in spectral domain (left) or time domain (right).

this condition is referred to as a Fourier-limited pulse. The pulse length is then fully determined by the spectral width of the pulse. The time-bandwidth product

$$\mathrm{TBP} = \Delta t_0 \cdot \Delta\omega \tag{2.70}$$

is the product of the temporal duration (FWHM) Δt_0 and the spectral bandwidth (FWHM) $\Delta\omega$. In the case of a Gaussian pulse shape TBP ≥ 0.44 holds. The minimum is reached in the Fourier limit.

Another measure which has a comparable meaning, but which is more often used in the context of spectro-temporal shaping of pulses, is the pulse complexity [85]

$$\eta = \frac{\Delta t}{\delta t} = \frac{\Delta\omega}{\delta\omega} \tag{2.71}$$

with δt and $\delta\omega$ being the smallest and Δt and $\Delta\omega$ being the largest features in temporal and spectral shape, respectively. Figure 2.14 illustrates the meaning of the complexity in that context.

For a pulse with Gaussian spectrum, the complexity is $\eta = \mathrm{TBP}/(4\ln 2)$. Generally, the complexity η that can be reached is a limiting factor, in any pulse shaping setup. In Chap. 5, computer-controlled adaptive optics, which apply a frequency-dependent phase shift, are used. These offer high flexibility due to their large number of degrees of freedom. Phase-shifters for pulse shaping reached a maximum complexity [86] of about 600. However, a much simpler setup like a Michelson interferometer, which delays two $50\,\mathrm{fs}$ long pulses by $100\,\mathrm{ps}$, easily reaches a complexity of $\eta = 2000$. This emphasizes that complexity is not a matter of flexibility in pulse shape.

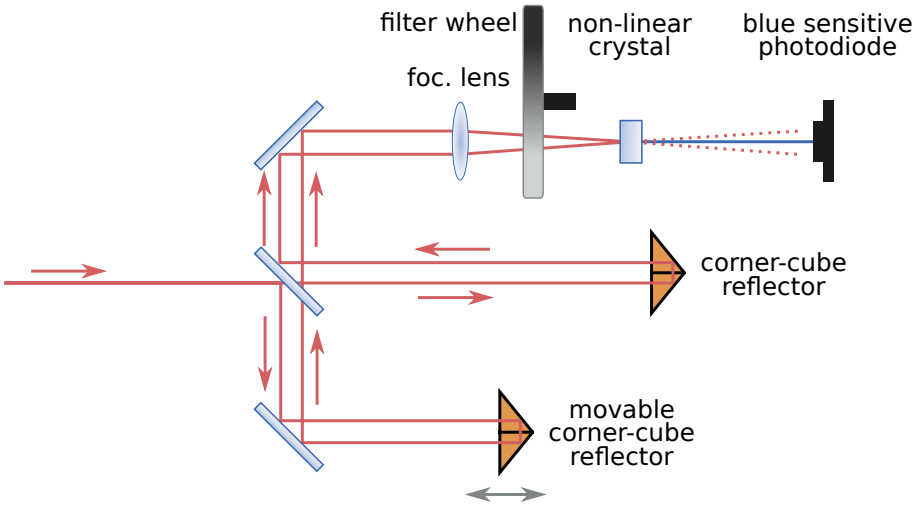

Figure 2.15: Sketch of a background-free autocorrelator. The incoming beam is divided into two beams by a 50:50 beam splitter. After passing corner-cube reflectors, the two beams are delayed and recombined in a second-harmonic generation (SHG) crystal by a focusing lens. Three beams exit the crystal. The central beam being the second harmonic of the combined signal is analyzed by an IR-blind photodiode.

2.5 Temporal diagnostics of pulsed optical radiation

The goal of this thesis is to implement different pulse shaping schemes for laser radiation to control the generation of THz radiation based on a laser-electron interaction. Typical devices used for the diagnostics of (ultra-)short laser pulses which were used in this thesis, are described in the following.

2.5.1 Autocorrelation

Autocorrelation in general is a technique to characterize a time-dependent signal by determining the correlation with a delay of the original signal. In optics, two different kinds of autocorrelation are used to estimate the pulse duration or the temporal shape of the intensity. Here, only the intensimetric autocorrelation [87] is described whereas more information on interferometric autocorrelation can be found in [88].

As depicted in Fig. 2.15, a scanning intensity autocorrelator consists of a Michelson interferometer to create a pulse copy which is shifted in time. In the so-called background-free configuration, the two beams are guided with a lateral offset and are recombined by

a focusing lens at a crossing angle inside a crystal with significant non-linear dielectric susceptibility $\chi^{(2)}$. In general, polarization inside media is described by [2, 89]

$$P = \epsilon_0 \chi^{(1)} \mathcal{E}(t) + \epsilon_0 \chi^{(2)} \mathcal{E}^2(t) + \dots \,. \tag{2.72}$$

If a strong field $\mathcal{E}(t) = \mathcal{E}_0 \sin(\omega t)$ is present, the second term causes a polarization

$$P^{(2)} = \epsilon_0 \chi^{(2)} \mathcal{E}^2(t) = \epsilon_0 \chi^{(2)} \mathcal{E}_0^2 \sin^2(\omega t) = \epsilon_0 \chi^{(2)} \mathcal{E}^2 \left(\frac{1}{2} - \frac{\cos(2\omega t)}{2} \right). \tag{2.73}$$

This means that after an excitation of the medium at ω, a re-emission process at the doubled frequency occurs. Due to energy and momentum conservation in the crystal, the two primary beams leave the crystal at an angle, but the second harmonic is generated on-axis.

The output intensity I_{out} of an intensity autocorrelator is

$$\begin{aligned} I_{\text{out}} &\propto |\mathcal{E}(t) + \mathcal{E}(t-\tau)|^2 && (2.74)\\ &\propto |\mathcal{E}^2(t)|^2 + 2|\mathcal{E}(t)\mathcal{E}(t-\tau)|^2 + |\mathcal{E}^2(t-\tau)|^2 && (2.75)\\ &\propto \underbrace{I^2(t)}_{\omega} + \underbrace{2I(t)I(t-\tau)}_{2\omega} + \underbrace{I^2(t-\tau)}_{\omega} && (2.76) \end{aligned}$$

with a variable time delay τ and the electrical fields $\mathcal{E}(t)$ and $\mathcal{E}(t-\tau)$. If the beams are combined in the crystal at a crossing angle, the three intensity terms leave the crystal at different angles which makes a separation very feasible. Moreover, the on-axis radiation is frequency doubled with respect to incoming beam because of the SHG (second-harmonic generation) crystal.

Although intensity autocorrelation is not a phase-sensitive method for pulse characterization, it is a useful method to measure the intensity modulation of a laser pulse. An autocorrelator of this kind was built within this thesis to characterize modulated laser pulses. The setup employs a crystal of barium boron oxide (BBO) also known as β-barium borate cut at $29°$ with a thickness of $0.2\,\text{mm}$. The cutting angle is important for the efficiency of the SHG process. The on-axis radiation has a wavelength of $400\,\text{nm}$. Although the primary beams and autocorrelation beam are transversely separated, a gallium-phosphide photodiode is used which is only sensitive below $550\,\text{nm}$.

Further details about the setup can be found in A.5. Measurements carried out using the device are shown in Chap. 5. Autocorrelation is a reliable technique to detect intensity modulations. However, it has to be noted that due to the symmetry of the setup, sub-

structures may be suppressed. Additionally, short intensity features may be washed out in the autocorrelation signal.

2.5.2 Frequency-resolved optical gating

Another self-referenced characterization for laser pulses is called frequency-resolved optical gating (FROG) [90, 91]. The main idea is to temporally gate the test laser pulse with a reference pulse and measure the resulting spectrum as function of the delay τ between the respective pulses. A two-dimensional spectrogram

$$S(\tau, \omega) \propto \left| \int \mathcal{E}(t)\mathcal{G}(t-\tau)\exp(j\omega t)\mathrm{d}t \right|^2 \tag{2.77}$$

is recorded. This is realized by overlapping a pulse with a gate pulse in an SHG crystal while measuring the SHG spectrum. Spectral phase and amplitude are extracted from the resulting two-dimensional map $S(\tau, \omega)$. Here, it is beneficial that extracting the phase information from $S(\tau, \omega)$ is mathematically equivalent to phase retrieval problems in other fields and iterative algorithms exist to determine the phase. In the simplest case, the gate pulse $\mathcal{G}(t)$ is identical to the pulse to be analyzed, but ideally a gate pulse with well-known spectral amplitude and phase is used.

Different implementations of FROG exist of which SHG-FROG is the most-widely used. The technical implementation equals the autocorrelator setup shown in Fig. 2.15 except that the photodiode is replaced by a spectrometer. The test pulse $G(t-\tau)$ then is simply $G(t-\tau) = \mathcal{E}(t-\tau)$ and the spectrogram reads

$$S(\tau, \omega) \propto \left| \int \mathcal{E}(t)\mathcal{E}(t-\tau)\exp(j\omega t)\mathrm{d}t \right|^2 . \tag{2.78}$$

An implementation of SHG FROG without a moving delay line is called GRENOUILLE[2]. Here, a combination of a cylindrical lens and prism are used to shear the beam in the crystal so that a time delay variation is reached along the horizontal coordinate of the crystal which can be imaged with a camera which directly acquires $S(\tau, \omega)$. More information on this setup can be found in [92, 91]. A GRENOUILLE FROG was available for measurements in this thesis, however, the maximum laser pulse length the device can handle is $150\,\mathrm{fs}$. Hence, the characterization of longer pulses was carried out by an intensity autocorrelation and only fully compressed pulses where characterized by the FROG.

[2]GRENOUILLE: **Gr**ating-**e**liminated **n**o-nonsense **o**bservation of **u**ltrafast **i**ncident **l**aser **l**ight **E**-fields, la grenouille: french for "frog"

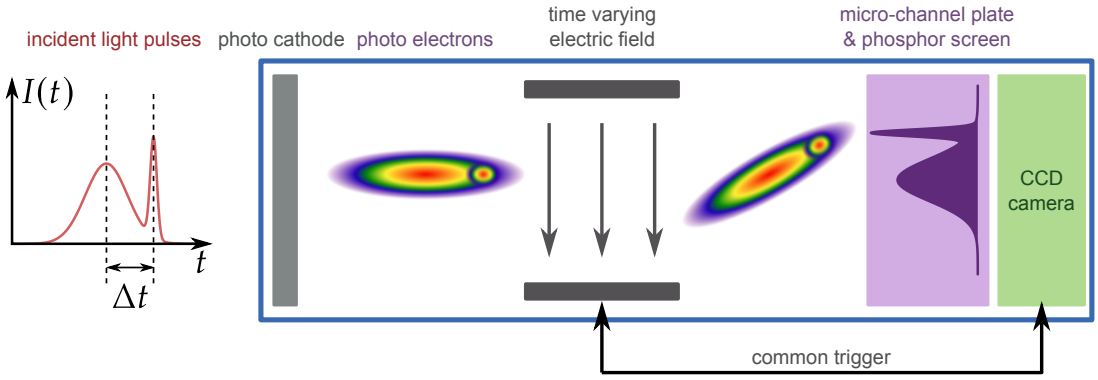

Figure 2.16: Working principle of a streak camera. See text for details.

2.5.3 Streak camera

Another device for the diagnostics of periodically pulsed optical radiation which is typically used at synchrotron radiation sources, is the streak camera. It allows for an incoherent detection of pulses with a typical resolution of several picoseconds [93, 94].

Figure 2.16 shows the basic principal of a streak camera. The light pulse is focused onto the input slit and hits a photo cathode where a number of photo electrons proportional to the light intensity is emitted. The temporal shape of the light pulse equals the temporal shape of the photo electron ensemble.

A voltage of several hundred volt is used to accelerate the photoelectrons away from the photo cathode. An additional voltage with fast oscillating field is applied to a pair of electrodes causing a transverse acceleration of the photo electrons. The time-dependent field leads to a tilt of the electron ensemble which now has a correlation between transverse position and arrival time. Hence, an image taken by a two-dimensional CCD camera after a phosphor screen and a micro-channel plate for image intensifying contains the temporal shape of the initial light pulse. Often, the high-voltage pulse is generated by a photoconductive switch if laser radiation is diagnosed. However, for measurements in this thesis a streak camera was used which relied on a synchronization with an externally provided RF signal of $125\,\mathrm{MHz}$. The synchronization signal is a frequency-divided signal from the accelerator RF system working at $500\,\mathrm{MHz}$.

As the short-pulse laser used at DELTA is synchronized to the storage ring RF system, both, laser radiation and synchrotron radiation, can be observed with the streak camera. To detect temporal variations between the observed light pulses and the reference RF signal, many streak cameras allow to apply a second voltage to another set of electrodes with an orientation perpendicular to the first pair of deflection plates. In this way, periodic phase changes and pulse length can be imaged in two dimensions on the

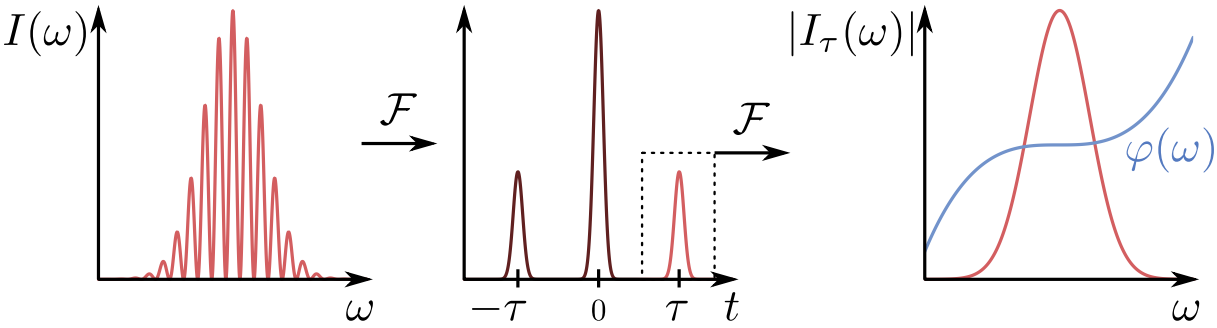

Figure 2.17: Left: The spectrum of a test pulse and a delayed reference pulse exhibits interference fringes. Center: The Fourier transform of the spectrum shows a central peak and symmetric sidebands at the delay $\pm\tau$. Right: The spectral phase of the test pulse can be retrieved if the reference pulse is fully characterized (see text for details).

CCD camera [95]. The operation mode is often called synchroscan. In this thesis, the streak camera is mainly used to find the temporal overlap of laser pulses and electron bunches. This is realized by equalizing the arrival time of laser pulses and synchrotron light pulses emitted by the electron bunch. Furthermore, it was used to measure intensity modulations of laser pulses before the self-built autocorrelator was available.

2.5.4 Spectral interferometry

The relation of temporal and spectral shape is given by the complex Fourier transform. As pointed out in the previous section, Fourier-limited pulses of known shape can be fully characterized by their amplitude spectrum. If these special conditions are not fulfilled, spectral measurements are still of use if a reference pulse exists.

In this thesis, twin pulses generated in a Michelson interferometer were used to interact with longitudinally displaced regions of an electron bunch. A way to get more information about such a double-pulse train is spectral interferometry [96,97,99,98]. Here, the spectrum of a test pulse $\mathcal{E}(t)$ is measured first. Next, the spectrum of the pulse together with a reference pulse $\mathcal{E}_{\mathrm{ref}}$ delayed by τ is measured. The spectrum now exhibits fringes from the temporal interference of the two pulses (c.f. Fig. 2.17). The spectrometer signal reads [99]

$$I(\omega) \propto \left|\tilde{\mathcal{E}}(\omega) + \tilde{\mathcal{E}}_{\mathrm{ref}}(\omega)\exp(j\omega\tau)\right|^2 \tag{2.79}$$

$$\propto A^2(\omega) + A^2_{\mathrm{ref}}(\omega) + 2A(\omega)A_{\mathrm{ref}}(\omega)\cdot\cos\{\varphi(\omega) - \varphi_{\mathrm{ref}}(\omega) - \omega\tau\} \tag{2.80}$$

with the spectral amplitudes $A(\omega)$ and $A_{\mathrm{ref}}(\omega)$.

The spectral structure described by the cosine term is visible as a modulation with a frequency of $1/\tau$. However, there is a second phase term being $\varphi(\omega) - \varphi_{\text{ref}}(\omega)$ which can be interpreted in the picture of a frequency modulation. The delay corresponds to a carrier frequency which is modulated by the phase difference of the two pulses. If the pulses are identical, the phase difference is zero and the modulation is purely caused by the delay. Then, the delay can be precisely measured from this oscillation. More information is gained if the reference pulse has a well-known spectral phase being different from the test pulse. Fourier-transforming the amplitude spectrum gives a central peak and two sidebands separated by the delay. Only back-transforming the sideband yields

$$I_\tau(\omega) = A(\omega)A_{\text{ref}}(\omega)\exp\left\{j(\varphi(\omega) - \varphi_{\text{ref}}(\omega) - \omega\tau)\right\}. \tag{2.81}$$

This method is known as Fourier filtering as only the side band is analyzed. Figure 2.17 (right) depicts the phase retrieval by the second Fourier transform.

2.6 Dispersion control and shaping of optical pulses

The previous section covered the retrieval of spectral phase and spectral amplitude to characterize a laser pulse. The pulse length and more generally its shape is essentially influenced by the phase.

Again, the description of the pulse can either be expressed in frequency domain or in time domain. The different meaning of spectral phase $\varphi(\omega)$ and temporal phase $\phi(t)$ is easily confused. In the following, only the spectral description is given, but the perspective can be changed to time domain by a Fourier transform. Expanding the spectral phase as a Taylor series helps to identify ways to manipulate the spectro-temporal behavior of a laser pulse. The expansion reads

$$\varphi(\omega) = \varphi_0 + D_1 \cdot (\omega - \omega_0) + D_2 \cdot (\omega - \omega_0)^2 + D_3 \cdot (\omega - \omega_0)^3 + \ldots. \tag{2.82}$$

The coefficients have different effects on the laser pulse:

- φ_0 is the absolute phase, or the carrier-envelope phase (CEP). It is the relative phase between the envelope of the electric field and the carrier. This phase is important to reach the highest electric peak field. In some applications, laser pulses are so short that the field envelope only covers a few cycles. Here, it is important to achieve a stable relation between envelope and carrier [100].

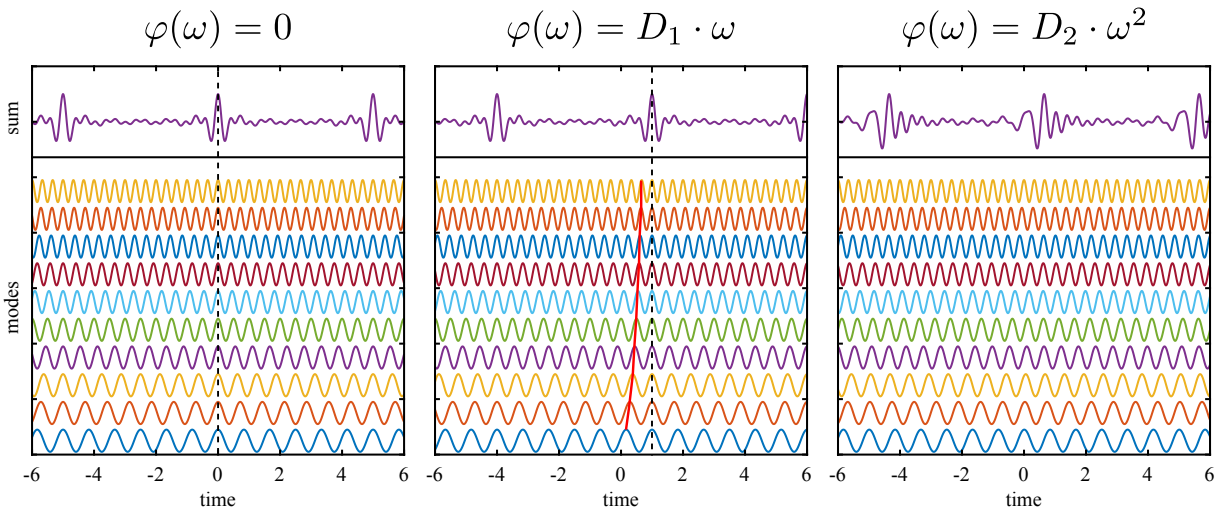

Figure 2.18: Effect of different orders of dispersion. Left: Ten longitudinal modes are aligned without phase delay. The pulse (purple) is fully compressed. Center: A linear variation of the phase with frequency leads to a delay of the pulse. The red line indicates the shift of the maxima for each mode next to the pulse center. Right: A quadratic phase shift leads to a chirp of the resulting pulse. A variation of frequency with time and pulse broadening is clearly visible.

- D_1 is the delay between the pulse and an arbitrary origin of time. It is a constant group delay leading to a simple shift in time.
- D_2 is known as the chirp of the pulse. It not only leads to an increase of pulse length, but also introduces a time dependence of the instantaneous frequency as each frequency experiences a different time shift. More specifically, while sweeping the frequency, the phase advance increases linearly.
- D_3 is the cubic phase term. Pre- and post pulses are generated by the cubic phase which is also known as third-order dispersion (TOD).

The effect of different orders of dispersion is illustrated in Fig. 2.18. Here, a set of 10 longitudinal modes interferes without phase delay (left) which leads to a fully compressed pulse. A phase which linearly depends on the frequency of the mode (center), leads to a shift of the sum pulse. A quadratic variation of the phase (right) changes the pulse length and leads to a frequency variation in time.

In this thesis, only second-order and third-order dispersion are regarded when correcting the spectral phase. However, in the application of ultra-high power lasers [101] the correction of higher orders improves the time-bandwidth product and brings the pulse near the Fourier limit.

2.6.1 Grating compressors

Many applications demand a method to compress a chirped laser pulse either to control a temporal behavior on a short timescale or to drastically increase the peak intensity of a laser pulse. To achieve that, an optical setup with controllable dispersion is needed. The laser system used in this thesis employs the chirped-pulse amplification (CPA) scheme where a comparatively long laser pulse is amplified to avoid damage of the laser crystal caused by a high peak intensity. After the amplification, a grating compressor is used to reduce the pulse length.

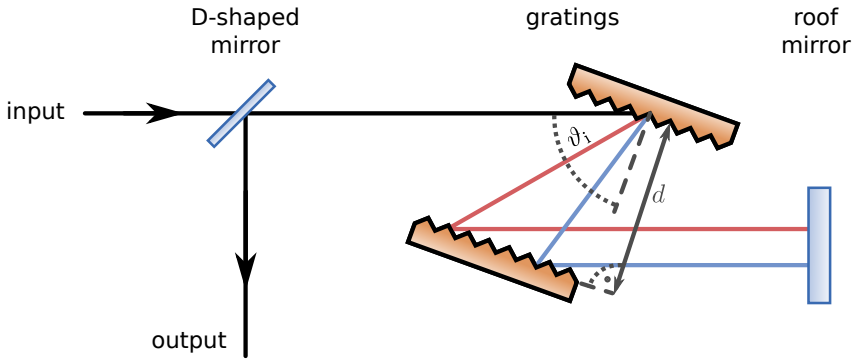

Figure 2.19: Geometrical arrangement of a grating compressor for laser pulses. A laser pulse enters the compressor at an angle of incidence ϑ_i at the first grating. The blue and red lines indicate different paths for different wavelengths. After passing a second grating, the spatially chirped beam is recombined by being sent back after a beam height change at a roof mirror. The path length is correlated with the wavelength. Longer wavelength components experience a larger delay.

Figure 2.19 shows a sketch of a four-grating compressor which is built of two gratings being passed by the laser pulse twice. This arrangement is also known as Treacy-type compressor. The input beam is dispersed at both gratings which are oriented in parallel. The beam is then reflected at a roof mirror changing the height of the beam. After passing the grating arrangement a second time, the beam is reflected at a D-shaped mirror to exit the compressor arrangement. The wavelength-dependent diffraction angles yield a chromatic delay which depends on the distance of the gratings d and the angle of incidence on the first grating ϑ_i.

The diffraction at a single grating is defined by the grating equation [102]

$$m\lambda = g \cdot \{\sin(\vartheta_i) + \sin(\vartheta_o)\}\,. \tag{2.83}$$

Here, m is the dispersion order, g is the grating line period and ϑ_i and ϑ_o are input and output angles, respectively. In the so-called Littrow configuration, the input angle and output angle are equal and the Littrow angle $\vartheta_\mathrm{Littrow}$ reads

$$\vartheta_\mathrm{Littrow} = \vartheta_\mathrm{i} = \vartheta_\mathrm{o} = \arcsin\left\{\frac{n\lambda}{2\cdot d}\right\}. \tag{2.84}$$

This arrangement, which is sometimes used in laser resonators, allows to use a grating as a mirror, but, of course, $\vartheta_\mathrm{i} = \vartheta_\mathrm{o}$ is only fulfilled for a specific wavelength. The group delay $\tau = D_1$ introduced by the compressor is [102]

$$D_1 = \frac{d\left\{1+\cos(\vartheta_\mathrm{i})\right\}}{c}. \tag{2.85}$$

For practical applications, it is worth mentioning that every change of the grating distance leads to a global time shift D_1 of the pulse. The setup depicted in Fig. 2.19 can be adapted to correct length changes inherently. This requires a co-moving delay line reversing the time shift which is connected to the translation mechanism of the movable grating.

The group delay dispersion (GDD) D_2 introduces the chirp of the laser pulse, i.e., the correlation between frequency and time. The GDD of a grating compressor is [102]

$$D_2 = -2\frac{4\pi^2 cd}{\omega_0^3 g^2}\left[1-\left(\frac{2\pi c}{\omega_0 g}-\sin\vartheta_\mathrm{i}\right)\right]^{-\frac{3}{2}} \tag{2.86}$$

and the third-order dispersion (TOD) reads [102]

$$D_3 = -\frac{D_2}{2\omega_0}\cdot\frac{1+\frac{2\pi c}{\omega_0 g}\sin\vartheta_\mathrm{i}-\sin^2\vartheta_\mathrm{i}}{1-\left(\frac{2\pi c}{\omega_0 g}-\sin\vartheta_\mathrm{i}\right)^2}. \tag{2.87}$$

The TOD D_3 is a linear function of the second-order dispersion D_2. In consequence, any change of the grating distance will affect both, GDD and TOD.

A given dispersion D_2 influences a fully compressed pulse of duration Δt_0 in the way that the pulse duration increases to [102]

$$\Delta t_1 = \Delta t_0\sqrt{1+\left(\frac{4D_2\ln 2}{\Delta t_0^2}\right)^2}. \tag{2.88}$$

At full compression, the laser pulse length is limited by the time-bandwidth product with an electric field

$$\mathcal{E}_0(t) = \mathcal{E} \cdot \exp\{-a_0 t^2\} \cdot \exp\{j\omega_0 t\} \quad \text{with} \quad a_0 = \frac{2\ln 2}{\Delta t_0^2}\,. \tag{2.89}$$

The eletric field including dispersion up to the second order D_2 reads

$$\mathcal{E}_1(t) = \mathcal{E}\sqrt{\frac{\Delta t_0}{\Delta t_1}} \cdot \exp\{-a_1 t^2\} \cdot \exp\{j\omega_0 t + jb_1 t^2\} \tag{2.90}$$

with

$$a_1 = \frac{2\ln 2}{\Delta t_1^2} \qquad \text{and} \quad b_1 \approx \frac{2\ln 2}{\Delta t_1 \Delta_0}\,. \tag{2.91}$$

Here, the approximation holds for $\Delta t_1 \gg \Delta t_0$.

In standard operation at DELTA, the laser employs a grating compressor to reach shortest pulses with a duration of about $40\,\mathrm{fs}$. As will be explained in Chap. 5, the compressor was detuned to obtain laser pulses of longer duration. Different methods were tested to correct unwanted TOD of laser pulses with durations of up to $20\,\mathrm{ps}$.

2.6.2 Fourier optics

The Fourier transformation plays an important role in optics. While mostly used to choose the right perspective either in time domain or in spectral domain, it can give access to the spatial domain when used to describe Fraunhofer diffraction. In this section, the idea of shifting the spectral phase in the spatial domain is derived mathematically in view of classic diffraction theory. The basics of this so-called Fourier optics are explainend in [103, 104, 105] more detailed.

If a plane wave

$$\mathcal{E}_p(x, y, z) = \mathcal{E}_0 \exp\{j(kz - \omega t\} \tag{2.92}$$

advancing in z direction approaches a diffracting object at $z = 0$ with a complex transfer function $T(x, y)$ with $|T| \leq 1$, the electric field after the diffraction reads

$$\mathcal{E}^T(x, y, z) = T(x, y)\mathcal{E}_p(x, y, z). \tag{2.93}$$

Amplitude and phase of T model the attenuation and phase shifting behavior of the object. This arrangement of diffraction plane and observer plane is depicted in Fig. 2.20. In the Fresnel approximation, propagation near the optical axis at small angles is considered. The approxmation reads

$$\mathcal{E}_{\text{Fresnel}}(x,y,z) = \frac{je^{jkz}}{\lambda z} \int\int T(x,y)\, \mathcal{E}(x',y',z=0)\, e^{j\frac{\pi}{\lambda z}((x-x')^2+(y-y')^2)} \mathrm{d}x'\mathrm{d}y' \,. \quad (2.94)$$

Further assuming that the observation plane is much wider than the diffraction plane and $z \gg z'$ yields the Fraunhofer diffraction integral

$$\mathcal{E}_{\text{FH}}(x,y,z) = \frac{je^{jkz}}{\lambda z} e^{j\frac{\pi}{\lambda z}(x^2+y^2)} \int\int T(x,y)\, \mathcal{E}(x',y',z=0)\, e^{-j\frac{2\pi}{\lambda z}(xx'+yy')} \mathrm{d}x'\mathrm{d}y' \,. \quad (2.95)$$

The definition of spatial frequencies $\nu_x = x/(\lambda z)$ and $\nu_y = y/(\lambda z)$ allows to express the field distribution in form of a two-dimensional Fourier transform multiplied by a quadratic phase term

$$\mathcal{E}(x,y,z) = \frac{je^{jkz}}{\lambda z}\, e^{j\frac{\pi}{\lambda z}(x^2+y^2)}\, \mathcal{F}\left\{T(x,y)\, \mathcal{E}(x',y',z=0)\right\}(\nu_x,\nu_y) \,. \quad (2.96)$$

In reality, the far-field approximation can be realized by a lens imaging the diffraction plane. An optical setup following this approach is shown in Fig. 2.21. Here, the diffracting element is a vertical-line grating which is placed in the image plane of a focusing lens. The lens with a focal length f adds a phase shift

$$\varphi(x,y) = -\frac{\pi(x^2+y^2)}{\lambda f} \,. \quad (2.97)$$

To determine the effect of the lens, the field at a distance $z = f$ has to be evaluated. Since the diffracting object, the lens, is located at $z = 0$, the image plane of the lens is $z = f$. As this distance does not fulfill the far-field approximation, the Fresnel approximation is used. Equation 2.94 is a function of $x-x'$ and $y-y'$ and it can be treated as a convolution of an impulse response function $h(x,y,z)$ and the field $\mathcal{E}^T(x',y',z=0)$ with

$$\mathcal{E}(x,y,z) = \mathcal{E}^T(x',y',z=0) * h(x,y,z) \quad \text{with} \quad h(x,y,z) = \frac{je^{jkz}}{z\lambda} e^{j\frac{\pi}{\lambda z}(x^2+y^2)} \quad (2.98)$$

and the $*$ being the convolution operator.

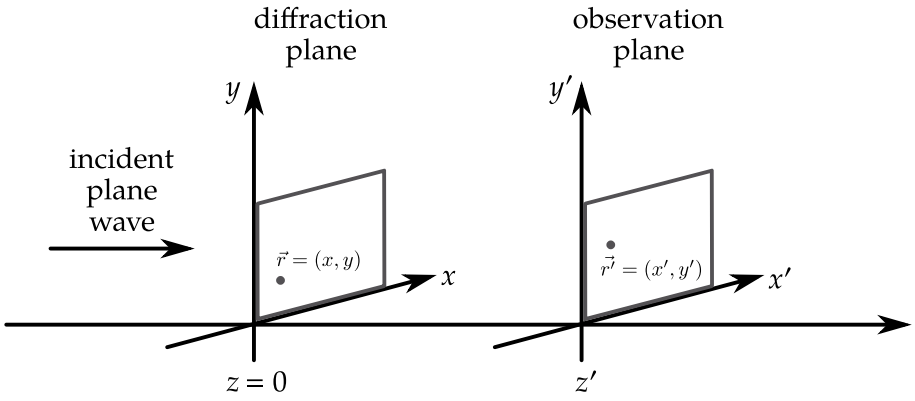

Figure 2.20: Generalized view of diffraction of a plane wave by an object at $z = 0$ and observer at z' (see text for details).

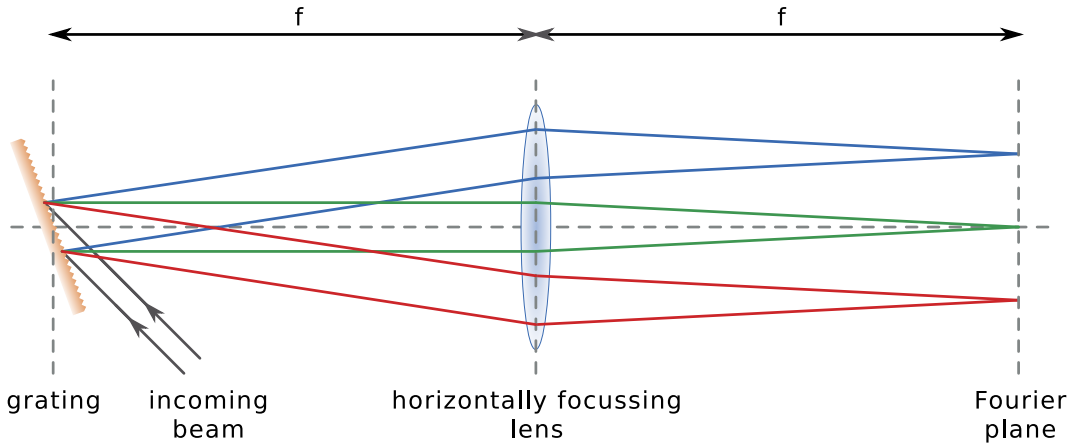

Figure 2.21: Sketch of a 2-f line to create a transversely chirped beam. The setup is also regarded as an optical Fourier transform because in the Fourier plane, a correlation between spatial coordinate and frequency is created.

Applying another transfer function $T_{\text{lens}} = e^{j\varphi}$ and evaluating the Fresnel integral at $z = 2f$, the focal point after the lens, yields

$$\mathcal{E}(x'', y'', z = 2f) = \frac{je^{jkf}}{f\lambda} \int\int \mathcal{E}(x, y, z = f) e^{-j\frac{\pi}{\lambda f}(x^2+y^2)} e^{j\frac{\pi}{\lambda f}((x-x'')^2+(y-y'')^2)} \mathrm{d}x\mathrm{d}y \tag{2.99}$$

$$= \frac{je^{jkf}}{\lambda f} e^{-j\frac{\pi}{\lambda f}(x''^2+y''^2)} \int\int \mathcal{E}(x, y, z = f) e^{-j\frac{2\pi}{\lambda f}(xx''+yy'')} \mathrm{d}x\mathrm{d}y. \tag{2.100}$$

A comparison with Eq. 2.95 reveals that Eq. 2.100 can be expressed as a Fourier transform of the field after propagating the distance $z = f$ from the diffraction plane

$$\mathcal{E}(x, y, z) = \frac{je^{ikf}}{\lambda f} e^{-i\frac{\pi}{\lambda f}(x''^2+y''^2)} \mathcal{F}\left\{\mathcal{E}(x, y, z = f)\right\}(\nu_x, \nu_y). \tag{2.101}$$

With Eq. 2.98 and the application of the convolution theorem follows

$$\mathcal{E}(x, y, z) = \frac{je^{ikf}}{\lambda f} e^{-i\frac{\pi}{\lambda f}(x''^2+y''^2)} \mathcal{F}\left\{\mathcal{E}^T(x', y', z = 0) * h(x, y, z)\right\}(\nu_x, \nu_y) \tag{2.102}$$

$$= \frac{je^{ikf}}{\lambda f} e^{-i\frac{\pi}{\lambda f}(x''^2+y''^2)} \mathcal{F}\left\{\mathcal{E}^T(x', y', z = 0)\right\}(\nu_x, \nu_y) \cdot \mathcal{F}\left\{h(x, y, z)\right\}(\nu_x, \nu_y) \tag{2.103}$$

$$= \frac{je^{j2kf}}{\lambda f} \mathcal{F}\left\{E^T(x', y', z = 0)\right\}(\nu_x, \nu_y) \tag{2.104}$$

with $H(\nu_x, \nu_y) = \mathcal{F}\{h(x, y, z)\}(\nu_x, \nu_y) = e^{jkf} \cdot e^{-j\pi f\lambda(\nu_x^2+\nu_y^2)}$.

Equation 2.104 shows that a lens generates the spatial Fourier transform of the object in the image plane. Furthermore, two subsequent arrangements of 2-f lines, apply two Fourier transforms yielding the original field distribution as the Fourier transform is its own reverse operation.

If the diffracting object at $z = 0$ is a ruled grating with vertical lines, only the horizontal plane needs to be considered. The temporal Fourier transform of the field $\mathcal{E}(x, t)$ is $\tilde{\mathcal{E}}(x, \Omega)$ with $\Omega = \omega - \omega_0$ and the central frequency ω_0. As a plane wave is considered,

a separation into $\tilde{\mathcal{E}}(x,\Omega) = \tilde{\mathcal{E}}(\Omega)\mathcal{E}(x)$ is possible. Following [106], the field directly after the grating is

$$\mathcal{E}^T(x) = \sqrt{\beta}\mathcal{E}(\Omega)\mathcal{E}(\beta x)\exp(j\gamma\Omega x) \tag{2.105}$$

with $\beta = \cos(\vartheta_\mathrm{i})/\cos(\vartheta_\mathrm{o})$ and $\gamma = 2\pi/\left(\omega_0 g\cos\vartheta_\mathrm{o}\right)$. This means that the angular coordinate after the diffraction grating is translated into a spatial coordinate at the position $z = 2f$. This plane is called Fourier plane and allows to modify the spectral phase in the spatial domain.

In practice, the spatial coordinate has to be known as function of the frequency ω and an angle of incidence ϑ_i for a given setup. The transverse displacement $x(\lambda)$ of a given wavelength λ from the central wavelength λ_0 reads [107]

$$x(\lambda) = f\cdot\tan\left[\vartheta_\mathrm{o}(\lambda) - \vartheta_\mathrm{o}(\lambda_0)\right]. \tag{2.106}$$

Combining Eq. 2.106 with the grating relation from Eq. 2.83 leads to

$$x(\omega) - x_0 = f\cdot\tan\left[\arcsin\left(\frac{2\pi c}{\omega g} - \sin\vartheta_i\right) - \arcsin\left(\frac{2\pi c}{\omega_0 g} - \sin\vartheta_i\right)\right]. \tag{2.107}$$

Here, $x(\omega)$ is the horizontal coordinate in the Fourier plane and x_0 is the coordinate of the central frequency ω_0. Other literature [85] linearizes this term to achieve simpler expressions. As in this thesis, the correction of TOD plays a central role, approximations were not used here, since this would introduce new non-linearities. The output angle of a grating is not a linear function of the frequency and for a precise treatment no approximations are tolerable, here. The setup used for phase shifting is presented in Chapter 5.

2.6.3 Linear filters for spectro-temporal shaping

Linear filters are conceptually well known from signal theory [108]. The idea of describing and controlling a time-dependent effect in phase-frequency domain can be transferred to optical waveforms as well. The time-domain description of the output $\mathcal{E}_\mathrm{out}$ of a linear filter is characterized by the convolution of the impulse response function $h(t)$ and the input pulse $\mathcal{E}_\mathrm{in}(t)$

$$\mathcal{E}_\mathrm{out}(t) = \mathcal{E}_\mathrm{in}(t) * h(t) = \int \mathrm{d}t'\,\mathcal{E}_\mathrm{in}(t)h(t-t'). \tag{2.108}$$

Describing the same expression in frequency domain simplifies it a lot because the convolution theorem applies and reduces the equation to a multiplication which reads

$$\tilde{\mathcal{E}}_{\text{out}}(\omega) = \tilde{H}(\omega) \cdot \tilde{\mathcal{E}}_{\text{in}}(\omega). \tag{2.109}$$

The quantities used here are the Fourier transforms of the respective symbols from Eq. 2.108. The properties of the optical filter $\tilde{H}$ are described by the amplitude filter $R(\omega)$ and the phase filter $\Phi(\omega)$ in

$$\tilde{H}(\omega) = R(\omega) \exp(-j\Phi(\omega)) \tag{2.110}$$

Applying this to the incident light beam with a field $\tilde{\mathcal{E}}_{\text{in}} = |\tilde{\mathcal{E}}_{\text{in}}(\omega)| \exp(\mathrm{i}\Phi(\omega))$ leads to

$$\tilde{\mathcal{E}}_{\text{out}} = \underbrace{\left|\tilde{\mathcal{E}}_{\text{in}}(\omega)\right| R(\omega)}_{|\tilde{\mathcal{E}}_{\text{out}}(\omega)|} \exp\left[\mathrm{i} \underbrace{\left(\Phi_{\text{in}}(\omega) - \Phi(\omega)\right)}_{\Phi_{\text{out}}(\omega)}\right]. \tag{2.111}$$

Amplitude and phase of the resulting beam are $|\tilde{\mathcal{E}}_{\text{out}}(\omega)|$ and $\Phi_{\text{out}}(\omega)$, respectively. In frequency domain, the filter function $\tilde{H}(\omega)$ follows as

$$\tilde{H}(\omega) = \frac{\tilde{\mathcal{E}}_{\text{out}}(\omega)}{\tilde{\mathcal{E}}_{\text{in}}(\omega)} \tag{2.112}$$

if the incoming and outgoing fields are known. Any pulse-shaping setup modifying the spectral phase of the laser pulse can be described by linear filters. Table 2.1 gives an overview of the filter functions of simple pulse-shaping setups which are a Michelson interferometer, a grating compressor, a prism compressor, and a chirped mirror. The influence on spectral phase and amplitude for each setup is given in the third column.

2.7 Computer-controlled spatial modulation of light

The previous section covered the model behind the manipulation of optical pulses in the spectral domain. Setups known from classical optics (see Tab. 2.1) were described within that model. Studies of the analysis and synthesis of laser pulse trains using phase and amplitude filters already started in the 1980s [109]. After early approaches with phase shifting and/or intensity-absorbing optical layers, more modern attempts using computer-controlled optical elements were realized. Here, so-called liquid-crystal spatial light modulators (LC-SLMs), micro electro-mechanical systems

Table 2.1: Overview of simple pulse-shaping setups and their corresponding filter function in frequency domain.

instrument	phase shift in time domain	response in frequency domain
Michelson interferometer	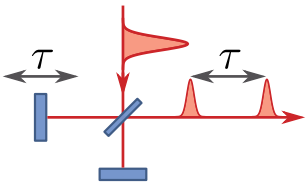	$\tilde{H}(\omega) = \frac{1}{2}(1 + e^{j\omega\tau})$
grating compressor/stretcher	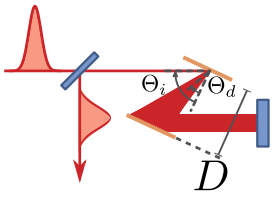	$\tilde{H}(\omega) = e^{j\phi(\omega)}$ $\phi(\omega) = \frac{2D\omega}{c} \cdot \frac{\cos(\Theta_i+\Theta_d)}{\cos\Theta_i}$
prism compressor/stretcher	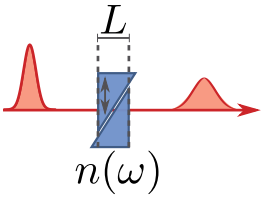	$\tilde{H}(\omega) = e^{j\phi(\omega)}$ $\phi(\omega) = n(\omega)L\omega/c$
chirped mirror	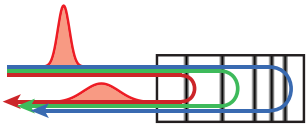	$\tilde{H}(\omega) = \lvert\tilde{H}(\omega)\rvert e^{j\phi(\omega)}$

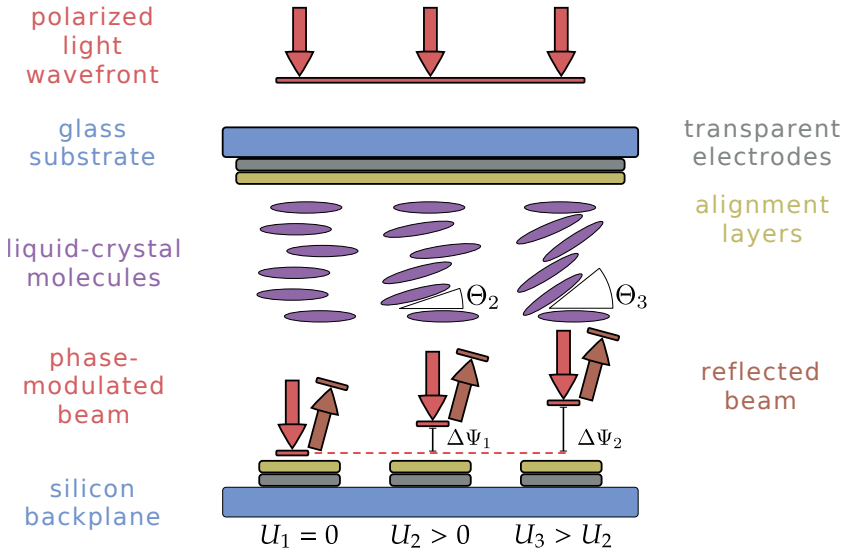

Figure 2.22: Principle of a pixelated, reflective laser phase shifter. After passing the entrance window, the incident plane wavefront is delayed depending on the orientation of the birefringent liquid-crystal molecules whose orientation is programmable through an external voltage. Each pixel allows an individual phase delay of the optical wavefront.

(MEMs) and acousto-optic modulators (AOMs) are still important today. Computer-controlled spatial modulators for manipulation of laser radiation are commercially available since the 1990s [110, 107].

In general, programmable optics features high flexibility and especially the ability to implement feedback loops which stabilize or control certain properties of the laser beam either spatially or temporally. Among the different devices, LC-SLMs feature refresh rates of several $10\,\mathrm{Hz}$ [111], while MEMs reach several $100\,\mathrm{Hz}$ [112] and AOMs can reach the $1\,\mathrm{MHz}$ range [113]. In this thesis, a liquid-crystal array was used to control the spectro-temporal shape of laser pulses by introducing a spatially-dependent phase shift. As was shown in Sec. 2.6.2, a grating followed by a lens can be used to perform an optical Fourier transform, introducing a correlation between spatial coordinate and wavelength of the laser pulse. Placing a phase-shifting LC-SLM in the Fourier plane allows to control the spectral phase and hence to shape the temporal profile of the pulse. Here, any arbitrary spectral phase shift can be programmed. The LC-SLM then performs as a computer-programmable phase filter with a response $H(\omega)$ and $|H(\omega)| \approx 1$ because the amplitude is not affected.

Figure 2.22 is a sketch of the principle of a liquid-crystal on silicon chip (LCoS) which is one technical realization of an LC-SLM. Typically, these devices form two-dimensional arrays of up to 1920×1080 pixels. For simplicity, the sketch shows a three-pixel phase

modulator containing voltage controllable liquid-crystal molecules which are aligned between transparent electrodes. A silicon backplane is used to electrically contact each pixel. A phase-only modulator uses liquid crystals in nematic phase because here a uniaxial alignment of the rod-shaped molecules is possible. Due to the birefringence of the crystals, a change of their orientation leads to a change of the effective refractive index along the axis of a traversing light beam. Hence, each pixel can delay the light wavefront individually.

The phase shift $\Delta\Phi$ as function of the control voltage U and resulting crystal angle Θ, crystal thickness d_{LC} and the refractive indices $n(\Theta(U), \lambda)$ and $n_0(\lambda) = n(\Theta(U = 0), \lambda)$ is

$$\Delta\Phi(U, \lambda) = \frac{2\pi d_{\mathrm{LC}}}{\lambda} \left(n(\Theta(U), \lambda) - n_0(\lambda)\right). \tag{2.113}$$

The analog control voltage is typically generated from a digital 8-bit signal and the electronics is very often based on controllers for video projectors. Hence, the input signal typically is a video signal based on DVI or HDMI standard. The prealignment of the crystals by the mask prevents a change of the beam polarization and allows for a real phase-only modulation. The experiments described in the following chapters were carried out using a reflective modulator. For high-power lasers, reflective modulators are preferred because the chip itself can be actively cooled and temperature-stabilized. However, transmissive modulators exist and often allow a simpler geometric arrangement of the optical setup.

The large number of pixels implemented in an LCoS SLM allows to reach output pulses with high complexity (see Eq. 2.71, Sec. 2.4.2). The theoretical upper limit of the complexity η is the number of illuminated pixels. However, practical limitations are caused by the finite laser beam diameter and the grating setup. If the LC-SLM is placed in the Fourier plane, the maximum achievable complexity η_{LC} reads [85]

$$\eta_{\mathrm{LC}} = \frac{\Delta\lambda}{\lambda} \frac{\pi}{\sqrt{\ln 2}} \frac{w_{\mathrm{in}}}{g \cdot \cos(\theta_{\mathrm{in}})} \tag{2.114}$$

with the relative bandwidth (FWHM) $\Delta\lambda/\lambda$, the input beam size w_{in}, the grating period g and the angle of incidence θ_{in}. Typically, a complexity of several hundreds is reached. It is directly proportional to the number of illuminated grating lines and defines the temporal range in which the pulse can be shaped.

In Chap. 5, the implementation of an LC-SLM-based laser pulse shaper is presented. It is used to generate THz pulses by means of a laser-electron interaction and results in precisely controllable spectro-temporal shaping capabilities in the THz regime [114, 115].

3 Generation of THz radiation at DELTA

The results presented in this thesis are based on experiments carried out at the synchrotron radiation source DELTA which is operated by the Center for Synchrotron Radiation at the TU Dortmund University in Dortmund, Germany. In this chapter, the accelerator and its short-pulse facility are described. The emission process of coherent THz radiation from a laser-electron interaction is explained and basic measurements are presented. Furthermore, the simulation developed and used in this thesis to model the coherent emission of THz radiation at the short-pulse facility is introduced.

3.1 The DELTA electron storage ring

DELTA, a 1.5-GeV electron storage ring, is a so-called second-generation synchrotron light source in user operation [116,117,118]. The users of DELTA carry out experiments with synchrotron radiation generated in the 1.5-T dipole magnets and from insertion devices such as undulators (U55 and U250) or the superconducting wiggler (SCW).

Figure 3.1 shows an overview of the accelerator complex. A thermionic triode gun with an anode voltage of $90\,\mathrm{kV}$ supplies electrons either in multi-bunch or single-bunch mode [119, 120]. Following, a velocity chirp along the electron beam is induced by a 3-GHz pre-buncher cavity. The subsequent drift space leads to a bunching of the electron beam. Afterwards, the electron bunching is strengthened in a 3-GHz buncher unit which also accelerates the electrons to an energy of $4\,\mathrm{MeV}$ and the 3-GHz linear accelerator (linac) increases the electron energy to $75\,\mathrm{MeV}$ [121]. Both, buncher and linac, are driven by a pulsed 3-GHz klystron.

In the booster synchrotron BoDo, which has a circumference of 50.4 m [122], the electrons are accelerated by a DESY-type three-cell 500-MHz cavity [123] which is supplied by a 20-kW solid-state amplifier. Electrons from the linac are injected to BoDo with a nominal energy of 75 MeV through the transfer line T1 and fast injection kickers. The ramping period of BoDo is $7\,\mathrm{s}$, during which the electron energy is increased to a final

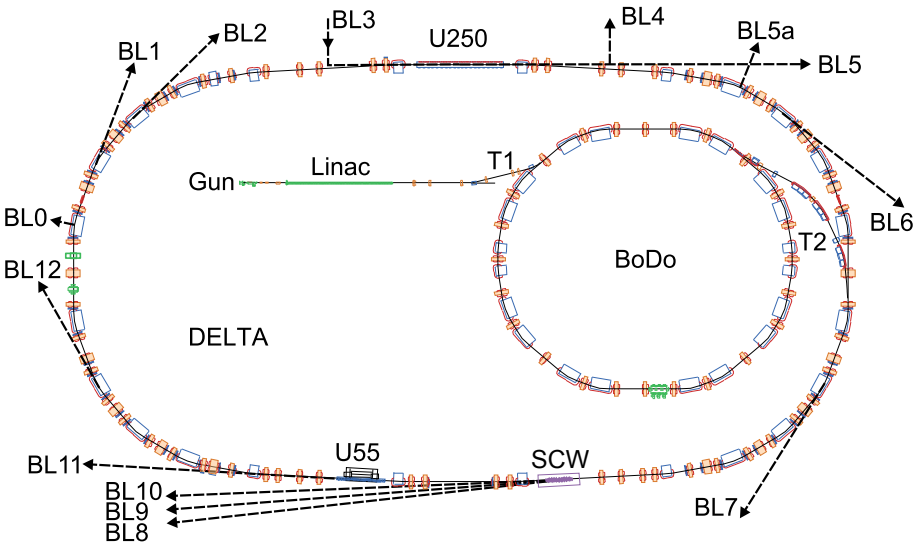

Figure 3.1: Overview of the synchrotron light source DELTA with the electron source (Gun), the linear accelerator (Linac), the booster synchrotron (BoDo) and the storage ring with its beamlines BL0 to BL12 (modified, courtesy of D. Schirmer).

value of $1.5\,\mathrm{GeV}$. The transfer line T2 and extraction/injection kickers are used to guide the beam to the storage ring. Since the operation mode of the gun can be changed online, a combined injection of single-bunch and multibunch, the so-called hybrid filling, is possible, as well.

The storage ring has a circumference of $115.2\,\mathrm{m}$ which results in a revolution period of $384\,\mathrm{ns}$ corresponding to a revolution frequency of $2.6\,\mathrm{MHz}$. The 500-MHz RF system of the storage ring uses a single-cell DORIS-type cavity and a European higher-order-mode damped (EU) cavity [124, 125]. The EU cavity is supplied by a 75-kW solid-state amplifier while a 65-kW klystron amplifier supplies the DORIS cavity [126]. Figure 3.2 shows a section of the synchrotron BoDo (left) and photographs of the cavities (center and right). During former storage-ring FEL experiments, DELTA has been operated at a reduced beam energy of $550\,\mathrm{MeV}$ [127]. Today, the standard beam energy is the maximum energy of $1.5\,\mathrm{GeV}$ for user experiments as well as for the operation of the short-pulse facility.

Since the cavities work at a frequency of $500\,\mathrm{MHz}$, the harmonic number, i. e. the number of possible bunches to be stored, is 192. However, in user operation only 144 bunches are filled. The maximum current in the standard mode is $130\,\mathrm{mA}$ but during the commissioning of the accelerator $300\,\mathrm{mA}$ beam current were reached [128]. Further parameters of DELTA are summarized in Tab. 3.1.

The short-pulse facility of DELTA relies on the interaction between an ultra-short laser pulse and a short slice of an electron bunch. For this interaction, a high-current sin-

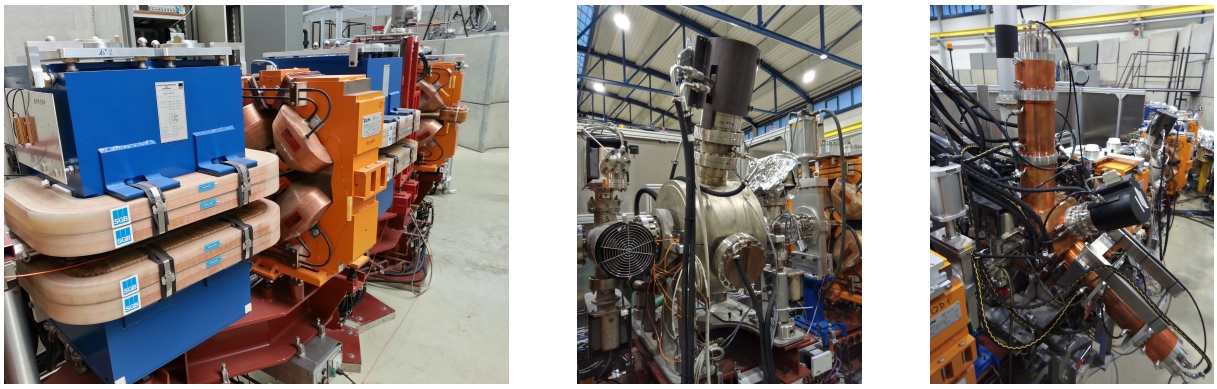

Figure 3.2: Left: Section of the Booster ring (BoDo) with bending magnets (blue) and quadrupole magnets (orange). Center: Single cell DORIS-type cavity installed in the storage ring. Right: European higher-order-mode damped (EU) cavity installed in the storage ring.

Table 3.1: Selected parameters of the electron storage ring DELTA.

nominal beam energy	1.49 GeV
circumference	115.2 m
revolution time	384.1 ns
revolution frequency	2.603 MHz
rf frequency	499.834 MHz
bunch spacing	2 ns
harmonic number	192
multibunch current	130 mA
multibunch lifetime	about 13 h (at 100 mA)
single-bunch current	3 to 20 mA
single-bunch lifetime	about 4 h (at 5 mA)
bunch length	about 100 ps (FWHM)
horizontal beam emittance	18 nm rad
vertical beam emittance	1.5 nm rad
momentum compaction factor	$4.8 \cdot 10^{-3}$
relative energy spread	$6.8 \cdot 10^{-4}$

gle bunch is filled with up to about $20\,\mathrm{mA}$. A short-pulse mode compatible with standard user operation is the hybrid filling pattern which is realized by injecting the single bunch within the 48-buckets gap of the multibunch setting. A typical beam lifetime is about 13 hours at a beam current of $100\,\mathrm{mA}$ in multibunch mode. Typically, the lifetime of a $20\,\mathrm{mA}$ single-bunch filling is only about 30 minutes. Hence, whenever possible, the short-pulse facility is operated with a single-bunch current of about $5\,\mathrm{mA}$ leading to a lifetime of about 4 hours. The beam current and lifetime measurement is based on a DC current transformer [129, 130].

To ensure a stable operation of the accelerator, the position of the beam is measured by 54 button-type BPMs and a computer-controlled, slow feedback [131] is used as an orbit correction which automatically adjusts the current of steerer magnets in order to reduce deviations from a predefined reference orbit. Recently, the feedback was exchanged and improved by moving away from a singular-value decomposition-based approach to a numerical optimization algorithm [132]. The accelerator and diagnostics components are controlled via EPICS [133], a popular control system for particle accelerators. The experimental setups developed in this thesis were integrated into EPICS, too, which features the possibility to acquire synchronous data from storage ring parameters as well as THz spectrometers (see Chap. 4), the autocorrelator for laser diagnostics (see Chap. 5), and the different pulse shaping setups (see also Chap. 5).

3.2 The short-pulse facility at DELTA

The electron bunch duration in the DELTA storage ring being about $100\,\mathrm{ps}$ (FWHM) predominantly defines the duration of the synchrotron radiation pulses emitted from bending magnets and insertion devices. Today, much shorter light pulses are emitted from lasers. However, their spectrum is near the visible range which is insufficient for many applications regarding the photon energy needed to drive certain processes. To provide ultrashort radiation pulses at much shorter wavelengths, a scheme employing a laser-electron interaction called coherent harmonic generation (CHG) was proposed in 1982 [134]. It was first implemented at ACO, Orsay, France in 1984 [135]. Experiments with CHG radiation were also carried out at the UVSOR-II storage ring in Okazaki, Japan [136]. A short-pulse facility using the CHG principle to generate ultrashort VUV pulses has been commissioned at DELTA in 2011 [137, 138, 26]. The scheme provides radiation pulses at harmonics of the laser wavelength using a laser-electron interaction inside the electromagnetic undulator U250 of the DELTA storage ring. Next to that, the interaction causes the coherent emission of (sub-)THz radiation in the subsequent bending magnets.

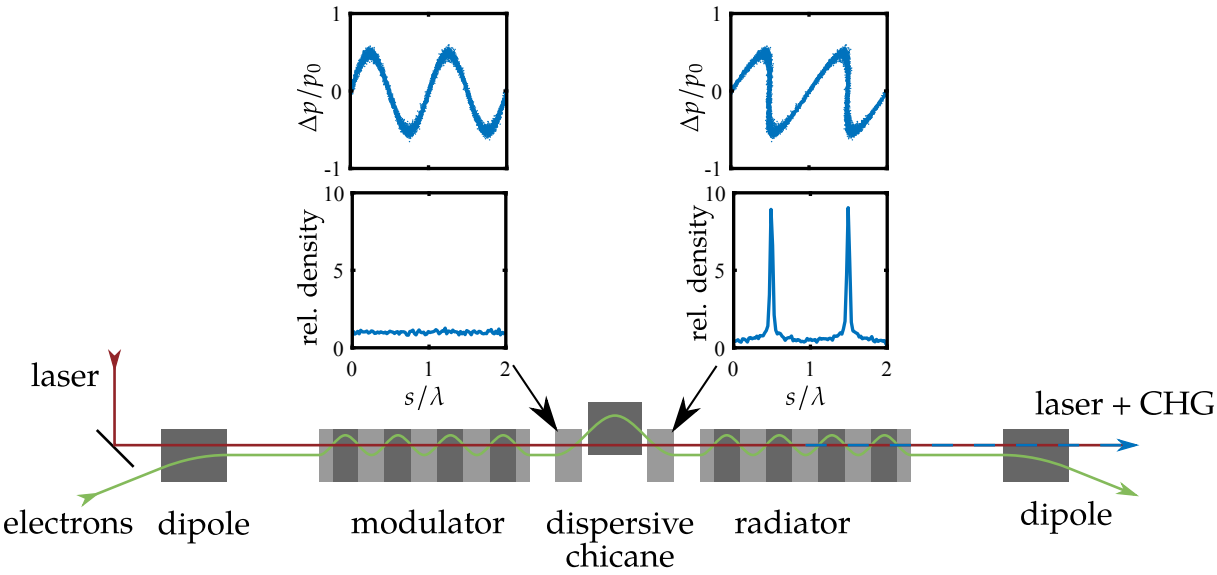

Figure 3.3: Sketch of the CHG setup. The incoming laser pulse (red) modulates the electron energy inside the first electromagnetic undulator (modulator). A dispersive chicane then transforms the energy modulation into a density modulation. The plots above the chicane show the energy distribution as function of the longitudinal coordinate before and after the chicane. The radiator is tuned to a harmonic of the laser wavelength. Hence, the short density spikes called microbunches give rise to coherent emission.

3.2.1 Setup

The CHG setup at DELTA employs the electromagnetic undulator U250 which was formerly part of the storage-ring FEL experiment [127] at DELTA. Ultrashort laser pulses with a pulse duration of approximately $50\,\mathrm{fs}$ (FWHM) copropagate with an electron bunch in the first part of the undulator called the modulator. The K-value of the modulator is tuned to the laser wavelength such that the resonance condition from Eq. 2.46, Chap. 2, is fulfilled. The horizontal oscillatory motion of the electrons leads to an interaction between the electrons and the transverse electric field of the laser pulse. The electrons gain or lose energy depending on their phase relative to the laser field. As shown in Fig. 3.3, a sinusoidal energy modulation is applied along a short slice in the bunch center. The modulator is followed by a magnetic chicane which introduces an energy-dependent path length. In the chicane, electrons with excess energy move ahead while electrons with less energy lag behind. Correct tuning of the matrix element r_{56} of the chicane causes a density modulation. Each falling slope of the energy modulation is converted to a density maximum called microbunch. After the chicane, another undulator called radiator is tuned to a harmonic of the laser wavelength. Here, the microbunches emit ultrashort pulses of coherent radiation at the radiator wavelength. The

Figure 3.4: Electromagnetic undulator U250 offers two different modes of operation: it can either be used as one long modulator or it is powered in a segmented way such that three regions are powered as modulator, chicane and radiator (see text for details).

intensity of the harmonics n being proportional to the square of the so-called bunching factor $b(n)$ scales as [139]

$$I_{\mathrm{CHG}} \propto b^2(n) \propto \exp\left(n^{-2}\right). \tag{3.1}$$

Reasonable intensities are achieved up to the fifth harmonic of the laser wavelength [140]. In 2022, an upgrade of the short-pulse facility towards the generation of short wavelength [140,141,142], the so-called SPEED (short-pulse emission via echo at DELTA) project was realized [143]. The echo-enabled harmonic generation (EEHG) scheme [144] uses a second modulator and a second chicane. A two-fold laser-electron interaction is used to generate a more complex density modulation with higher harmonic content which allows to reach even shorter wavelengths. In the case of EEHG the intensity scales as [145]

$$I_{\mathrm{EEHG}} \propto b^2(n) \propto n^{-1/3} \tag{3.2}$$

which allows to operate at even higher harmonics. At DELTA, all five magnet sections are implemented in the same undulator by individually powering groups of magnet coils.

Figure 3.4 shows a photograph of the undulator U250. Formerly, the undulator (250 mm period length, 19 periods) was operated in an optical klystron [146, 147] configuration as part of a storage-ring FEL setup. The coils of the undulator were powered in three groups – two undulators tuned to the same FEL wavelength and a central dispersive section inbetween. Nowadays, the short-pulse facility uses the first seven periods as

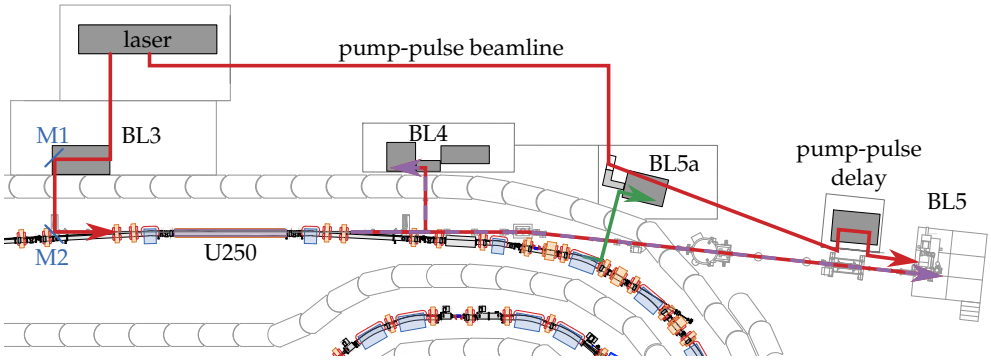

Figure 3.5: Short-pulse facility and laser laboratory at DELTA. The laser pulse is guided to the undulator U250 through BL3 using the motorized mirrors M1 and M2. The diagnostics BL4 and the VUV beamline BL5 allow to detect VUV radiation. To carry out pump-probe experiments at BL5 a portion of the laser pulse can be used for pumping a sample at BL5 (courtesy of T. Schulte-Eickhoff).

modulator, the central three periods as chicane and the final seven periods as radiator. The maximum resonance wavelength modulator and radiator can be tuned to is $840\,\mathrm{nm}$ which is slightly above the laser wavelength of $800\,\mathrm{nm}$ and thus offers a resonable tuning range. The chicance can be set to a maximum value of $r_{56} = 130\,\mu\mathrm{m}$ [148] at a current of $650\,\mathrm{A}$.

The laser operated at the short-pulse facility is a commercial system. It employs a Ti:sapphire short-pulse laser oscillator (Coherent Micra-5) synchronized to a sub-harmonic of the storage ring RF system. The laser pulses leaving the oscillator laser are amplified by a Coherent Legend Elite Duo HP chirped-pulse amplifier. More information about the laser system is given in Tab. 3.2 and Tab. 3.3.

To carry out CHG and THz experiments, spatial and temporal overlap of laser pulses and electrons in the U250 has to be achieved first. Figure 3.5 shows an overview of the short-pulse facility. Two remote-controllable, motorized mirrors M1 and M2 are used to guide the laser beam such that the laser pulses co-propagate with the electrons. The laser system, laser diagnostics and laser telescopes are operated in air, however M1 is the first in-vacuum mirror of the setup. Motorized in-vacuum screens, read out by cameras after M1 as well as M2, serve as laser-beam position indicators. The downstream direction of the U250 either points to the beamline 5 (BL5) or, if an in-vacuum $45°$ mirror is inserted, the beamline 4 (BL4).

Beamline 4 provides basic laser diagnostics such as cameras, photodiodes, a power meter and a streak camera to detect laser radiation and undulator radition. For the analysis of CHG radiation a grating monochromator (Czerny-Turner type [149]) is used. Next to that an additional in-vacuum XUV spectrograph covering the wavelength range from

Table 3.2: Parameters of the Ti:sapphire short-pulse laser oscillator.

model	Micra-5, Coherent Inc.
central wavelength	800 nm
bandwidth	100 nm
repetition rate	83.3 MHz
output power	400 mW
integrated pump laser	Nd:YVO_4, Verdi, Coherent Inc.
pump wavelength	532 nm
pump power	4.5 W (CW)
synchronization	6th sub-harmonic of the 500-MHz reference oscillator of the storage ring fed to a Synchrolock, Coherent Inc.

Table 3.3: Parameters of the Ti:sapphire laser amplifier.

model	Legend Elite Duo HP, Coherent Inc. chirped-pulse amplifier regenerative (multi-pass) + single-pass stage
central wavelength	800 nm
bandwidth	30 nm
pulse duration	40 fs
repetition rate	1 kHz (optional: 5 kHz)
output power	8 W
integrated pump laser	Nd:YLF, Evolution, Coherent Inc.
pump wavelength	527 nm
pump power	40 W (nominal)

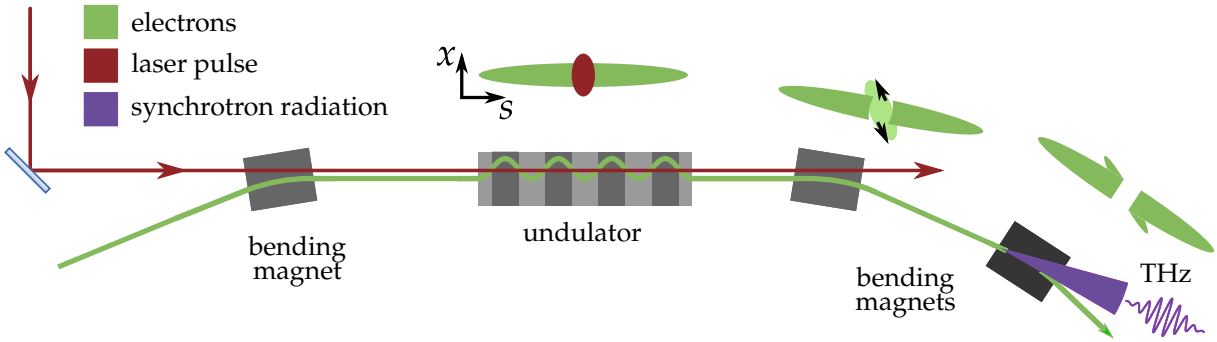

Figure 3.6: Sketch of the THz generation at DELTA (not to scale). The electron bunch (green) interacts with the laser pulse in the undulator acting as a modulator. During the passage of the subsequent dipole magnets, the modulated electrons leave the center of the bunch. The resulting gap gives rise to the coherent emission of THz radiation.

30 nm to 210 nm with a resolution better than 0.07 nm is currently under commissioning. A spectrometer for angle-resolving photoemission spectroscopy (ARPES) [150] in the XUV- and soft X-ray range is installed at the BL5. Pump-probe experiments with laser and CHG pulses can be carried out at this beamline [148].

3.2.2 Generation of THz radiation

A (sub-)ps structure in the longitudinal electron density $\rho(z)$ is required for giving rise to the coherent emission of THz radiation. At DELTA, the structures occur due to energy-dependent path length differences of the electrons modulated by the laser.

The change of the longitudinal position Δz of an electron with a relative energy deviation $\Delta E/E$ is

$$\Delta z = r_{51} x_0 + r_{52} x_0' + r_{56} \frac{\Delta p}{p_0}. \tag{3.3}$$

Here the matrix elements r_{51}, r_{52} and r_{56} belong to a combined transfer matrix which considers all magnetic fields between the energy modulation and the source point. The most relevant effect in the longitudinal movement depends on the combined r_{56} which contributes proportionally to the energy deviation. Due to this effect, which is illustrated in Fig. 3.7, an electron with positive energy deviation will lag behind while an electron with negative energy deviation will move ahead. This leads to a depopulation of the central bunch section and to the formation of two maxima in the longitudinal electron density about the center.

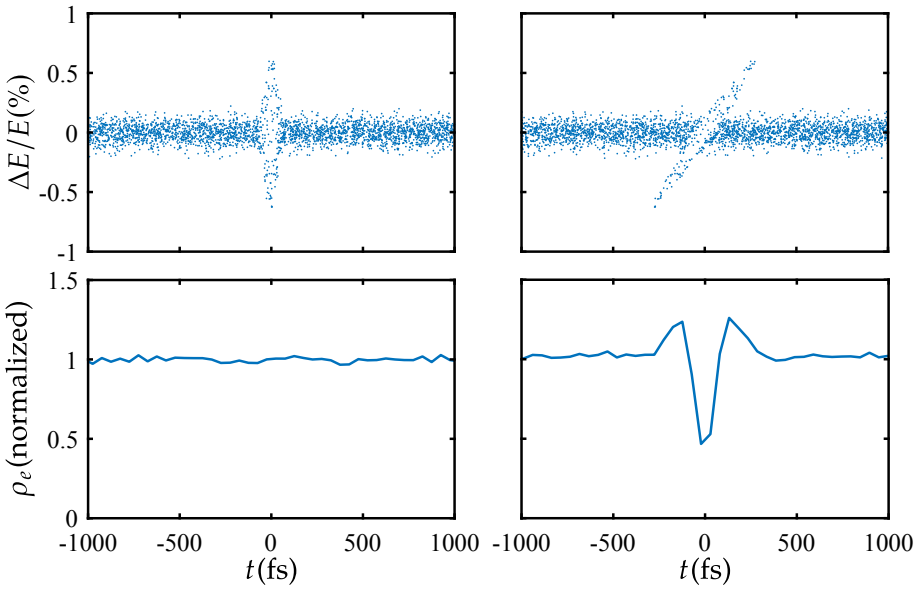

Figure 3.7: Simulated evolution of the relative energy deviation $\Delta E/E$ after a laser-electron interaction and the longitudinal electron density as function of the arrival time t. The central part of the electron bunch is modulated by a 50-fs laser pulse (top left). First, the electron density is unaffected and uniformly distributed. After passing the subsequent magnet structure, the distribution of the energy deviation (top right) is sheared which leads to a dip in the longitudinal electron density which is surrounded by two maxima (bottom right).

3.2.3 The THz beamline at DELTA

As part of the commissioning of the short-pulse facility at DELTA in 2011, the dedicated THz beamline (BL5a) was designed and put into operation [137, 138].

The outlet chamber houses a gold-coated copper mirror which is water cooled. It reflects UV light and longer wavelengths to the first focusing mirror. Shortly after that mirror, the vacuum system of the actual THz beamline begins with a window. While originally built with a z-cut quartz window, the beamline was equipped with a $0.85\,\mathrm{mm}$ thick diamond window in 2017. The window is soldered in a CF100-CF63 reducer flange and features a clear aperture of $50\,\mathrm{mm}$. It can withstand a maximum pressure of $1\,\mathrm{bar}$ from both sides [151]. The beamline uses a 100-mm tubing featuring a 10-mm layer of aluminium foam to avoid wall reflections. The large surface of the aluminium foam limits the vacuum pressure in the THz beamline to a minimum of about $10^{-6}\,\mathrm{mbar}$. A total number of six focusing mirrors is used to guide the beam above the radiation protection shielding and down to an optical table in the BL5a laboratory. The six mirrors form three sets of so-called Gaussian telescopes. A Gaussian telescope consists of two mirrors located at a distance being equal to the sum of their focal lengths. This arrangement features a beam waist position which is independent of the wavelength. Hence, the three sets of telescopes guarantee a fixed position of the final beamline focus. To maintain a stable ambient temperature with a stability of $\pm 1\,^{\circ}\mathrm{C}$, the laboratory is an air-conditioned hutch.

3.3 Measurements of coherently emitted THz pulses

To analyze THz radiation at DELTA, two main beam paths exist. One beam path reaches a commercial in-vacuum spectrometer which allows to measure THz spectra free of water-absorption by air-humidity. The other beam path is realized in air. Through two possible z-cut quartz windows, the beam can leave the vacuum system. To prevent water absorption at a still reasonable level, this beam path can also be covered and flooded with nitrogen. In air, detectors such as the YBCO detector, the Schottky diode or a silicon bolometer are used to measure the temporal intensity of THz pulses.

Figure 3.8 shows a direct comparison of the response of the YBCO detector and a Schottky diode. Here, the THz beam was split using a polarizing wire grid to achieve equal intensity at both detector inputs. It is noticeable that the blue curve shows an additional first peak next to the red curve, which seems to have a delayed detection. However, both detectors measure a train of THz pulses from consecutive storage ring revolutions. The

major difference between the two detectors is their spectral sensitivity. The YBCO detector is sensitive upto $2.5\,\mathrm{THz}$ while the sensitivity of the Schottky detector drops above $1\,\mathrm{THz}$.

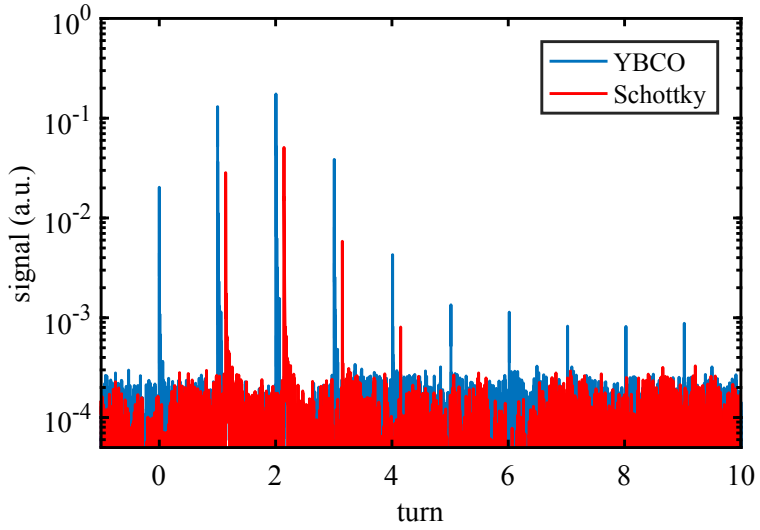

Figure 3.8: Measurement of THz pulses after the initial laser-electron interaction with two different detectors: The YBCO detector (blue) senses higher frequencies than the Schottky diode (red). However, the YBCO detector offers a higher sensitivity allowing to resolve late pulses easier. The red curve was shifted by $30\,\mathrm{ns}$ to achieve a better visibility.

The different detector responses to the individual THz pulses from consecutive revolutions already hint at different spectral compositions of the pulses. To study the spectro-temporal evolution, simulations and time-resolved spectral measurements were performed.

3.4 Simulations of the radiation emission

For theoretical studies of the generation of THz radiation at DELTA, a new C++-based [152] simulation code was developed. Although similar software existed (for example THzSMe [153]), a significant speedup was achieved and further pulse shaping methods were implemented. A shortening of the computation time was needed because the studies presented in Chap. 6 required simulations of the longitudinal phase space during 500 storage-ring revolutions with high spatial and temporal resolution. Another requirement to the software was a flexible changing of the laser pulse parameters, especially pulse duration, pulse shape, spectral phase and spectral intensity.

Three main steps are executed by the simulation:

1. Definition of the laser pulse shape according to the laser pulse properties and a given pulse shaping setup. A Gaussian pulse, a periodic modulation with given chirp parameters up to third order or a user-defined laser phase modulation by a spatial light modulator (see Chap. 5) can be selected.
2. Modeling of the laser-electron interaction in the undulator U250.
3. Six-dimensional tracking of two sets of electrons in the storage ring according to a given lattice configuration. One electron ensemble holds an energy modulation while the other one maintains unmodulated. This step is performed by the well established software `elegant`[1] [154].
4. Analysis of the longitudinal electron configuration to calculate the coherent emission in the THz regime.

The energy modulation calculated in step 2 is modeled as an integration over discrete time steps. The electric field of the laser pulse and the electron position are evaluated after each time step to calculate the energy exchange. The laser pulse is modeled including offsets in spatial, angular and temporal coordinates and user-defined spectral phase and amplitude. To model the laser pulses as realistically as possible, one of the predefined pulse shaping settings implements the pulse compression as a Treacy-type compressor (see Chap. 2). The spectral phase of the laser is then calculated according to Eq. 2.86 and Eq. 2.87, Chap. 2. Further settings are laser double pulses, and laser pulses with periodic intensity modulation and variable third-order dispersion. Storing the six-dimensional coordinates of the electrons is organized in a shared memory [155] which is physically realized by direct access to the computer RAM[2], allowing to efficiently share fast access to the data from different parts of the software and also from external tools such as the third-party tracking tool `elegant` [154]. The `elegant` code is used for the tracking of the two electron bunches generated before. It models the effect of the magnetic fields as a sequence of small discrete kicks, which allows to resemble the statistical emission of synchrotron radiation photons and the corresponding energy loss in a realistic way. The electrons of modulated and unmodulated bunch are tracked for a user-defined number of revolutions, beginning after the modulator.

The longitudinal electron density is calculated from the electron coordinates at the position of the THz beamline. To observe the effect of the laser modulation, the densities of modulated and unmodulated bunch are substracted. Afterwards the form factor (see Chap. 2) is determined by a Fourier transformation of the density difference. Further output generated by the simulation is the evolution of the longitudinal phase space.

[1] ELEctron Generation ANd Tracking
[2] Random Access Memory

Table 3.4: Simulation output of coherent emission of THz radiation based on a laser-electron interaction tracked through five revolutions in the storage ring.

turn	central frequency	bandwidth
0	3.45 THz	2.5 THz
1	0.15 THz	0.15 THz
3	0.09 THz	0.08 THz
4	0.07 THz	0.05 THz
5	0.07 THz	0.04 THz

3.4.1 Simulation of broadband emission

The persistance of the coherent THz emission for several storage ring revolutions was shown in Fig. 3.8. Running the simulation code presented in the previous section allows to simulate the evolution of the longitudinal electron density over several turns. The coherent emission of THz radiation can be analyzed on a turn-by-turn base.

Figure 3.9 shows the simulated emission spectra of five consecutive revolutions in the storage ring. The turn-0 data belong to the emission just after the laser-electron interaction. The central emission frequency lies at 3.45 THz and the bandwidth is 2.5 THz. During the following revolutions the density structure broadens further, leading to lower emission frequencies. The simulation results of the first five revolutions are given in Tab. 3.4. Except for the turn-0 simulation, the relative bandwidth is close to 100 % which emphasizes the broadband character of the source. Further simulations and measurements of laser-induced THz radiation using laser pulses with periodic modulation are presented in Chap. 5. The simulation code is used again in Chap. 6 to describe the long-term evolution of THz spectra on the timescale of the synchrotron oscillation period.

To acquire THz spectra at DELTA, the commercial spectrometer (Bruker Vertex 80V, see App. A.6) covering the frequency range from 1.2 THz to 240 THz was commissioned in 2013 [156]. The device is connected to the vacuum system of the THz beamline and allows to measure the transmission of samples in vacuum. However, the detector and readout chain are not suited well to observe the temporal evolution of THz spectra on a turn-by-turn basis. To realize this, a new spectrometer optimized for the operation from the few 10 GHz regime to several THz was designed in a master's thesis [157]. The commissioning process of this spectrometer was carried out in the context of this thesis. A description of the spectrometer and results from spectral measurements are presented in the next chapter.

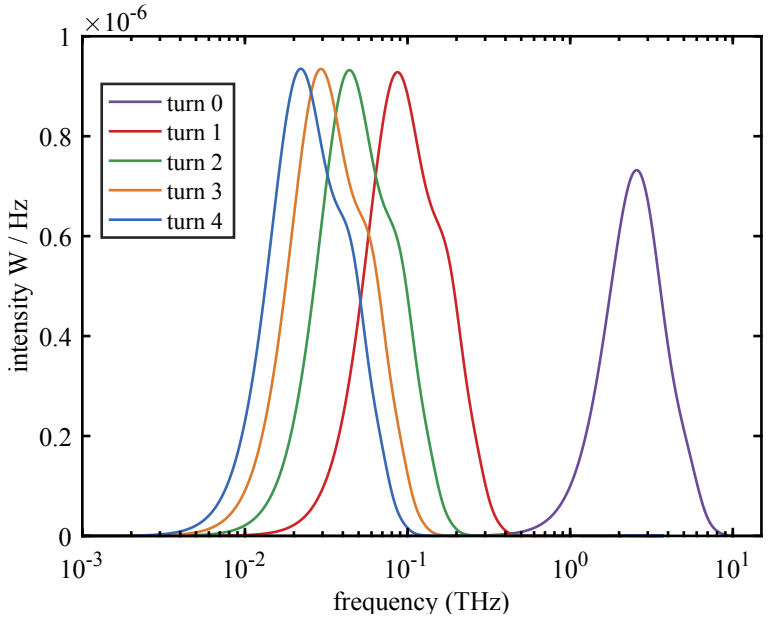

Figure 3.9: Spectral simulation of five consecutive (sub-)THz pulses. From the simulated longitudinal electron density, the coherent emission spectrum is calculated. During the first five revolutions, a continuous shift from a spectrum being centered around 3.45 THz towards 70 GHz is observed.

3.5 Further techniqes

The generation of THz radiation based on a laser-electron interaction is the main topic of this thesis. However, further methods can be used to generate pulses in the THz regime. The generation of THz radiation based on the microwave instability is another accelerator-based technique and its observation at DELTA is described in the following section. Another method which is based on the excitation of a photo-conductive antenna is used at DELTA to test THz setups without accelerator-based radiation. More details on this technique can be found in another thesis [158].

3.5.1 Emission of THz radiation based on the microwave instability

Synchrotron radiation at wavelengths which are longer than the charge distribution causing the radiation phenomenon, is generally emitted coherently as the radiation emitted from different parts of the bunch is in phase by definition. In this case, the spectral power of the coherent radiation is proportional to the number of electrons squared. A mechanism leading to the emission of THz radiation is the coherent synchrotron radiation (CSR) impedance which leads to a modulation of the longitudinal phase space

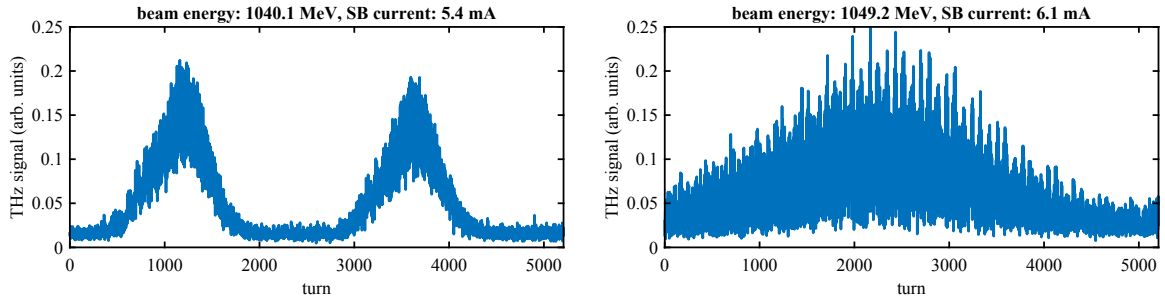

Figure 3.10: Measurement of the THz intensity over 5000 turns. Depending on the beam current and the beam energy, the repetition frequency of the THz pulse trains varies. At lower beam current (left) sporadic THz emission is observed while at higher beam current, THz pulses are emitted during each revolution with varying peak intensity.

giving rise to the formation of substructures in the longitudinal electron density which then emit CSR.

The so-called parallel-plates model [159] describes the influence of a conductive vacuum chamber of height $2h$ on an electron bunch. Here, the interaction of vacuum chamber and electron bunch leads to an impedance causing the radiation phenomenon. The radiation emission occurs above a threshold beam current

$$I_{\mathrm{b}}^{\mathrm{th}} = \gamma I_A \sigma_\delta^2 \alpha_c R^{-1/3} \sigma_{z,0}^{1/3} \left(0.5 + 0.12 R^{1/2} \sigma_{z,0} h^{-3/2}\right) \tag{3.4}$$

with the Lorentz factor γ, the Alfvén current I_A, the relative energy spread σ_δ, the momentum compaction factor α_c, the bending radius R and the natural bunch length $\sigma_{z,0}$. During standard operation of DELTA, either multibunch or single bunch, it is not possible to observe THz emission from coherent synchrotron radiation. However, Eq. 3.4 depends on the Lorentz factor and hence on the beam energy which means that during low-energy operation, the emission of THz bursts is more likely. The DELTA storage ring can be run at various energies between about $500\,\mathrm{MeV}$ and $1500\,\mathrm{MeV}$ [160]. A measurement of the threshold current for coherent THz bursts was performed during an energy ramp with a high single-bunch current of $10\,\mathrm{mA}$ starting at the standard energy of $1500\,\mathrm{MeV}$. A Schottky-barrier detector at the THz beamline read out by a fast and large-memory oscilloscope was used to acquire the THz intensity. Figure 3.10 shows examples of THz emission depending on the energy and the beam current.

Figure 3.11a shows the Fourier transform of the THz bursts as function of the beam current which is also known as a burst spectrogram (see e.g. [161]). The spectrogram is acquired at a beam energy of $1\,\mathrm{GeV}$. Broadband bursting occurs above a beam-current threshold of $4.7\,\mathrm{mA}$. However, the spectrogram shows spikes at harmonics of $22.8\,\mathrm{kHz}$,

which is the synchrotron oscillation frequency. Here, the bursting starts already at a current of $4.2\,\mathrm{mA}$ due to resonance effects.

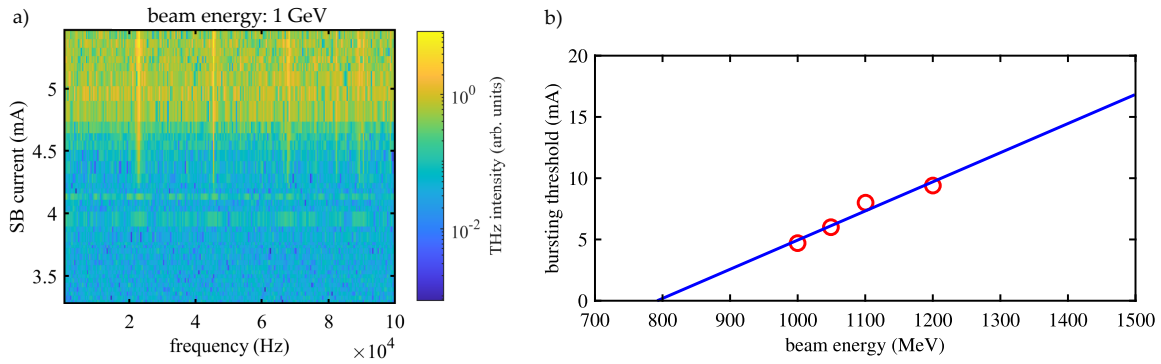

Figure 3.11: a) Frequency spectrum of the THz emission as function of the beam current. b) Threshold currents at which THz bursting occurs as function of the beam energy.

The measured bursting threshold current as function of the beam energy is linear (Fig. 3.11b). Extrapolation of the linear relation shows that in standard user operation the bunch current would need to be about $17\,\mathrm{mA}$ to overcome the bursting threshold. The actual bunch current at a total beam current of $130\,\mathrm{mA}$ is $0.9\,\mathrm{mA}$ if 144 out of 192 buckets are filled which is explains why THz bursts where not observed at a beam energy of $1.5\,\mathrm{GeV}$ so far.

The THz bursts offer an additional radiation source in the sub-millimeter wavelength range at DELTA. In comparison to the THz emission based on the laser-electron interaction, the frequency range is limited to a few $100\,\mathrm{GHz}$ but the revolution frequency being $2.6\,\mathrm{MHz}$ is much higher than laser-initiated emission.

Further studies of THz bursts and the control of the microbunching instability were done at other facilities as, for example, KARA [161], SOLEIL [162], the Metrology Light Source [163] and BESSY II [164].

4 Fourier-transform spectrometry at the DELTA THz beamline

Time-domain measurements of THz signals generated at DELTA were presented in Chapter 3. As the emission process is based on the laser-electron interaction, the duty cycle of the resulting oscilloscope trace is low: a pulse lasting several picoseconds is detected every millisecond. Consequently, analyzing time-domain data with RF-based detectors is inherently challenging. Resolving the pulses requires ultra-high data acquisition bandwidth in the GHz range and a low-jitter trigger. Therefore, a more flexible diagnostic approach involves using a fast spectrometer to provide turn-resolved spectra.

The analysis of spectral amplitude and phase information is particularly important to understand ways to manipulate the pulse shape of electromagnetic radiation pulses, be it laser pulses or THz radiation pulses. The approach of modelling the (quasi-)optical frequency response of instruments, i.e. phase shift and absorption, was introduced in Chapter 2. Examples of response functions of simple optical systems were given in Tab. 2.1. To keep a common description of different experimental systems throughout this thesis, the diagnostics is described by its frequency response function, too.

A spectrometer for the (sub-) THz range was designed in a master's thesis [157]. Optimizations and commissioning were done within the scope of this thesis. Simulation results presented in the previous chapter showed a turn-by-turn evolution of the THz spectrum, moving from central frequencies of several THz to $10\,\mathrm{GHz}$ after a few revolutions in the storage ring.

In the design process of the spectrometer particular importance was given to the feature of resolving spectral information turn-by-turn after the initial laser-electron interaction. However, resolving single-shot THz spectra with sufficient resolution would be challenging [165]. The compromise chosen here is to use sufficiently fast detectors providing readout rates much faster than a revolution period. The data are averaged over many laser shots but averaged data for individual turns after the laser-electron in-

teraction are still available. The setup of the spectrometer is discussed in the following sections.

4.1 Spectrometry in the THz domain

In the field of THz diagnostics, a Fourier-transform spectrometer consisting of an interferometer being readout as function of the interferometer delay, offers several advantages over diffractive spectrometers using prisms or gratings. Finding highly efficient prisms or gratings for a wide frequency range can be difficult and costly and any dispersive spectrometer has the disadvantage that the intensity needs to be high enough such that the dispersed beam is still detectable. Because of its wide use in infrared spectroscopy interferometer-based spectrometers are often also referred to as Fourier-transform infrared (FTIR) spectrometer. Detailed information on theory and use of Fourier-transform spectrometers can be found in [166].

Figure 4.1 depicts the basic setup of a Fourier-transform spectrometer based on a Michelson interferometer. The interferometer uses a beam-splitter to separate the beam into two orthogonal arms, the adjustable arm and the reference arm.

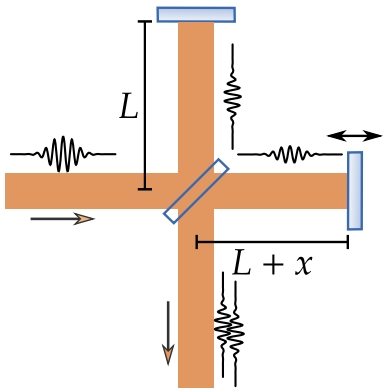

Figure 4.1: Basic principle of an FTIR spectrometer. A Michelson interferometer is used to split the beam and recombine it with a delay. The recombined radiation intensity is recorded as a function of the delay. (See text for details).

The idea is to record the intensity at the output as function of the optical path difference $\delta = 2x$ of the two arms. Generally, the Fourier transform of the incoming signal describes the electric field of an incoming pulse as a weighted sum of monochromatic waves. The electric field of the incoming pulse in time domain reads

$$\mathcal{E}_{\text{in}}(t) = \int \tilde{\mathcal{E}}(\omega)\, \mathrm{e}^{j\omega t} \mathrm{d}\omega\,. \tag{4.1}$$

After recombination, the electric field $\mathcal{E}_{\text{out}}$ is the sum of the two split beams of the original field, one of which is shifted by a frequency dependent phase advance $\varphi(\omega) = \omega/c \cdot 2x$. The recombined field is then written as

$$\mathcal{E}_{\text{out}}(t) = \frac{1}{2}\int \tilde{\mathcal{E}}_0(\omega)\,\mathrm{e}^{j\omega t}\mathrm{d}\omega + \frac{1}{2}\int \tilde{\mathcal{E}}_0(\omega)\,\mathrm{e}^{j\left[\omega t - 2\phi(\omega)x\right]}\,\mathrm{d}\omega\,. \tag{4.2}$$

The intensity measured during the acquisition of the interferogram $I(x) \propto \left|\tilde{\mathcal{E}}_{\text{out}}(t,x)\right|^2$ is given by

$$I_{\text{out}}(x) = \frac{1}{2}\int \tilde{I}_0(\omega)\left\{1 + \cos\left[\varphi(\omega)\right]\right\}\mathrm{d}\omega \tag{4.3}$$

$$= \frac{1}{2}I_{\text{tot}} + \frac{1}{2}\int \tilde{I}_0(\omega)\cos\left[\varphi(\omega)\right]\,\mathrm{d}\omega \tag{4.4}$$

with the spectrally integrated intensity I_{tot}. The second term of Eq. 4.4 contains the spectral information while the first term is an unmodulated, constant contribution which can be neglected for the spectral analysis of the signal. Typically, the interferogram $I(x)$ is defined as

$$I(x) = \int B(\omega)\cos(\varphi\,[\omega)]\,\mathrm{d}\omega. \tag{4.5}$$

For any broadband signal, (partial) destructive interference occurs depending on the delay x, except for the case of $x = 0$. A typical interferogram is symmetric ($I_{\text{out}}(x) = I_{\text{out}}(-x)$) and has a strong central peak ($I_{\text{out}}(x = 0) = I_{\text{tot}}$). Fourier transforming the interferogram gives the spectrum

$$B(\omega) = \int I(x)\cos\left[\varphi(\omega)\right]\mathrm{d}\omega\,. \tag{4.6}$$

The interferogram is an even function of x. The Fourier transform then reduces to the Fourier cosine transform because the sine transform is always zero.

4.2 Distortions and resolution

Spectral imperfections such as non-constant reflectivity or transmission of the beam splitter can be taken into account by defining a spectral correction $H(\omega)$ with

$$B(\omega) = \frac{1}{2}H(\omega)\,\tilde{I}_0(\omega)\,. \tag{4.7}$$

In order to let Eq. 4.6 converge to the spectrum, the integration must be performed over infinite delays. Since, in reality, the delay is limited by the mechanics of the interferometer, the spectrum becomes a convolution of the interferogram and a boxcar function $f(x) = 1$ for $x \in [-x_{\max}, x_{\max}]$ and $f(x) = 0$ elsewhere, which reads

$$G(\omega) = \int f(x)I(x)\cos\left[\varphi(\omega)\right] \mathrm{d}x = \tilde{f}(\omega) * B(\omega) \tag{4.8}$$

$$\text{with} \quad \tilde{f}(\omega) = 2x_{\max}\,\mathrm{sinc}\left[\varphi(\omega, x_{\max})\right] . \tag{4.9}$$

The sinc function being defined as $\mathrm{sinc}(x) = \sin(\pi x)/(\pi x)$ has a width (FWHM) of

$$\Delta\omega \approx 1.896\,\frac{c}{x_{\max}} \tag{4.10}$$

which means that the resolution is inversely proportional to the maximum delay $x_{\max}$ and hence a monochromatic spectrum $B(\omega) = \delta(\omega - \omega_0)$ will appear spectrally broadened as given by Eq. 4.10.

The limited scanning range of an FTIR spectrometer can cause a ringing-effect which is relevant specially for low-frequency radiation with central frequency close to the resolution limit. Resolving these spectral features requires maximum optical delay and stopping the acquisition of the interferogram at a position with non-zero intensity introduces a ripple caused by Eq. 4.9. To avoid this effect, a long enough travel was realized in the spectrometer commissioned in this thesis.

The maximum-resolvable frequency is given by the Nyquist-Shannon theorem which states that the phase advance between two sampling points must be smaller than π. The interferogram $I(x)$ is sampled as function of the optical delay x. The digitization is performed at discrete mirror positions. Since the fast Fourier transform (FFT) algorithm needs equidistantly spaced data points, the data are first interpolated to a common spacing Δx. The maximum detectable frequency is then given by

$$\omega_{\max} = \frac{\pi c}{\Delta x} . \tag{4.11}$$

One major advantage of FTIR spectrometers over diffractive or dispersive spectrometers are contrast and sensitivity of the measurement. The electric fields of all frequencies contained in the signal reach the detector simultaneously which leads to a better signal-to-noise ratio and can be used to reduce the acquisition time. Spatially splitting the signal, as done in a diffractive setup, is not necessary. Furthermore, diffractive spectrometers typically need an entrance and an exit slit/aperture to improve the spectral

resolution at cost of intensity. Beam waists in the THz range tend to be rather large (cm scale) and hence it is beneficial to avoid intensity-blocking apertures.

4.3 Short-pulse paradox in view of linear filters

The spectral diagnostics of a pulsed radiation source with a Michelson interferometer easily leads to confusion. If the pulse separation in the interferometer is wider than the pulse duration, it is unintuitive why an interference effect is still observable. The reason is, of course, that an interferometer is sensitive to the temporal coherence and not the pulse duration. The general concept of a pulse being a rapid, transient amplitude only works for the description of a signal in time domain. However, a base change from time domain to frequency domain must be possible, without loosing information.

A Fourier-transform spectrometer always acts as a narrowband filter in frequency domain. Here, the filter function depends on the interferometer position. As discussed in Chapter 2, any frequency dependent filter applied to a few-cycle, Fourier transform limited, broadband pulse will increase the pulse duration due to the bandwidth limitation. The filter bandwidth of a Michelson interferometer can be derived from Eq. 4.3. The transmission neglecting the phase for a fixed delay x reads

$$T = \frac{1}{2}\left(1 + \cos\left[\frac{2\pi x}{c} \cdot f\right)\right] \tag{4.12}$$

which is the real part of the complex response function given in Tab. 2.1 being

$$H = \frac{1}{2}\left(1 + \exp\left[\frac{2\pi j x}{c} \cdot f\right)\right]. \tag{4.13}$$

Equation 4.12 resembles the suppression of certain frequencies due to destructive interference. It is the real part of Eq. 4.13 which means that the complex phase is neglected. The difference between a fast, phase-sensitive detector and a slow, phase-insensitive detector is that the latter does not resolve any influence of the imaginary part of $H(\omega)$ which reduces the response to T. Only measuring a signal being proportional to the square of the amplitude, i. e. the intensity, leads to loosing the phase information.

Broadband THz pulses generated at DELTA are close to single-cycle pulses which are Fourier-transform limited inherently. The filter function Eq. 4.12 has a (smoothed) comb-like transmission with a comb period of c/x. For better illustration a 1-ps pulse with a central frequency of $1\,\mathrm{THz}$ is assumed. The convolution of the spectral transmission of the filter with the transform limited pulse is calculated and the resulting filtered

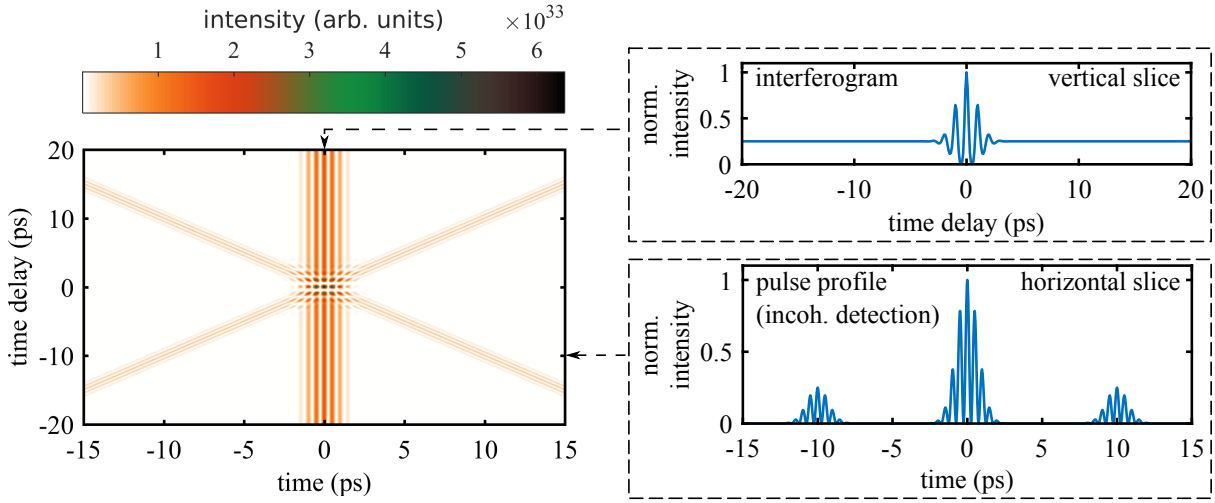

Figure 4.2: Left: Temporal distribution (horizontal axis) of the electric field of a bandwidth-limited THz pulse in an interferometer as function of the interferometer delay (vertical axis) without phase information. The central vertical line is the interferogram (see also top right). Neglecting the phase removes any information which of the two pulses arrives earlier. Nevertheless, the interferogram is reconstructed without this information.

pulse is plotted in Fig. 4.2 (left). For each time delay, the input pulse experiences a different real filter function which neglects the phase information.

In Fig. 4.3 the response of a phase-sensitive detector is plotted. The arrival order of the two pulses can be derived unambigously. However, the interferograms of the direct and the indirect detector are equal which shows that it is not needed to resolve the separation of the pulses.

4.4 Preprocessing of the interferograms

In theory, a Fourier-transform spectrometer derives the spectral amplitude from the integral of the interferogram over an infinite delay interval. In reality, the path length difference is limited by the delay line of the interferometer. The Fourier transform is calculated using the fast-Fourier transform (FFT) algorithm which requires the number of sampling points to be a power of 2. The delay line should be long enough such that the detector signal with maximum delay has approximately declined by half the maximum intensity ($I_0/2$). This value is substracted from the interferogram before calculating the Fourier transform and the data are extended by zeros to reach the correct amount of datapoints to perform an FFT. It can be shown mathematically that this so-

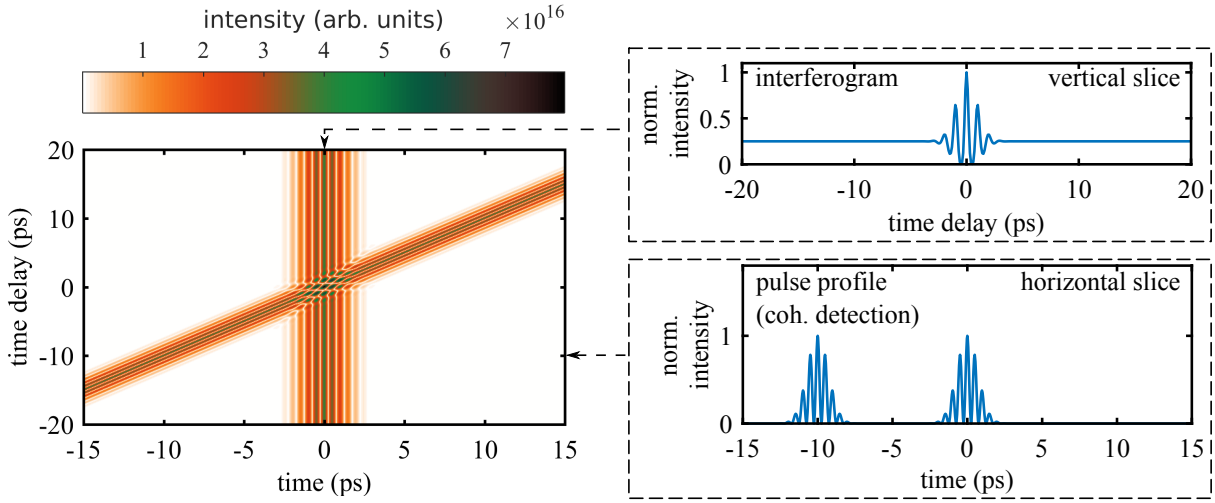

Figure 4.3: Schematic of an incoherent, phase-insensitive readout of a Michelson interferometer used to diagnose short pulses (1 ps (rms))

called zero-padding technique in spatial domain, corresponds to an interpolation in frequency domain without altering the signal [167].

4.5 Setup

Typically, Michelson interferometers use dielectric beamsplitters. In the THz regime, many materials have absorption resonances and specially lower frequencies are not efficiently reflected. This problem is solved by using polarization-based beam splitters. A sketch of the interferometer commissioned in this thesis is shown in Fig. 4.4. Wire-grid polarizers made from free-standing, thin wires offer close to fully symmetric reflection/transmission ratios if the incident beam is linearly polarized and the wires are rotated by 45 degree with respect to the electric field. Equipping a standard Michelson interferometer with such a kind of polarizer is not sufficent for interferometry because the portion of light being transmitted at the polarizer will be fully transmitted again after passing a mirror. Instead, the polarization is rotated by 90° by using a roof-top shaped mirror.

4.6 Spectra of coherently emitted THz radiation

In 2012, a commercial FTIR spectrometer with a sensitive range from 1.3 THz to 240 THz and a resolution better than 1.8 GHz was installed at the THz beamline. The lower fre-

quency limit is set by the beamsplitter made of a thin Polyethylene terephthalate[1] sheet consisting of 50-µm thick layers. The transmission-to-reflection ratio of the beamsplitter becomes asymmetric towards the lower frequency bound. The upper (theoretical) limit stems from the helium-neon alignment laser used to measure the interferometer position. A more practical limitation is the emission range of the DELTA THz source which is between about $50\,\mathrm{GHz}$ and $7\,\mathrm{THz}$.

The commercial spectrometer features an automatic in-vacuum (typically 2 to 3 mbar) beam path changer to switch between multiple detector and source ports. Two internal sources, a Globar and a mercury arc lamp can be used for calibrating the spectrometer and for transmission spectroscopy of samples in the evacuated sample chamber. The third source port is connected to the DELTA THz beamline (BL5a) through a valve which holds a z-cut quartz window in the gate. Since the beamline is typically operated at $2 \times 10^{-6}\,\mathrm{mbar}$, the valve window is used for preparatory measurements during which the beamline vacuum shall not be affected. For full optical transmission, the valve is opened at cost of worse vacuum conditions in the beamline. Two DLaTGS[2] detectors, one for the far-infrared and one for the mid-infrared region, are mounted inside the spectrometer housing. Additionally, a silicon bolometer is attached from the outside of the housing. This detector is the optimal detector for measurements with laser-induced THz radiation.

4.7 Commissioning of a polarizing THz spectrometer

The optical design of a new Fourier-transform spectrometer to be used at the DELTA THz beamline was carried out in [157]. Within this doctoral thesis, the electronic readout and integration to the DELTA control system were commissioned and the device was used for the diagnostics of THz pulses at DELTA [168]. The spectrometer should extend the observable spectral range to frequencies below $1\,\mathrm{THz}$ and hence, low-frequency compatible beam splitters were needed. An efficient approach is to use polarizers made of free-standing wire grids. If the beam splitting and recombination is based on polarization, moving the delay line of the spectrometer changes the ellipticity of the polarization of the recombined beam.

One approach to efficiently split a THz beam with symmetric intensity distribution between transmitted and reflected beam is to use polarizers made of free-standing wire grids. Named after the inventors of the first spectrometer using wire grids, this spec-

[1] commonly known as Mylar, a brand of DuPont
[2] DLaTGS: Deuterated Lanthanum α-Alanine doped TriGlycine Sulphate, a pyroelectric detector

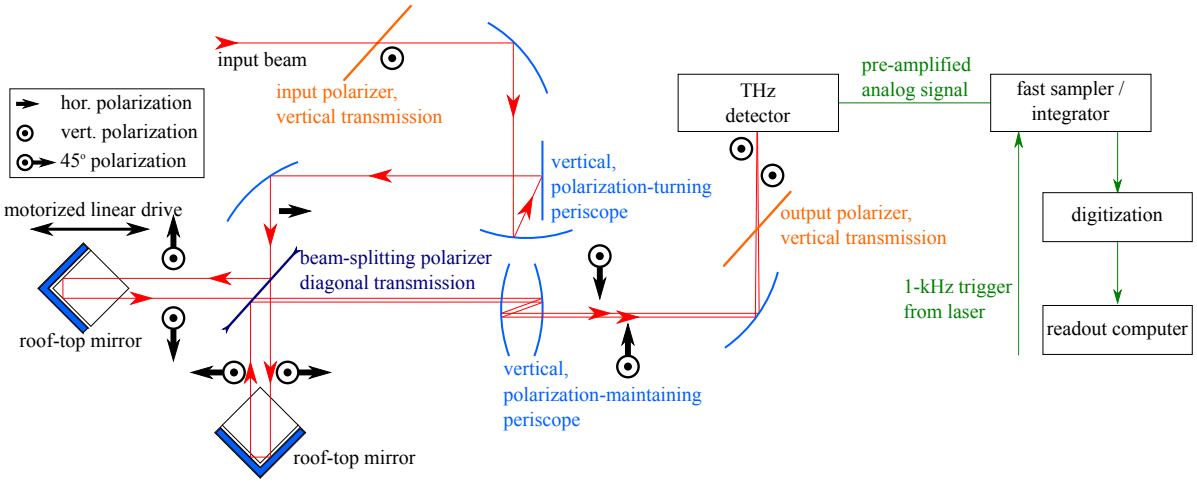

Figure 4.4: Setup of the Martin-Pupplet interferometer. (See text for details.)

trometer type is called Martin-Puplett interferometer [169, 170]. The wire grids used here, consist of $5\,\mu\mathrm{m}$ thick gold-plated tungsten wire with a period of $12.5\,\mu\mathrm{m}$.

Figure 4.4 shows the setup of the polarizing spectrometer.

4.7.1 Readout

In order to distinguish signals from different storage ring revolutions, the readout electronics of the spectrometer needed to have a sampling rate of at least the storage ring revolution time $1/T_0 = 2.6\,\mathrm{MHz}$. One of the standard detectors used with the spectrometer is the YBCO detector [171] which has an RF bandwidth of $55\,\mathrm{GHz}$ including the output amplifier [172]. The detector itself as well as the amplifier is very sensitive to electro-static discharge and also to RF reflections. Consequently, any part in the readout chain needs to provide a clean $50\,\Omega$ impedance over a broad bandwidth. Other detectors which are used with the spectrometer are a Schottky-barrier detector and a silicon bolometer.

Two different options for the readout of the respective detector are used:

- **oscilloscope readout**: A fast oscilloscope (Teledyne LeCroy WavePro 804HD) is used to aquire a single-turn signal from the attached detector. To synchronize the interferometer delay measurement with the data acquisition, both signals are distributed digitally via the storage ring control system. The maximum trigger rate of the oscilloscope depends on the setting of the sampling rate but is limited to about $30\,\mathrm{Hz}$. Hence, only a small fraction of the THz pulses with a repetition rate of $1\,\mathrm{kHz}$ is acquired.

- **fast sampler**: the standard use of the spectrometer relies on a gated integrator and a fast sampler. The sampler uses an integrating track-and-hold amplifier to provide a droopless analog DC voltage. The integration gate is adjustable between $100\,\mathrm{ps}$ and $1\,\mathrm{ns}$ and the maximum analog bandwidth is $3.5\,\mathrm{GHz}$. The analog output voltage is digitized with an FPGA based single-board computer (Red Pitaya 125-14). The commercially available board was modified to synchronize it directly to the DELTA RF system which provides a frequency divided signal of $125\,\mathrm{MHz}$. This readout chain allows to sample each THz pulse arriving with a rate of $1\,\mathrm{kHz}$.

After commissioning the spectrometer, the output was first used with a single detector. However, the last polarizer provides two beams, one in transmission and one in reflection, which contain orthogonal information. Placing two detectors at the output allows to perform a balanced detection which gives a background-free combined interferogram I_B

$$I_B = \frac{I_\mathrm{h} - I_\mathrm{v}}{I_\mathrm{h} + I_\mathrm{v}} \tag{4.14}$$

as function of the interograms acquired with horizontal and vertical polarization, respectively.

In the early commissioning phase, only one detector of each type was available. Later, two Schottky-barrier detectors of the same model were used for detection of signals below $2\,\mathrm{THz}$.

4.7.2 Beam size in the spectrometer

According to the description of the Gaussian beam in Chap. 3, a Gaussian beam either converges or diverges but mathematically, a collimated beam does not exist. Since the spectrometer splits and recombines a THz beam with an adjustable delay, a collimated beam would be ideal to maintain a perfect transverse overlap of the two beams. When increasing the beam diameter that it varies only slightly along the longitudinal coordinate, it can be regarded as quasi-collimated. Figure 4.5 shows the evolution the THz beam size $w(z)$ in the spectrometer after the viewport of the beamline .

4.7.3 Alignment

Since the THz beamline at DELTA uses telescopes comprising mirrors with optical quality, visible radiation from the bending magnet is available at the beamline port. The visible radiation is ideally suited for the alignment of the spectrometer. To prepare

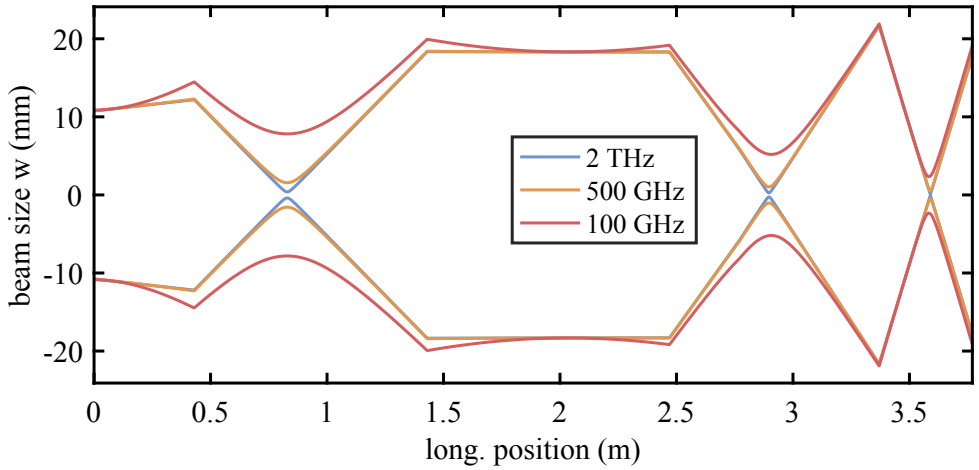

Figure 4.5: Evolution of the beam size after the viewport of the THz beamline inside the spectrometer.

the spectrometer for operation, the polarizing beam splitters are replaced by thin glass beam splitters which are mounted at the same position as the polarizers. The beams from both interferometer arms are aligned such that the final focus reaches the sensitive area of a Schottky-barrier detector. The optical beamsplitter allows to measure a first THz signal at the detector since glass holds a certain reflectivity around 200 GHz. After finding the overlap, the optical beamsplitter was replaced by the wire grid polarizers which increased the detector signal by about two orders of magnitude and allowed to take data in a board frequency range.

4.7.4 Spectral measurements with the polarizing spectrometer

The polarizing spectrometer allows spectral measurements between $50\,\mathrm{GHz}$ and $6.5\,\mathrm{THz}$. The new device enlarged the accessible frequency range towards the lower end, especially below $1.3\,\mathrm{THz}$. Figure 4.6 shows spectra of coherent THz radiation which were acquired during the revolution of the laser-electron interaction. This is sometimes referred to as turn-0 data (e.g. [153]).

The spectrum shown in red is based on a laser-electron interaction with an 800-nm laser beam while the curve shown in blue is generated using frequency-doubled pulses at $400\,\mathrm{nm}$. The laser pulse energy at $800\,\mathrm{nm}$ was about $3.8\,\mathrm{mJ}$ and the 400-nm pulses had a pulse energy of about $2.2\,\mathrm{mJ}$. The strength of the laser-based energy modulation ΔE determines the longitudinal movement of the modulated electrons $\Delta z = R_{56} \cdot \Delta E$. A stronger modulation causes a wider separation of the electrons resulting in a broader longitudinal density dip which causes a spectrum at lower frequencies. For that reason, the 800-nm laser beam causes a turn-0 spectrum centered about approximately $2\,\mathrm{THz}$,

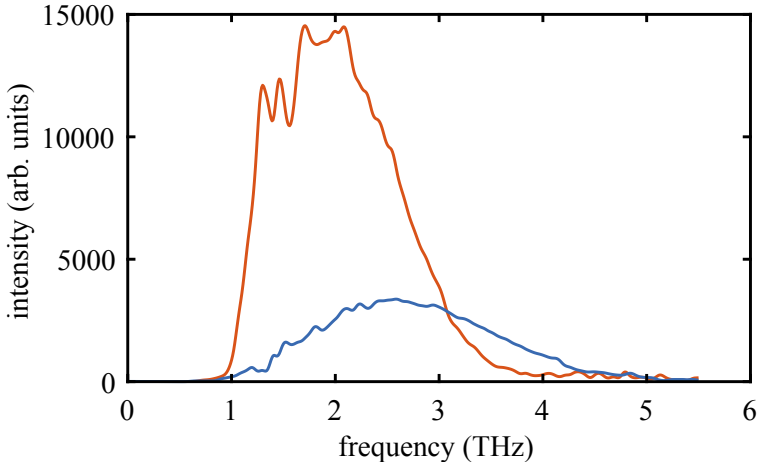

Figure 4.6: Spectra of coherently emitted THz pulses measured with the polarizing Fourier-transform spectrometer. The spectrum shown in red was acquired after a laser-electron interaction with an 800-nm laser beam whereas the blue curve is based on an interaction of a 400-nm laser beam (see text for details).

while the 400-nm laser beam results in turn-0 spectrum centered at about 2.3 THz. The measurement was performed using a silicon bolometer.

Two examples of interferograms acquired with the new spetrometer are shown in Fig. 4.7. The raw data shown here was taken using a Schottky-barrier detector gated to turn-1 after the laser-electron interaction (left) and turn 2, respectively.

The corresponding spectra are shown Fig. 4.8. The central frequencies of the turn-1 and turn-2 spectra agree well with the simulation-based predicted values in Tab. 3.4. The clear shift towards lower frequencies from one turn, centered at about 140 GHz to the other one centered at 90 GHz is visible. The interferograms show a good symmetry about the zero-delay position and show a clear modulation pattern. The minima of the

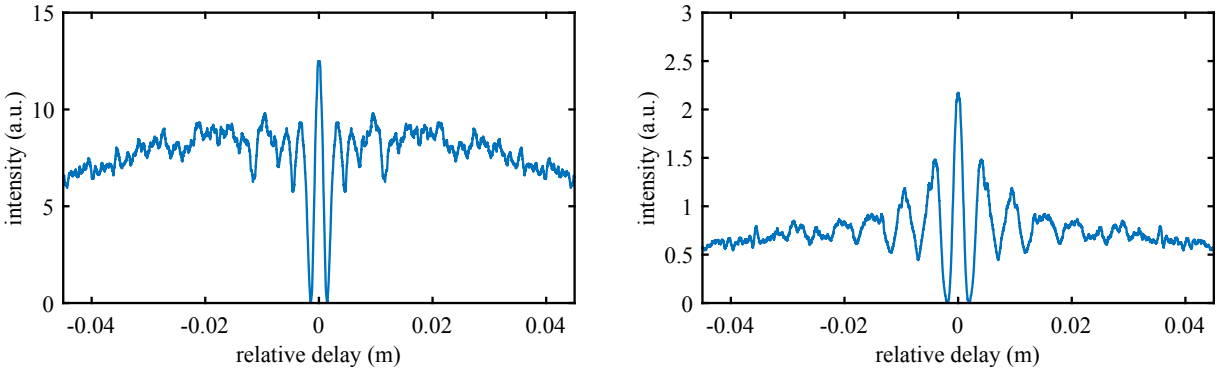

Figure 4.7: Interferograms of the turn-1 (left) and turn-2 signal (right) (see text for details).

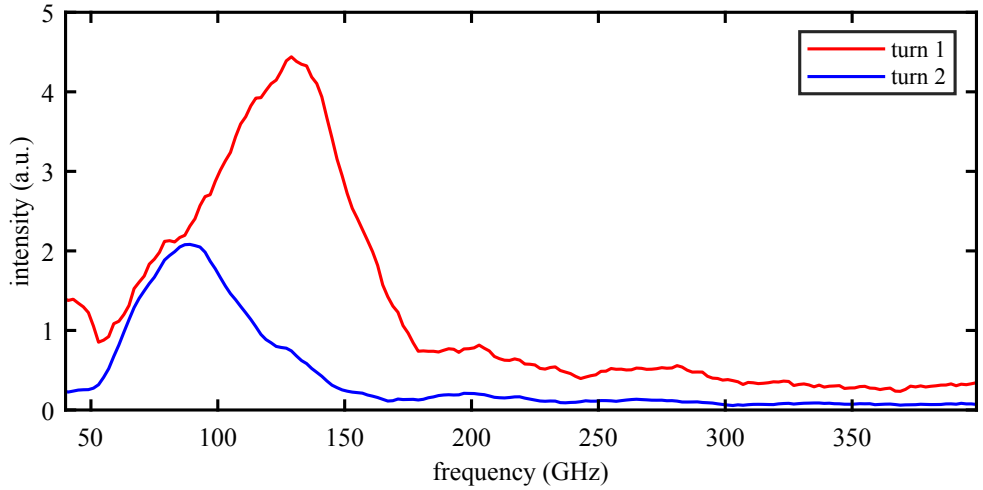

Figure 4.8: Coherent spectra of turn 1 and turn 2 after the initial laser-electron interaction.

interferograms are close to zero which means that the intensity distribution in the two interferometer arms is symmetric, too.

5 Pulse shaping of laser and THz radiation

In the previous chapter, the spectral diagnostics equipment developed and used to detect THz radiation at DELTA was described. Currently, sources of THz radiation with flexible spectro-temporal control remain rare. In the following sections, experimental results from DELTA are presented, demonstrating different approaches to achieving precise spectro-temporal control.

A key aspect of this control is the temporal shaping of the laser pulse intensity, which directly influences the spectro-temporal characteristics of the THz pulse. Compared to the standard operating mode described in Chapter 3, the laser pulses used for the electron-energy modulation are longer (up to approximately 20 ps FWHM) and exhibit a periodic intensity modulation. The increased pulse duration enables the generation of narrow spectral features, as the spectral resolution is inversely related to pulse duration (Fourier theorem).

The techniques presented include two types of interferometric pulse-shaping approaches and a computer-controlled setup utilizing an adaptive optical element, specifically a reflective spatial light modulator (SLM). The characterization of these setups, experimental results, and theoretical limitations are discussed.

The laser amplifier described in Chapter 3 relies on the chirped-pulse amplification scheme, which means that after amplification, a grating compressor is used to temporally compress the laser pulses. Table 5.1 summarizes different settings of the grating compressor. Setup 1 is the standard mode of operation of the short-pulse facility.

Measurements using GRENOUILLE FROG showed a minimum laser pulse duration of about $40\,\mathrm{fs}$. For simplicity, it is assumed that the laser pulse is transform-limited in this configuration, implying $D_2 = 0$ and $D_3 = 0$. However, a transform-limited laser pulse with an 800-nm wavelength, a 40-fs pulse duration, and a Gaussian shape would have a spectral width of $23.6\,\mathrm{nm}$ (FWHM), which is significantly smaller than the measured $30\,\mathrm{nm}$. Nevertheless, this discrepancy can be neglected, as the following experiments

Table 5.1: Overview of different laser pulse compressor configurations used for the experiments described in this chapter. Values of D_2 and D_3 refer to the effective laser pulse dispersion, not the correction induced by the compressor. The angle of incidence on the first grating is given by ϑ_{in} and d is the grating distance. All setups were designed based on gratings with a spatial grating-line frequency $g = 1500\,\text{mm}^{-1}$.

Setup	**spectral phase**	**estimated pulse length**
1) Fully compressed, ultrashort pulses		
$\vartheta_{\text{in}} = 51.3°$, $g = 1500\,\text{mm}^{-1}$ $d = 265\,\text{mm}$	$D_2 = 0\,\text{ps}^2$ $D_3 = 0\,\text{ps}^3$	$\Delta t = 40\,\text{fs}$ (FWHM)
2) Partial compression		
$\vartheta_{\text{in}} = 51.3°$, $g = 1500\,\text{mm}^{-1}$ $d = 235\,\text{mm}$	$D_2 = 1.64 \times 10^{-1}\,\text{ps}^2$ $D_3 = -5.60 \times 10^{-5}\,\text{ps}^3$	$\Delta t = 11.3\,\text{ps}$ (FWHM)
3) Partial pulse compression for pulse optimization by a phase modulator		
$\vartheta_{\text{in}} = 51.3°$, $g = 1500\,\text{mm}^{-1}$ $d = 210\,\text{mm}$	$D_2 = 3.00 \times 10^{-1}\,\text{ps}^2$ $D_3 = -1.03 \times 10^{-4}\,\text{ps}^3$	$\Delta t = 20.8\,\text{ps}$ (FWHM)
4) Uncompressed laser pulses		
(compressor bypassed)	$D_2 = 1.45\,\text{ps}^2$ $D_3 = -4.95 \times 10^{-4}\,\text{ps}^3$	$\Delta t = 100\,\text{ps}$ (FWHM)

use long pulse durations of several picoseconds, making the full-compression setting less critical.

Setup 2 is an alternative configuration of the standard compressor. Here, by reducing the grating distance, a pulse duration of about $11\,\text{ps}$ is achieved. These pulses were used for initial attempts to reduce the spectral bandwidth of the THz pulses.

Another compressor setting (cf. Setup 3, Tab. 5.1) involves tuning the default compressor to achieve a resulting pulse duration of $20.8\,\text{ps}$. In this case, a significant amount of TOD remains but is compensated later using an SLM-based phase-shifter setup.

All dispersion values and pulse durations given in Tab. 5.1 were calculated using Eqs. 2.86 and 2.87. The setups listed were used to generate laser pulses of different durations, which were then modulated in different ways to control the resulting THz spectrum.

5.1 Variation of the laser pulse length

When the DELTA short-pulse facility is operated in CHG mode, shortest laser pulses of about $40\,\text{fs}$ are used for the laser-electron interaction. The generation of THz radiation,

however, is possible with longer laser pulses, too. When using longer laser pulses, the THz radiation intensity increases because more electrons are modulated.

As a first step towards better spectral control of the THz spectrum, the built-in grating compressor of the laser system was detuned to increase the laser pulse length. The grating compressor is built of two parallel gratings and a roof-top mirror like the compressor depicted in Fig. 2.19. The angle of incidence is $\Theta_{\text{in}} = 51.3°$ and the distance of the gratings at full compression of the laser pulse is $265\,\text{mm}$ which leads to a fully compressed pulse duration of $40\,\text{fs}$. According to Eqs. 2.86 and 2.87, the GDD corrected by the compressor is $D_2 = -1.45\,\text{ps}^2$ and the TOD is $D_3 = 4.95 \times 10^{-4}\,\text{ps}^3$.

Figure 5.1 (top) shows the tuning capabilities of the pulse compressor in its standard configuration. The distance can be shrunk to about $185\,\text{mm}$ which leads to a maximum pulse duration of about $30\,\text{ps}$. The detuning of the compressor leads to a significant occurence of third order dispersion which is depicted in Fig. 5.1 (bottom).

5.2 Seeding with laser double pulses

To further study the influence of the laser pulse shape on the generated THz spectra, a Michelson interferometer was installed in the laser beam path to either create two distinct energy modulation regions on the electron bunch or to generate a laser pulse with intensity beating, which then interacts with the electron bunch.

A first version of the interferometer was kindly provided by PhLAM[1], Lille University, France [173]. Later experiments were conducted using optical setups designed and built as part of this thesis.

Figure 5.2 shows the optical setup, including the Michelson interferometer positioned after the laser pulse compressor. The interferometer is built so that the pulse passes through the same amount of glass in the beamsplitters and mirrors, minimizing nonlinear effects such as self-phase modulation. After the interferometer, the laser pulses are focused at the center of the undulator to interact with the electron bunch. A USB-based CCD[2] fiber spectrometer detects the laser pulses at a second interferometer output. Experimentally, it is highly feasible to acquire the spectrum for measuring the delay setting of the interferometer.

[1] PhLAM: Laboratoire de Physique des Lasers, Atomes et Molécules
[2] charge-coupled device

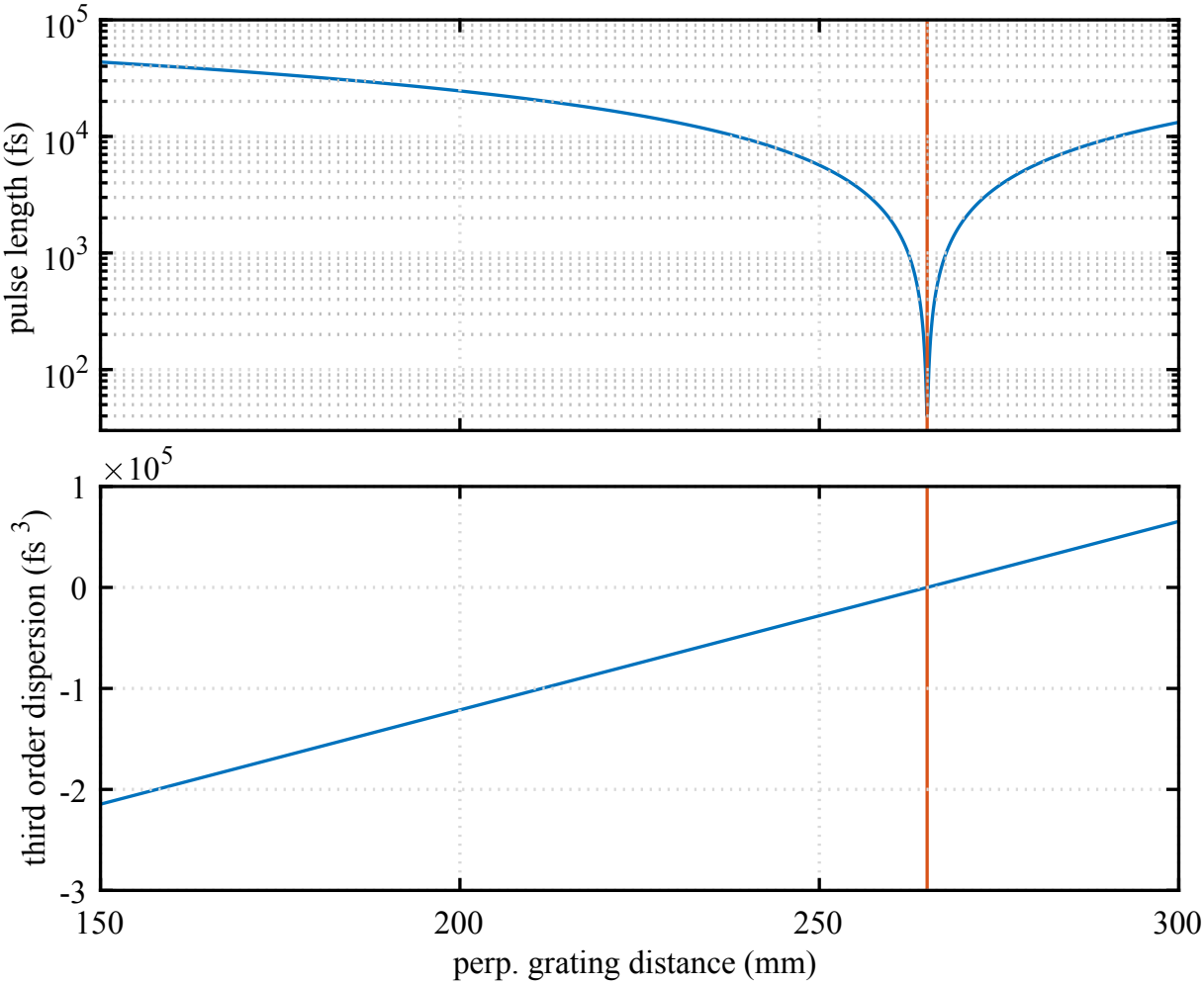

Figure 5.1: In its standard configuration, the grating compressor of the laser amplifier is set to a grating distance of $265\,\mathrm{mm}$ and an angle of incidence of $51.3°$. In this configuration, the minimum pulse duration of approximately $40\,\mathrm{fs}$ is achieved. The pulse length can be adjusted by varying the grating distance (top). The third-order dispersion (TOD) increases linearly with the grating distance (cf. Eq. 2.87) (bottom).

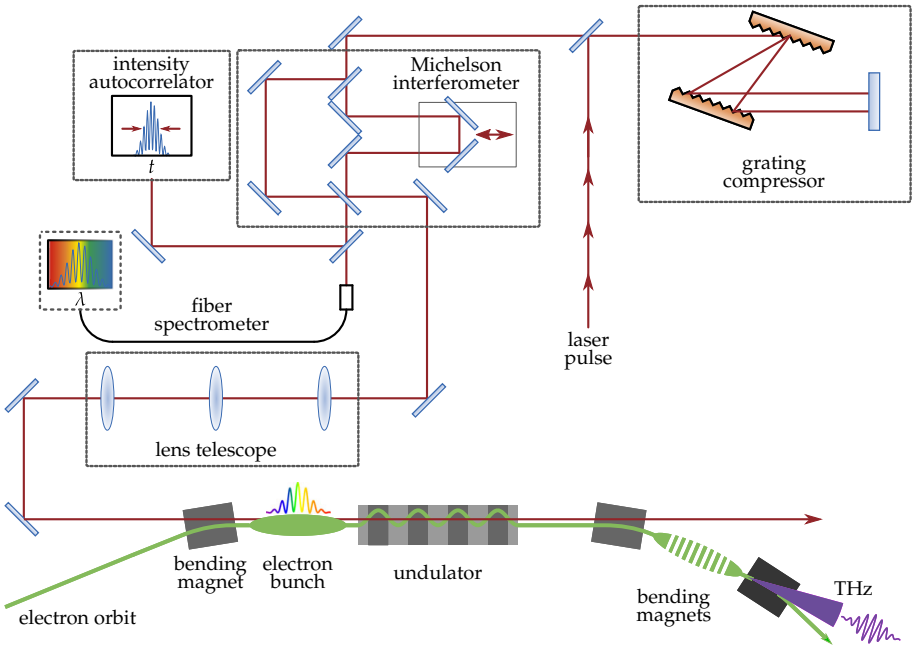

Figure 5.2: Setup to generate laser double pulses and also intensity modulated laser pulses. The laser pulse duration is adjustable using a Treacy-type laser pulse compressor and then guided to a Michelson interferometer offering two outputs one of which is used for the energy modulation of the electrons in the storage ring. The other output is used for diagnostics in a spectrometer and an autocorrelator.

5.2.1 Pulse delay measurement from modulated laser spectra

The measurement of laser pulse delays is essential for the correct alignment of interferometers used with pulsed lasers. In this thesis, several kinds of interferometers were used to generate copies of laser pulses or to induce a temporal modulation. In Fig. 5.2 the fiber spectrometer is used to measure the laser pulse delay in the interferometer. The trivial case of a delay $\Delta t = 0$ equals the spectrum I_1 of a single pulse which reads

$$I_1(\omega) = \frac{cn\epsilon_0}{2} \left|\tilde{\mathcal{E}}(\omega)\right|^2 = A^2(\omega) \, . \tag{5.1}$$

The spectral intensity $I_{12}(\omega)$ of both, pulse and delayed duplicate, shows a temporal interference which depends on the time delay Δt

$$I_{12}(\omega) = \frac{cn\epsilon_0}{2} \left|\tilde{\mathcal{E}}(\omega) + \tilde{\mathcal{E}}(\omega) \mathrm{e}^{\mathrm{i}\omega\Delta \mathrm{t}}\right|^2 \tag{5.2}$$

$$= 2A^2(\omega) + 2A^2(\omega)\cos(\omega\Delta t) \, . \tag{5.3}$$

The cosine term in Eq. 5.3 is repsonsible for the occurence of interference fringes in the spectrum. Figure 5.3 shows laser spectra (vertical) as function of the delay setting of the

interferometer. Longer delays Δt cause high a high-frequency modulation in the spectrum. In the experiment, the zero-delay setting is found by reducing the modulation frequency.

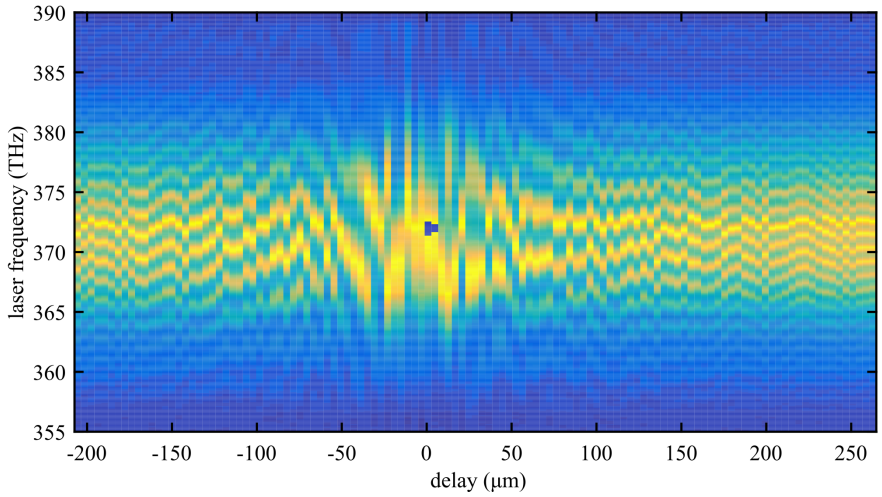

Figure 5.3: The CCD spectrometer shows an intensity modulation under variation of the laser pulse delay. The delayed laser pulses generate a cosine modulation in the laser spectrum which has frequency proportional to the delay time Δt. The blue spot in the middle is caused by unstable interference conditions close to equal time of arrival. Here, delay changes on the $\lambda/2$-scale occur due to air fluctuations and the intensity measured by the spectrometer shows the cancellation effect.

As a first test to influence the THz spectra, the laser pulse delays were varied between $20\,\mu\mathrm{m}$ and $80\,\mu\mathrm{m}$. In this regime, the region of the bunch which is energy-modulated increases with the delay setting which then leads to the formation of a wider density dip in the electron density. As shown in Fig. 5.4, in consequence, the central frequency shifts from approximately $3.4\,\mathrm{THz}$ to $2.3\,\mathrm{THz}$.

In this regime, the interferometer delay is only slightly longer than the pulse duration of $40\,\mathrm{fs}$. Larger delays of several millimeters cause the formation of distinctly energy-modulated regions on the electron bunch. Each of these regions gives rise to a broadband THz pulse. In the spectrometer, the temporal interference of these THz pulses is observed. Figure 5.5 shows two spectra acquired at laser pulse delays of $1.2\,\mathrm{mm}$ and $2.4\,\mathrm{mm}$, respectively. As expected, and similarly to the spectral observation of laser double pulses above, the longer delay of the two THz pulses results in a higher modulation frequency.

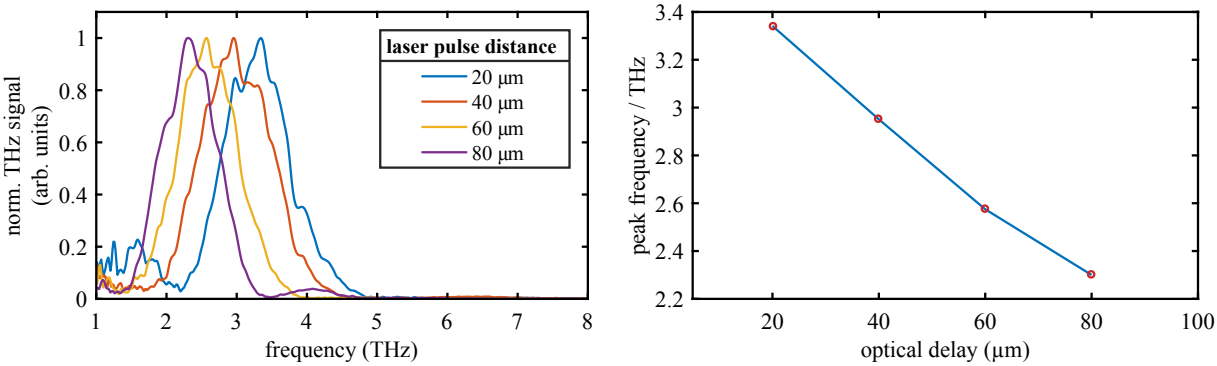

Figure 5.4: Spectra of coherently emitted THz radiation generated in a laser-electron interaction using short overlapping laser-double pulses (left) and frequency shift of the spectral peak intensity as function of the pulse delay (right). The pulse delay is only slightly longer than the pulse duration (40 fs) (adapted from [174]).

5.3 Chirp and delay technique for generation of narrowband THz radiation

The previous section showed that the temporal profile of the laser pulse significantly influences the THz emission spectrum. In the mid 1990s, a technique called chirped-pulse beating (CPB) was first realized using photoconductive antennas as THz emitters [175, 176]. Here, a partially compressed, chirped laser pulse travels through a Michelson interferometer where it is split and recombined with a variable delay. Superposing the two chirped pulses with a delay leads to a difference in the instantaneous frequency and results in an intensity beating with the periodicity of the difference frequency. If the initial chirp is purely quadratic, meaning the frequency variation along the pulse is linear, the beating frequency is constant. Such a laser pulse is used to modulate the electron energy with a periodic pattern which can give rise to the emission of narrowband radiation in the THz regime.

First experiments following this scheme at light sources were conducted at the UVSOR storage ring [177, 178]. In 2014, the same group from PhLAM, Lille University, France, provided their setup used to modulate the laser pulse intensity for experiments at DELTA [179, 153].

Within this thesis, a new optimized setup built for use at DELTA was realized. It offers the same functionality as the setup show in Fig. 5.2 and can be used for both, double pulse generation and the generation of intensity modulated pulses. The latter requires short delays compared to the relatively long pulse duration.

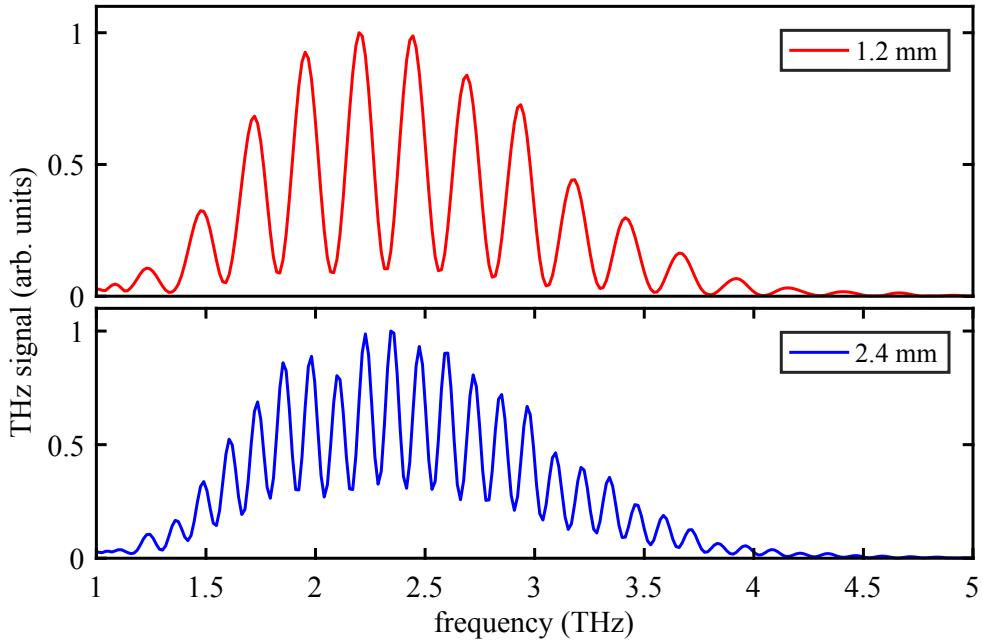

Figure 5.5: Spectra of two successive coherently emitted THz pulses with a relative distance of 1.2 mm (top) and 2.4 mm (bottom). Both spectra comprise an intensity modulation which is caused by the temporal interference of the two THz pulses (see text for details).

5.3.1 Derivation of the beating frequency

Figure 5.6 shows the instantaneous frequency of two laser pulses in the case of linear chirp (a) and quadratic chirp (b). Splitting and delaying two linearly chirped pulses generates a shift, leaving a constant distance of the two spectrograms. In consequence, the difference frequency is constant and, depending on the pulse delay, is a fraction of the spectral bandwidth. In the case of a quadratic chirp, the spectrograms have the shape of two shifted parabolas, which increase in distance as function of time. Hence, the difference frequency is not constant.

The time-dependent frequency of a chirped pulse is written as [180, 181, 182, 183]

$$\omega(t, D_2, D_3) = \omega_0 + \frac{1}{D_2}\, t - \frac{D_3}{2D_2^3}\, t^2 \tag{5.4}$$

Without third order dispersion, the instantaneous difference frequency of two purely linearly chirped pulses which are split, delayed by Δt and recombined reads

$$\Delta\omega(t) = \omega(t, D_2) - \omega(t + \Delta t, D_2) = \Delta t / D_2 \tag{5.5}$$

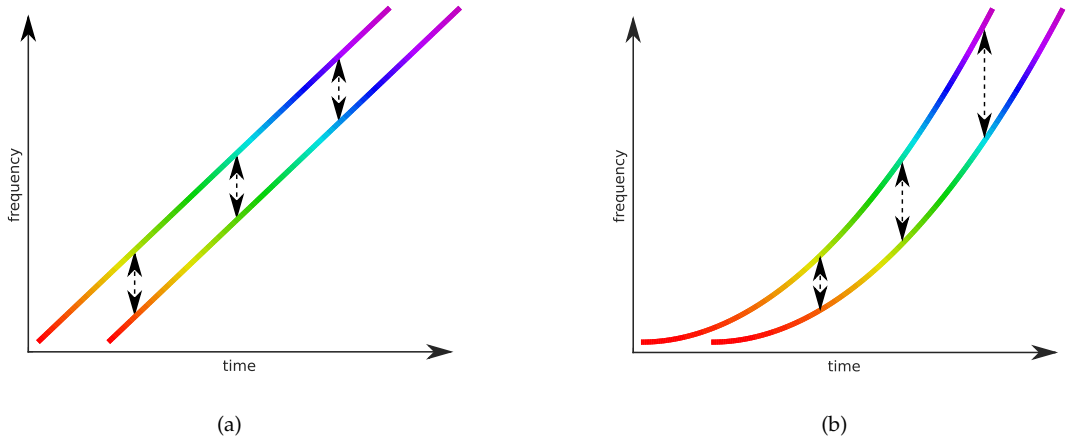

Figure 5.6: a) Two identical chirped laser pulses shifted in time have a constant difference frequency, if their instantaneous frequencies are a linear function of time. b) If the pulses are chirped non-linearly, the difference frequency varies over time and the spectrum of a difference-frequency generation process broadens.

in the case of non-zero third-order dispersion $D_3 \neq 0$, the resulting difference frequency is linearly chirped

$$\Delta\omega(t) = \left(\frac{\Delta t}{D_2} + \frac{D_3}{2D_2^3}\Delta t^2\right) - \left(\frac{D_3}{D_2^3}\Delta t\right) t. \tag{5.6}$$

Here, the second term is a linear variation of the difference frequency as function of time t.

Therefore, a large group delay dispersion D_2 improves the spectral width of the THz spectra in two ways:

1. the increased laser pulse duration leads to more intensity modulation cycles of the laser pulse which in turn lead to a narrowing of the spectra
2. the group delay dispersion scales down the third-order dispersion

5.3.2 Alignment of the chirped-pulse beating setup

The periodic intensity beating of the laser pulse was realized by using the setup already used in Sec. 5.2 to generate laser double pulses. The laser pulse compressor was tuned to an increased pulse length of about 20 ps (FWHM) by increasing the distance of the diffraction gratings. Since this changes the arrival time of the laser pulse with respect to the electron bunch, the so-called vector modulator which is used as a programmable laser delay is adjusted to correct for this delay. The long pulse duration facilitates set-

ting the correct frequency of the intensity modulation. Furthermore, the long pulse duration also allows to measure the temporal laser pulse profile with a streak camera. At DELTA, a streak camera is available at BL4 which is the diagnostics beamline of the U250 undulator. To check the laser profile and also the spatial alignment of the complete setup, the beating laser pulses were analyzed using the streak camera. Figure 5.7 shows measurements of the two interfering laser pulses (blue) and the temporal profile of each pulse (yellow, orange). A drop of the central intensity in the blue curve is visible which is caused by the interference of the two chirped and delayed laser pulses. Ideally, the central intensity of the blue curve should be close to zero, however, here only rough overlap conditions were checked and optimized later.

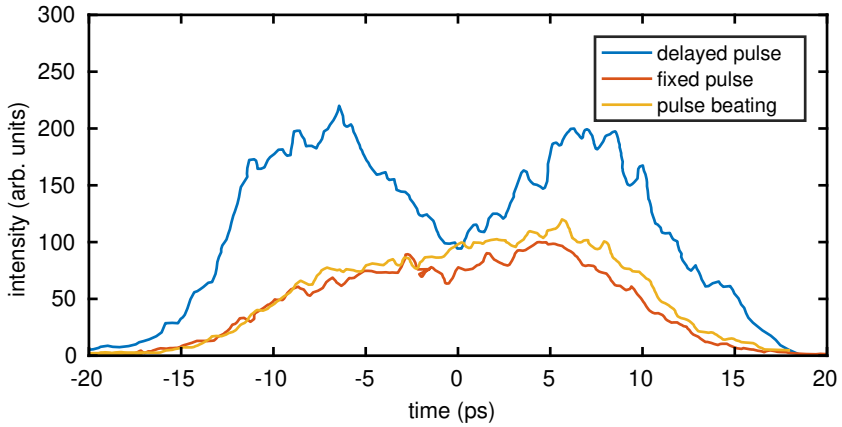

Figure 5.7: As a quick test whether the two interfering laser pulses overlap spatially and temporally, the laser pulses were guided to a streak camera after passing the eletromagnetic undulator U250. The long distance to the laser ensures a certain spatial and angular accuracy. The camera measures the laser intensity distribution over time. The yellow and orange curves depict the intensity profiles from single pulses, while the blue curve shows the profile of the inference. The beating frequency was set low enough to reach a picosecond-scaled modulation which is visible on the streak camera image.

A dedicated intensity autocorrelator was built to analyze the beating frequency online and to accurately align the chirp-and-delay interferometer. Figure 5.8 (left) shows an autocorrelation trace with a clearly visible intensity modulation on the picosecond scale.

Changing the interferometer delay increases the beating frequency. Figure 5.8 (right) shows the modulation frequency retrieved from the autocorrelation as function of the interferometer delay for small excursions leading to a maximum modulation frequencies of 1.1 THz. In this regime, the modulation frequency is a linear function of the delay. For larger delays, the autocorrelation shows a less clean modulation signal.

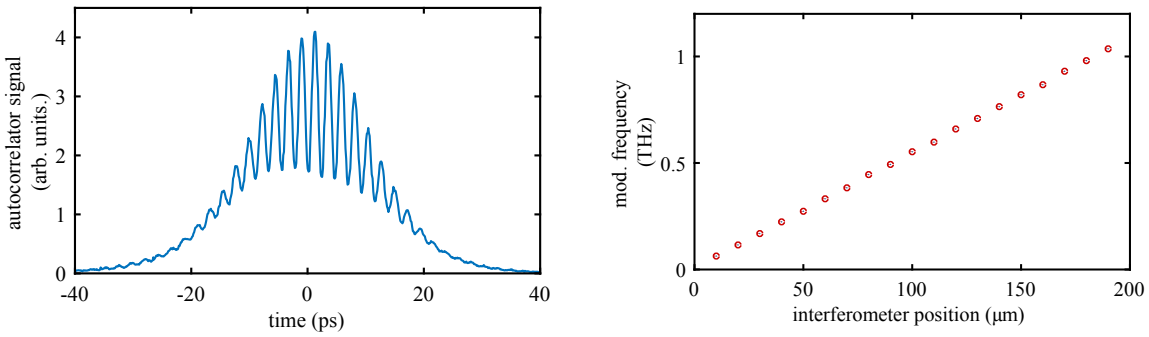

Figure 5.8: Left: Measurement of the variation of the intensity modulation frequency as function of the interferometer position. Right: Autocorrelation of a laser pulse which was intensity-modulated using the chirp-and-delay technique.

5.3.3 Tunable narrowband spectra

Using the intensity-modulated laser pulses for an energy modulation of the electron bunches leads to a narrowband emission of THz radiation in the frequency range up to 5.5 THz. Narrowband spectra above 1 THz generated by the split-and-delay technique are depicted in Figure 5.9. Here, the silicon bolometer was used as a detector for the spectrometer which excludes the spectral range below 1.3 THz.

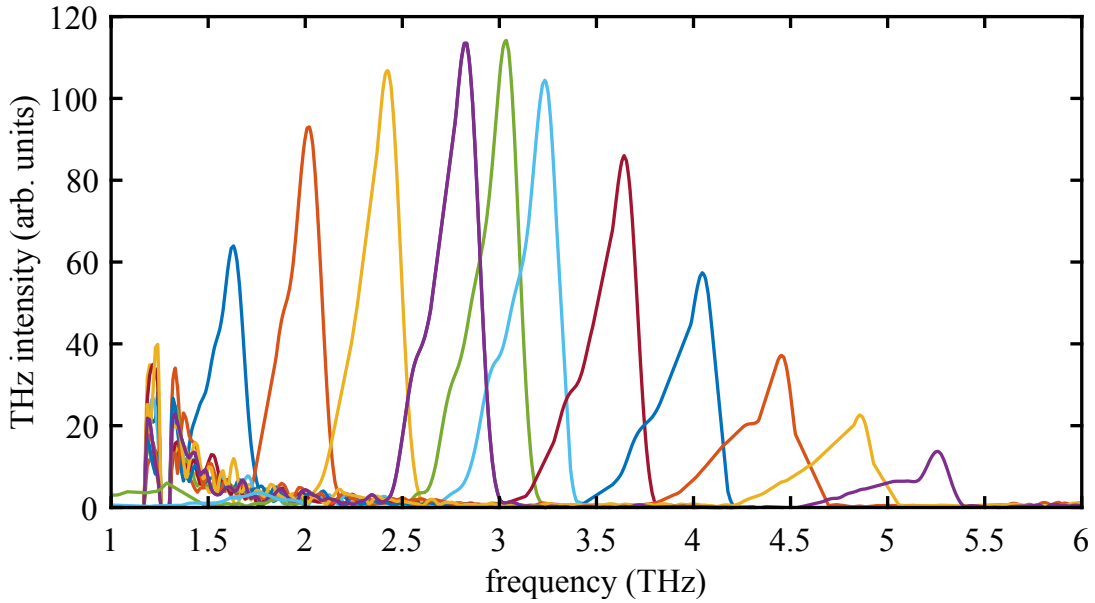

Figure 5.9: Spectra of coherently emitted THz radiation generated by the chirp-and-delay setup.

As expected from the third-order dispersion influence, the spectra become broader towards higher frequencies and become asymmetric. This is in agreement with the effect of the third-order dispersion: The intensity modulation of the laser pulse changes its

frequency along the pulse. If the Michelson interferometer is adjusted for modulation frequencies above $2.8\,\mathrm{THz}$, the spectral broadening is enhanced.

5.4 Tailored THz pulses from computer-controlled phase modulation

The fundamental configurations of optical 2-f and 4-f lines were discussed in Sect. 2.6.2. In these setups, the Fourier plane provides direct access to the spectral phase by establishing a correlation between a spatial coordinate and the instantaneous laser frequency. This correlation enables precise control over the spectro-temporal shape of laser pulses and facilitates the compensation of phase errors introduced by optical elements.

5.4.1 Fourier plane pulse shaping

An overview of linear filter functions in typical optical setups is provided in Tab. 2.1. These setups generally offer at most one degree of freedom, meaning that any modification to the spectral phase $\phi(\omega)$ affects both group delay dispersion (GDD) and third-order dispersion (TOD) simultaneously, as seen in grating and prism compressors.

More advanced linear filtering techniques in optics employ specialized grating compressors, known as zero-dispersion compressors or 4-f configuration compressors. This setup incorporates an additional telescope within the grating compressor, as illustrated in Fig. 5.10. A similar configuration was previously discussed in Chap. 2, Fig. 2.21.

A programmable pulse shaper based on this geometry was designed and built as part of this thesis. The setup consists of gratings with a line spacing of $1/1500\,\mathrm{mm}$, a telescope with horizontally focusing lenses of focal length $f = 75\,\mathrm{mm}$, and a spatial light modulator (SLM) with a width of $15.36\,\mathrm{mm}$ comprising 1920 phase-shifting pixels. The SLM has 1080 vertical pixels, but the applied phase shift remains constant along each vertical column, ensuring that dispersion occurs exclusively in the horizontal direction.

The gratings are arranged in the Littrow configuration, where the central wavelength of $805\,\mathrm{nm}$ has identical input and output angles, given by $\theta_{\mathrm{in}} = \theta_{\mathrm{out}} = 37.1°$.

In this configuration, the pulse shaper achieves a theoretical maximum pulse shaping complexity of $\eta = 1061$ and a maximum shaping time window of $T = 33.3\,\mathrm{ps}$.

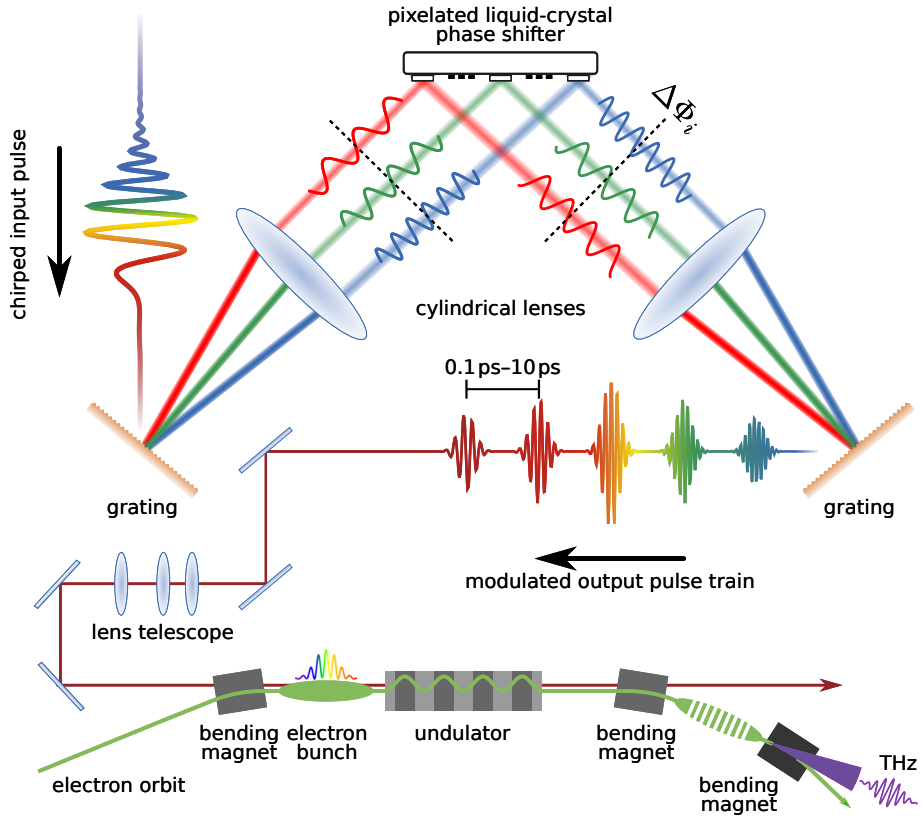

Figure 5.10: Sketch of the pulse shaping setup used to generate tailored THz pulses via laser-electron interaction in an electromagnetic undulator. The laser beam is dispersed by a first grating and focused by a cylindrical lens. A reflective phase shifter applies a frequency-dependent phase shift before the beam is recombined by a second grating into a pulse train, which can be computer-controlled through the phase shifter.

5.4.2 Analytic description of the phase-shift induced intensity modulation

Pulse shapers using zero-dispersion compressors are often laid out with help from automatic optimization routines based on machine learning approaches and genetic algorithms [184, 185]. In the experiments carried out in this thesis, the optimization was done manually by using a spectrometer and an autocorrelator as laser diagnostics. However, a simplified mathematical model helps to motivate the pattern and the strength of the phase modulation applied to the laser beam. To derive a formula for the modulation frequency, expressions known from signal theory were used [186].

The electric field of the laser pulse in time domain is expressed as

$$\mathcal{E}(t) \sim \cos\left[2\pi f_c \cdot t + \beta \sin\left(2\pi \cdot \frac{f_m}{2} \cdot t\right)\right]. \tag{5.7}$$

Here, f_c denotes the central frequency of the laser pulse and f_m is the target frequency of the intensity modulation of the laser pulse and β is the strength of the phase modulation. Although the phase manipulation with the spatial light modulator occurs in frequency domain, the simplified model can be evaluated in time domain because a purely linear chirp is assumed which gives a clear correlation between time and frequency. Using the definition of the Bessel function J_k, this expression can be rewritten as the sum of two series of even and odd Bessel functions

$$\begin{aligned}\mathcal{E}(t) \sim\ & J_0(\beta) \cdot \cos(2\pi f_c \cdot t) \\ & + \sum_{k=0}^{\infty} J_{2k}(\beta) \left\{ \sin\left[2\pi\left(f_c + 2k \cdot \frac{f_m}{2}\right)t\right] + \sin\left[2\pi\left(f_c - 2k \cdot \frac{f_m}{2}\right)t\right]\right\} \\ & + \sum_{k=0}^{\infty} J_{2k+1}(\beta) \left\{ \cos\left[2\pi\left(f_c + (2k+1)\frac{f_m}{2}\right)t\right] - \cos\left[2\pi\left(f_c - (2k+1) \cdot \frac{f_m}{2}\right)t\right]\right\}.\end{aligned} \tag{5.8}$$

With $J_n \approx 0$ for $n > 1$, this expression is simplified to

$$\mathcal{E}(t) \sim J_0(\beta)\cos(2\pi f_c \cdot t) + J_1(\beta)\left\{\cos\left[2\pi\left(f_c + \frac{f_m}{2}\right)t\right] - \cos\left[2\pi\left(f_c - \frac{f_m}{2}\right)t\right]\right\} \tag{5.9}$$

Because the energy modulation of the electrons by the laser depends on the intensity and not solely the electric field, the laser intensity is evaluated as

$$I = \frac{c\epsilon_0}{2}\mathcal{E}^2. \tag{5.10}$$

The expansion of $\mathcal{E}$ leads to contributions of the following modulation frequencies

$$f_{I1} = \frac{f_m}{2}, \quad f_{I2} = f_m, \quad f_{I3} = 2\left(f_c - \frac{f_m}{2}\right), \quad f_{I4} = 2f_c, \quad f_{I5} = 2\left(f_c + \frac{f_m}{2}\right). \tag{5.11}$$

The frequencies being a sum of the laser carrier frequency $f_c = 375\,\mathrm{THz}$ and the modulation frequency f_m are of the same order of magnitude as the carrier frequency which means that these are outside the possible modulation bandwidth. The remaining modulation contributions occur at f_m and $f_m/2$. This means that a modulation at f_m also generates a modulation at the sub-harmonic $f_m/2$.

For simplicity, this model assumes a monochromatic laser. Furthermore, the calculation was done in time-domain whereas the spectral phase is modulated. Assuming a linear

chirp of the laser pulse, the time coordinate t of the electric field of the laser pulse can be expressed as

$$t = (\omega(x_i) - \omega_0) \cdot D_2 \tag{5.12}$$

with $\omega(x_i)$ being the instantaneous frequency at the position of the i-th pixel and a phase shift per i-th pixel

$$\Phi_i = \beta \sin\left(2\pi \cdot \frac{f_m}{2} \cdot (\omega(x_i) - \omega_0) \cdot D_2\right). \tag{5.13}$$

In Chapter 2, the theory of linear filters was discussed. Any optical element changing only the spectral phase can be described by the multiplication of a complex factor $\exp(j\varphi(\omega))$ which adds a spectral phase. Due to the linearity, multiple filters can be added independently. This can be used to counteract the occurence of sub-harmonics in the modulation. Another modulation at $f_m/2$ with opposite phase reduces the unwanted sub-harmonic at $f_m/2$, but leads to a (weaker) sub-harmonic at $f_m/4$ which can be reduced by another modulation generated at $f_m/4$ with opposite phase, again. In the experiment, this series is stopped at $f_m/8$ because lower sub-harmonics were not observed.

Again due to linearity, any additional correction of the spectral phase that can be described by a linear filter, can be added to the phase shifter. Here, especially the correction of the third-order dispersion D_3 is corrected in the experiments described in the following. The procedure to calibrate the phase shift of a pixel as function of its 8-bit intensity level is described in the next subsection.

5.4.3 Alignment of the pulse shaper

Careful alignment and calibration of the pulse shaper setup are essential for achieving accurate performance. The procedure consists of the following steps:

1. **SLM Phase Calibration:** Before setting up the pulse shaper, the phase response of the SLM was calibrated using a Michelson interferometer, as shown in Fig. 5.11 (left). Both interferometer arms have a fixed length, while the arbitrary SLM control signal is used to modify the optical path difference. The resulting phase shift is shown in Fig. 5.11 (right). For small control values below 15, no response is observed. As the control level increases, the phase shift follows a nonlinear trend, with the rightmost section of the curve being less steep. The range indicated

by the red dashed lines allows for a maximum phase shift of 2π and is therefore used. A look-up table containing the calibration data is implemented on the single-board computer controlling the SLM.

2. **4f-Line Alignment:** Before using the pulse shaper, the alignment of the 4f-line must be verified. Ensuring that the focal plane of the first lens is positioned correctly at the depth of the first grating is crucial.

3. **Wavelength-to-Pixel Calibration:** The relation between wavelength and pixel position on the SLM was calibrated using an interference pattern and a spectrometer. This method is described in the following subsection.

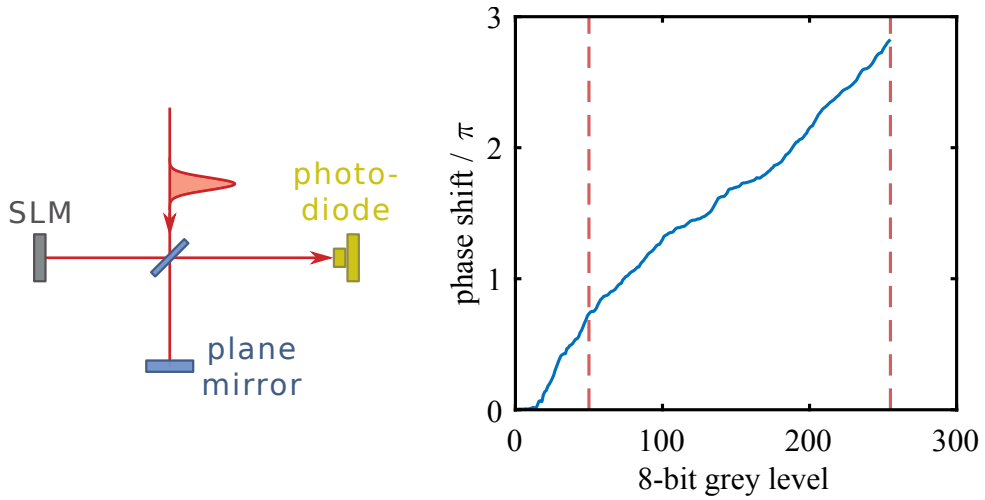

Figure 5.11: Setup used to calibrate the phase shift of the spatial light modulator (left) and resulting calibration curve (right). A phase shifting range of 2π is needed for the pulse shaping setup. The SLM is unresponsive for low grey levels between 0 and 15 and hence this region is not used for the experiments. Since the right part of the calibration curve is less steep, the region between the dashed red lines is used which also leads to a better phase shifting resolution. The calibration curve is used to implement a look-up table which uses the desired phase shift as an input.

5.4.4 Wavelength calibration of the Fourier plane using programmable interference patterns

The non-linear dispersion in the Fourier plane of the 4f-line has to be calibrated. First, a fiber-coupled spectrometer was used to measure laser spectra at different transverse positions of the Fourier plane. The single-mode fiber has a tight acceptance aperture of $12\,\mu\mathrm{m}$ which allows to transversely scan through the spectral components of the Fourier

plane. Furthermore, the correct position in laser beam direction can be found to optimize the distance between the focusing lens and the SLM. The spectral width measured with this method increases when the fiber coupler is out of focus.

To do a more precise mapping of the horizontal coordinate in the Fourier plane and the laser wavelength, the laser spectrum after the complete 4f-line was measured while introducing phase shifts of π for pairs of neighboring pixels. Figure 5.12 shows a laser spectrum with intensity dips caused by the destructive interference. If the gratings before and after the Fourier plane are out of focus, the interference pattern starts to blur because the frequency interval per phase shifter pixel increases and the interference condition is not fulfilled anymore. Using the spectral measurement, the central wavelength on each SLM pixel can be deduced. The result of the calibration is shown in Fig. 5.12.

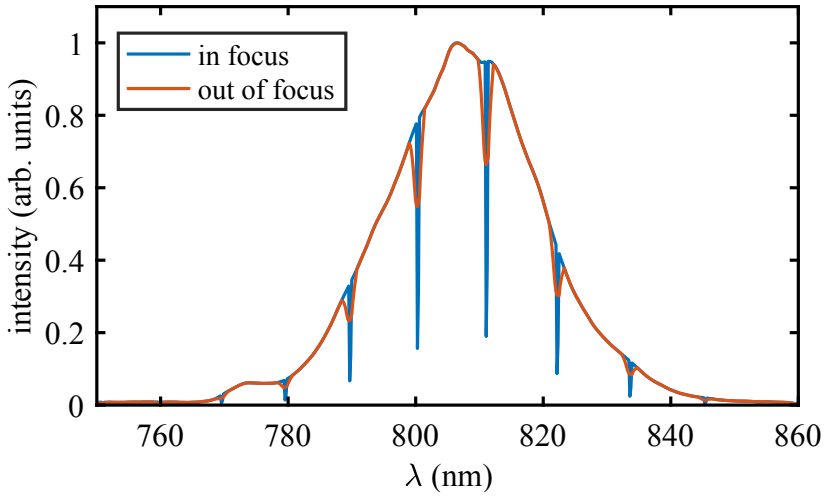

Figure 5.12: The relation between laser wavelength and pixel number on the spatial modulator was calibrated. Here, a phase pattern containing distinct phase shifts of $\phi_i = \pi$ was applied to the mask, leading to distinct intensity drops because of destructive interference (blue curve). Simultaneously, the distance between the first lens and the grating was optimized. When the grating is out of focus, the interference effect is less dominant because the frequency intervall $\delta\omega$ per pixel is increased (red curve) and the interference pattern blurs.

5.4.5 Nyquist-Shannon limit

The freedom of choice of the laser output pulse shape is also limited the Nyquist-Shannon limit. The Nyquist-Shannon sampling theorem known from signal theory [187, 188] causes an aliasing effect when phase differences of sampled signals become too large. The theorem states that any periodic function needs to be expressed by two

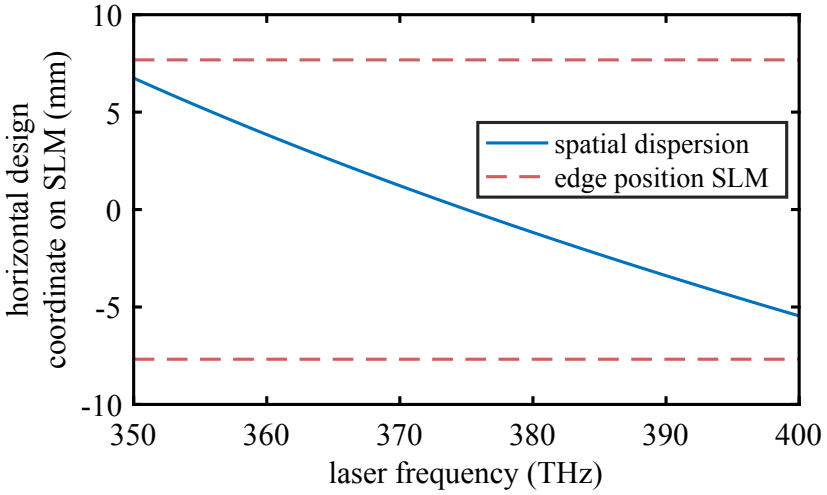

Figure 5.13: Spatial dispersion in the Fourier plane of the 4-f pulse shaper. The dispersion of the first grating leads to a slight asymmetric distribution of the outermost spectral contributions. For the ease of alignment, the central laser frequency $f_c = 375\,\mathrm{THz}$ was aligned in the middle of the SLM.

points per period. Otherwise ambiguities arise. While the sampling theorem is usually discussed in time domain when choosing the correct sampling rate for data acquisition, a plausible view in spectral domain of the phase shaper is that a phase shift of 2π needs to be sampled by at least two pixels. This defines a maximum steepness of the phase function applied to the modulator.

A linear phase variation is limited by a phase shift of $\delta\Phi < \pi$ between two neighboring pixels. This leads to a maximum linear dispersion of

$$D_1 = \pi/\delta\omega = 120.64\,\mathrm{ps} \tag{5.14}$$

The condition that the slope per pixel must not exceed a phase shift of π also holds for the quadratic phase. The phase shift of the n-th pixel is

$$\Phi_2(n) = D_2\,\delta\omega^2\left(n - \frac{N}{2}\right)^2 \tag{5.15}$$

and the largest phase advance per pixel is between pixel N and pixel $N-1$

$$\delta\Phi_{\max} = D_{2,\max}\,\delta\omega^2 \underbrace{\left\{\left[N - \frac{N}{2}\right]^2 - \left[(N-1) - \frac{N}{2}\right]^2\right\}}_{N-1} \tag{5.16}$$

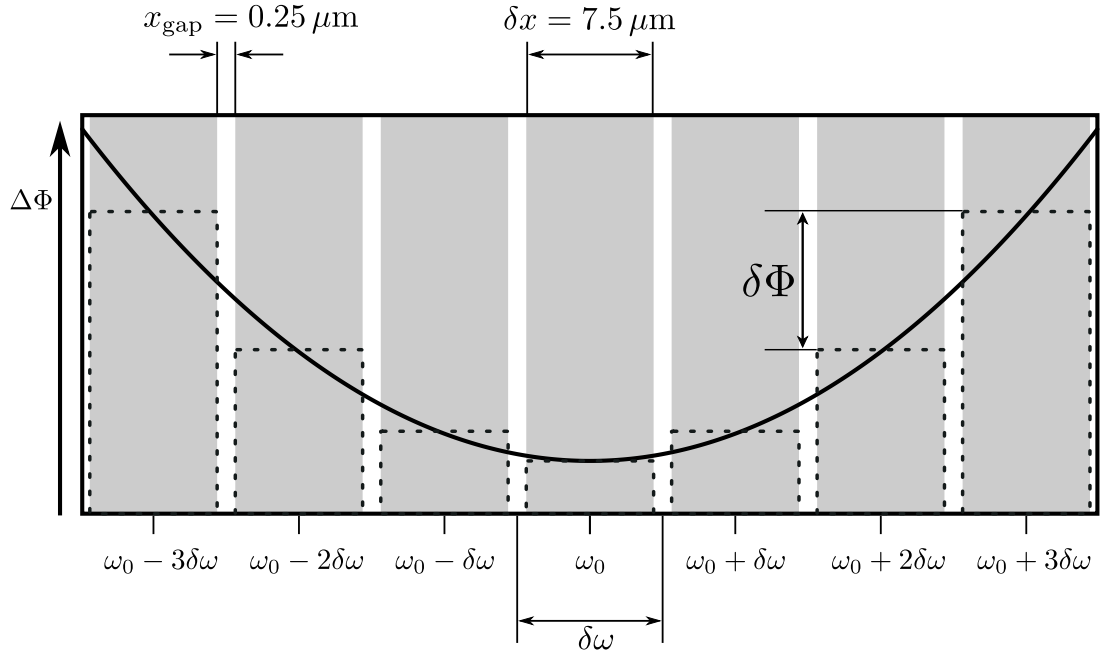

Figure 5.14: Simplified model of the LCD phase shifter matrix. Each pixel is illuminated by light of a certain frequency interval $\delta\omega$. Between the pixels, a metallization layer introduces gaps which do not contribute to the applied phase shift. The spectral-phase advance between two neighboring pixels must not exceed a value of π which sets limits for the maximum values of the dispersion correction (see text for details).

which leads to a maximum group delay dispersion of

$$D_{2,\mathrm{max}} = \frac{\pi}{(N-1)\delta\omega^2} = 1256.66\,\mathrm{fs}^2. \tag{5.17}$$

Applying a cubic phase, the phase advance per pixel n reads

$$\Phi_3(n) = D_3\,\delta\omega^3 \left(n - \frac{N}{2}\right)^3. \tag{5.18}$$

Again, the maximum phase difference for a cubic phase advance occurs between pixel N and $N-1$. It reads

$$\delta\Phi_{\mathrm{max}} = D_{3,\mathrm{max}}\,\delta\omega^3 \left\{\left[N - \frac{N}{2}\right]^3 - \left[(N-1) - \frac{N}{2}\right]^3\right\} \tag{5.19}$$

leading to a maximum third-order dispersion of

$$D_{3,\mathrm{max}} = \frac{\pi}{\left(\frac{3}{4}N^2 - \frac{3}{2}N + 1\right)\delta\omega^3} = 6.4 \times 10^7\,\mathrm{fs}^3. \tag{5.20}$$

Comparing these values to the GDD and TOD of the laser pulse compressor shows that the pulse shaper cannot replace the grating compressor when used in this configuration. For specific applications, a redesign of the pulse shaping setup could be possible which allows to avoid the grating compressor. This would be beneficial, since the grating compressor causes an intensity loss of about 20 %. However, the unwanted TOD introduced by the pulse compressor can be corrected with the pulse shaper since it is lower than $D_{3,\mathrm{max}}$.

5.4.6 Discretization of the pixel size

The SLM with a neutral phase pattern (constant phase shift or a phaseshift linear with frequency ω) still applies a periodic amplitude filter caused by the gaps between the pixels. The amplitude modulation pattern can be written as

$$\tilde{M}(\omega) = \left(\tilde{H}(\omega) \sum_{n=-N/2+1}^{n=N/2} \delta(\omega - n\delta\omega) \right) * \mathrm{rect}(\omega/\delta\omega) \tag{5.21}$$

with the Dirac delta distribution $\delta(\omega - n\delta\omega)$, the gate function $\mathrm{rect}(\omega/\delta\omega)$ and $*$ being the convolution operator.

The influence on the output pulse $\mathcal{E}_{\mathrm{out}}(t)$ is described by

$$\mathcal{E}_{\mathrm{out}}(t) \sim \left[\mathcal{E}_{\mathrm{in}}(t) * \sum_n h\left(t - n\frac{2\pi}{\delta\omega}\right) \right] \cdot \mathrm{sinc}\left(\frac{\delta\omega \mathrm{t}}{2}\right) \tag{5.22}$$

Copies of the original pulse arise due to the spatial amplitude modulation by the pixel metallization. The impulse response function $h(t)$ influences the output pulse. The term $h(t - n2\pi/\delta\omega)$ contributes at distinct times $t = n2\pi/\delta\omega$. In principle, the zeros of the term $\mathrm{sinc}\,(\delta\omega \mathrm{t}/2)$ counteract the occurence of the pulse copies, but $\delta\omega$ is only approximated as a constant and hence, the pulse copies are not fully suppressed which leads to pulse copies at delays of

$$\tau_{\mathrm{rep}} \approx n \cdot \frac{2\pi}{\delta\omega}. \tag{5.23}$$

In the experiment, the pulse copies do not temporally overlap with an electron bunch and are only visible in the diagnostics equipment.

5.4.7 Phase flickering

As any active electronic device, the pixels of the SLM are subject to electronic noise. During the alignment routine presented in Fig. 5.12, it was observed that the intensity minima start to blur if the laser intensity reflected by the SLM is too high. Stable operation is achieved at an average laser power of $1\,\mathrm{W}$ and pulse durations not lower than $20\,\mathrm{ps}$.

5.4.8 Measurements of narrowband THz radiation

Correcting the third order dispersion of the grating compressor with the SLM allows to imprint a single-frequency intensity modulation on the laser pulse. Figure 5.15 shows a set of THz spectra under variation of the central frequency and the bandwidth which can be controlled by changing the number of sinusoidal phase modulation periods on the SLM.

The spectra were acquired using the silicon bolometer. The minimal spectral bandwidth achieved is on the order of 100 GHz (top). In contrast to the narrowband spectra generated based on the chirped-and-delay technique, coherent emission is visible up to $6\,\mathrm{THz}$. Broader spectra are generated by reducing the number of modulation periods in the laser pulse intensity modulation.

5.4.9 Two-color THz pulses

The linearity of the phase shift pattern allows to add up multiple phase shifts to create more complex pulses or pulse trains. In a first attempt, multiple different THz output frequencies were overlayed in the phase pattern, resulting in a two-color THz generation. Figure 5.16 shows a series of tow-colored spectra under variation of the spectral distane of the contributions.

Generating two narrowband spectra at a very close spectral distance has a high complexity η. Here, the limit is reached at a minimum distance of approximately $200\,\mathrm{GHz}$ (Fig. 5.16 (top)).

5.4.10 Further user-defined spectral shapes

Merging the phase shift patterns of several narrowband modulation patterns allows to generate further arbitrary spectral shapes. Empirically, a rectangular spectrum and a

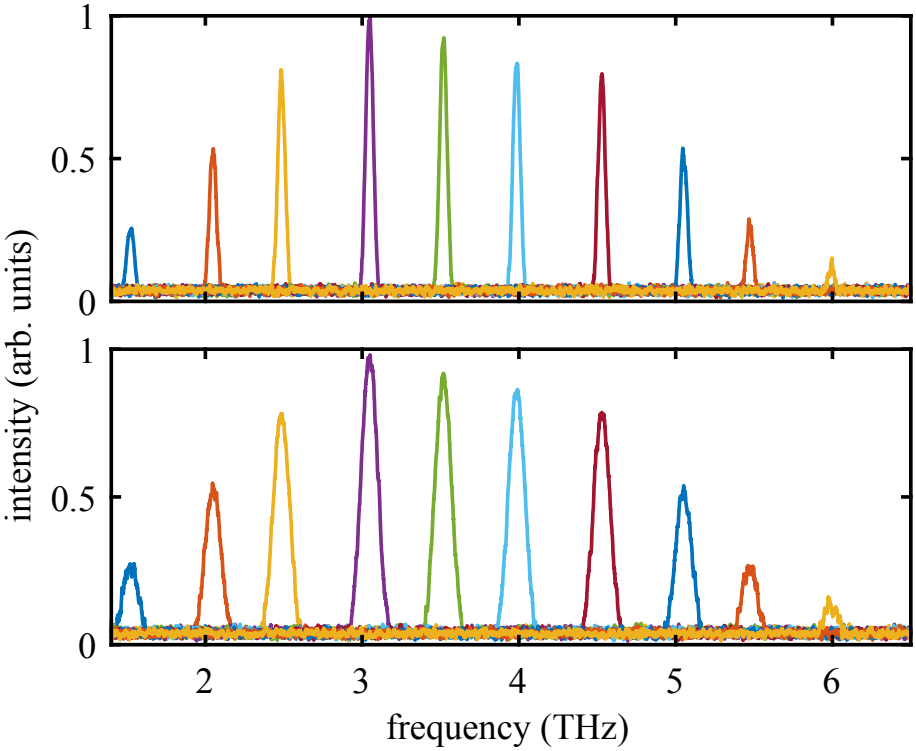

Figure 5.15: Spectra of narrowband THz radiation. The spectral phase of the laser pulse was corrected by the pulse shaper. A cancellation of the third-order dispersion was programmed. Different strength of the phase modulation, i.e. the maximum phase lead to a different number of pulse copies which allows for a user-defined spectral width.

trapezoidal spectral shape were generated by adding up phase patterns for narrowband modulation. Two examples are depicted in Fig. 5.17.

5.5 Comparison of shaping methods

In the previous sections, experimental setups for the temporal shaping of (ultra-)short laser pulses and results from THz generation experiments were described. The use of a Michelson interferometer enabled widely tunable THz radiation in the range from $50\,\mathrm{GHz}$ to approximately $6\,\mathrm{THz}$. Here, the influence of higher-order dispersion cannot be easily corrected, as the setup provides only one degree of freedom, namely the pulse delay. However, the components used in the interferometer have a high damage threshold, which, in principle, allows for scaling up the laser power. On the other hand, the interferometer reduces the efficiency of the shaping setup by a factor of two, since half of the laser power does not reach the experiment. The remaining laser pulse energy delivered to the storage ring was $3.5\,\mathrm{mJ}$. Comparing this value to the approximately

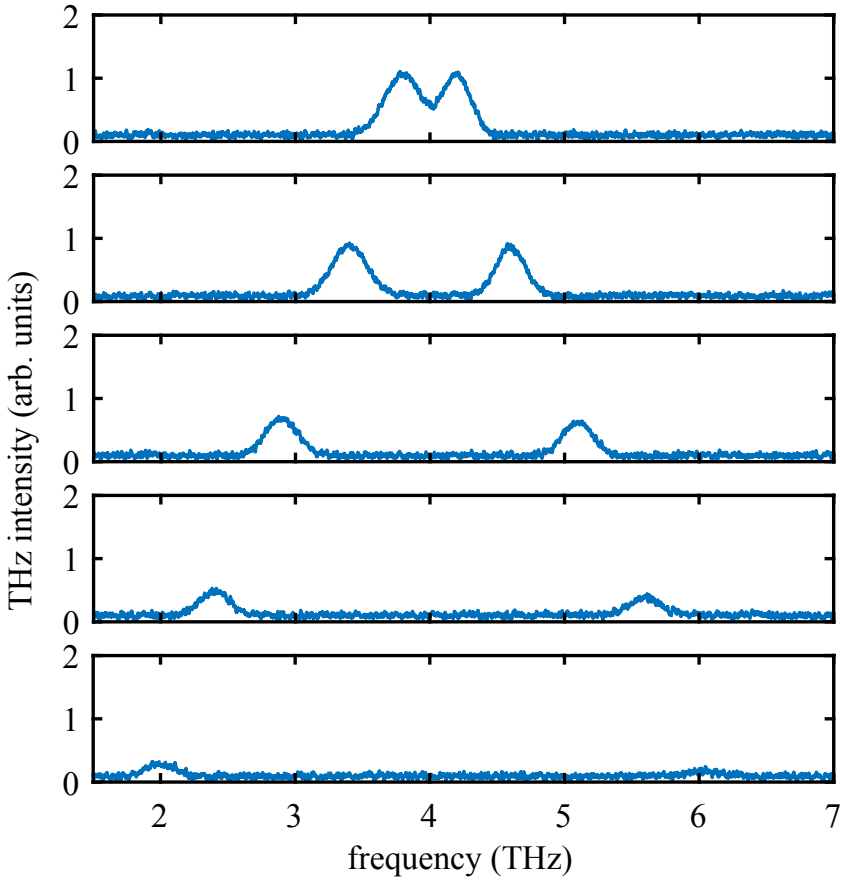

Figure 5.16: Series of two-color THz spectra with variable peak distance. Here, several phase filters are summed up and applied to the phase modulator to generate multiple controllable frequencies simultaneously.

$9.5\,\mathrm{mJ}$ before the laser pulse compressor and $8\,\mathrm{mJ}$ after the compressor, a significant portion of the laser pulse energy is lost.

Although the pulse shaper containing the SLM uses far fewer optical components compared to the interferometer, the output pulse energy is limited to about $1\,\mathrm{mJ}$ to prevent damage to the SLM. Higher pulse energies initially lead to fluctuations in diffraction efficiency, while permanent damage to the liquid crystal layer was observed at pulse energies exceeding $4\,\mathrm{mJ}$ for pulse durations of approximately $1\,\mathrm{ps}$. This presents two challenges: first, ablation due to the short pulse duration damages the mirror surface of the SLM, and second, the high average power burns the carrier substrate. Recent advancements in SLM technology offer potential solutions to these issues. One approach is the use of micro-mirror actuators (MEMS), which allow for higher peak and average power. Additionally, active cooling of SLMs could enhance their damage threshold beyond picosecond pulses with an average power of $200\,\mathrm{W}$ [189].

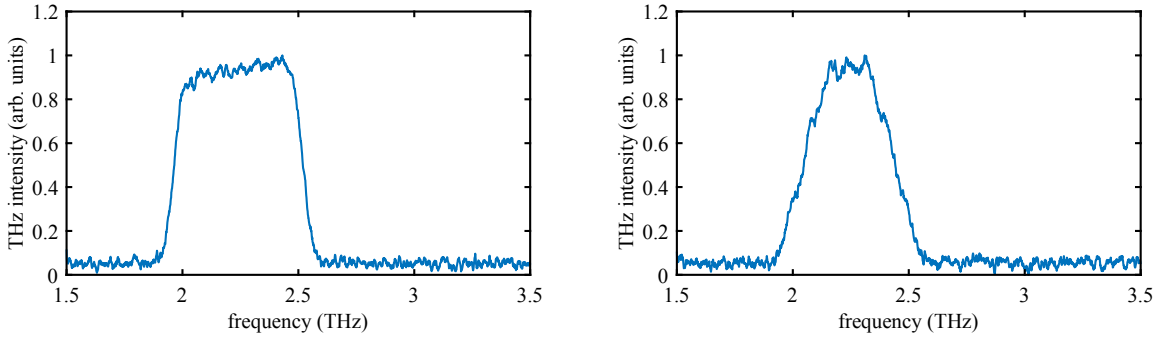

Figure 5.17: Rectangular spectral shape generated by superimposed filters on the SLM (left) and trapezoidal spectral shape (right).

The advent of adaptive optics has revolutionized the field of laser pulse shaping. With this technique now established in the laser community, applications in related fields, such as synchrotron radiation science, are emerging.

5.6 Applications

The pulse-shaping approaches make the THz beamline at DELTA an even more versatile tool. Changing the spectro-temporal behavior of a THz pulse allows to tailor pulses for applications where both is needed, control over timing and spectral properties.

5.6.1 Characterization of THz detection systems

As highlighted in Chap. 2, the diagnostics of radiation pulses emitted from short bunches is crucial for setting up accelerators that provide short pulses [190]. However, most available (sub-)THz detectors are not characterized under conditions comparable to their application in accelerators. Frequently, sensitivity measurements are performed using continuous-wave (CW) radiation, which differs significantly from pulsed operation in terms of the readout chain, including the antenna, detector, amplifier, and digitization.

Narrowband (sub-)THz radiation generated by the chirped-pulse beating technique was used to characterize various Schottky-barrier detectors manufactured by Virginia Diodes. The detectors exhibited narrowband sensitivity, determined by the antenna and the waveguide connecting the detector to the antenna.

Figure 5.18 presents measurements of the normalized responses of five detectors to (sub-)THz radiation generated by the chirped-pulse beating scheme. The Michelson

interferometer was supplemented with a piezo actuator, used to adjust the central frequency. The piezo was continuously moved, resulting in a linear frequency sweep over time. A total delay range of $400\,\mu m$ was scanned over approximately $5\,min$. In this setup, the frequency shift corresponds to $2.7\,GHz/\mu m$.

The resulting response curves represent convolutions of the THz generation gain curve, the spectral beamline transmission curve, and the spectral response of each detector. Calibrating these curves is challenging; however, the current setup offers a practical approach to characterizing the detectors under similar circumstances. The nominal sensitivity range ($3\,dB$ level) of each detector is provided in the legend of Fig. 5.18. Overall, the sensitivity spans from $90\,GHz$ to $750\,GHz$.

A Schottky-barrier detector manufactured by ACST was installed at a diagnostics beamline of the free-electron laser SwissFEL [191]. The accelerator employs two magnetic chicanes, referred to as bunch compressors (BC1 and BC2), to reduce the bunch length based on energy-dependent path lengths within the chicanes. The compression after BC1 is monitored by detecting radiation emitted from the fourth bending magnet of the bunch compressor. The observed spectral range is deliberately limited to the region where the intensity of coherent emission drops. For BC1, this corresponds to $25\,GHz$ to $250\,GHz$ [192]. The detector used is of the same type as the one employed for measurements in this thesis.

Due to the limited opportunities to access the detector at the beamline after installation, a test under similar conditions was required. This was particularly necessary to eval-

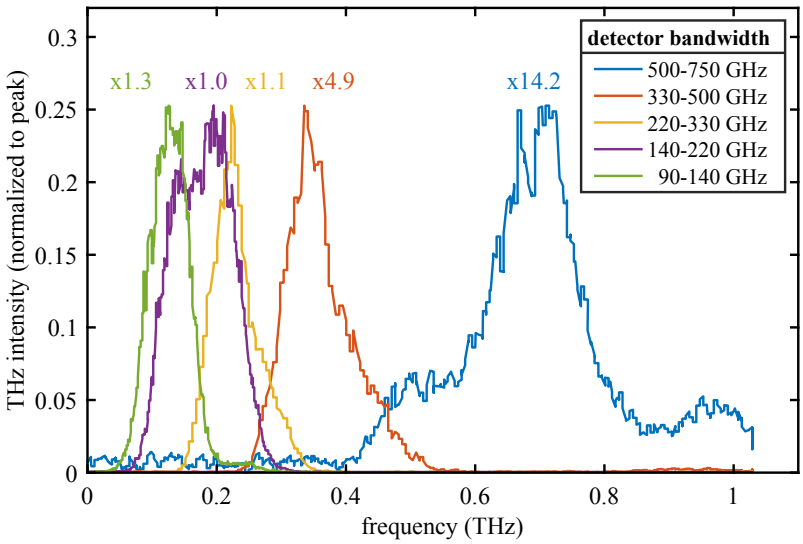

Figure 5.18: Detector responses of five narrowband Schottky-barrier detectors. The measured amplitude was aquired during sweeps of the central frequency of the (sub-)THz radiation to compare the sensitive range.

uate the timing characteristics, meaning a pulsed sub-THz source with a comparable spectrum was needed. As described in Chap. 2, the detector employs a log-spiral antenna to receive incident pulses. While log-spiral antennas generally exhibit only slight polarization dependence, the optimal antenna and detector orientation needed to be determined experimentally.

Before installation at SwissFEL, the detector was tested at the DELTA THz beamline, operated in the chirp-and-delay mode. The polarization angle of the incident radiation was varied from $0°$ to $350°$ in steps of $10°$, while the nominal central frequency was scanned from $0\,\mathrm{GHz}$ to $300\,\mathrm{GHz}$. To prevent optical coupling mismatches, the detector position was optimized for each setting. Figure 5.19 presents the results of the polarization-dependent frequency sweeps. The transverse size of the sub-THz beam is inversely proportional to the frequency (see Chap. 2). Consequently, low-frequency components cover a larger area of the antenna. Depending on the relative orientation of the field direction and the antenna spiral, the outermost sections of the antenna may contribute to signal reception. The correct detector assembly could be found using these experimental data.

5.6.2 Possible use cases in materials science and chemistry

Besides advancements in RF system engineering and accelerator diagnostics, there are also applications in materials science and chemistry. One example is the spectroscopy

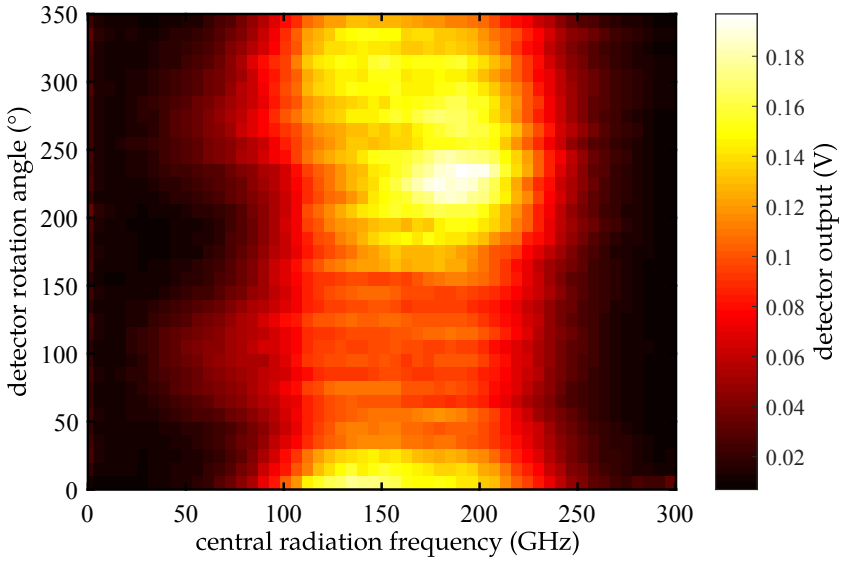

Figure 5.19: Frequency sweeps recorded with an ACST Schottky-barrier detector under variation of the incident polarization direction. Signals below $90\,\mathrm{GHz}$ are enhanced at certain, circular-symmetric angles.

of water. The absorption of THz radiation by water is of particular interest, as water is one of the most important solvents, specially for medical applications. However, its absorption characteristics are not yet fully understood [193]. Molecular dynamics simulations [194] suggest that different absorption mechanisms occur in water depending on the excitation frequency: Below $1\,\mathrm{THz}$, absorption is dominated by the reorientation of collective dipoles of multiple hydrogen-bonded water molecules [195]. Intermolecular translations, known as network stretching, cause absorption centered around $6\,\mathrm{THz}$. Additional absorption features due to librational modes are found at $10\,\mathrm{THz}$ and $20\,\mathrm{THz}$.

Considering the accessible frequency range at the DELTA THz beamline, parts of the regimes relevant for water spectroscopy are already covered. The pulse energy required to excite these modes is approximately $1\,\mu\mathrm{J}$. The currently achieved maximum pulse energy is about $200\,\mathrm{nJ}$, which is insufficient for nonlinear spectroscopy but could be applied for linear spectroscopy [194].

6 Studies of the longitudinal phase space

The previous chapters focused on the generation of THz radiation, particularly optimizing the radiation process. In the following sections, measurements related to the longitudinal phase space of the storage ring are presented, utilizing the laser-electron interaction.

6.1 Measurement of the longitudinal charge distribution

Since the generation of THz radiation relies on the interaction of the laser pulse with only a short slice of the electron bunch, a successive temporal shift of the laser pulse allows for sampling the electron distribution for each RF bucket. Figure 6.1 presents a typical measurement of the storage ring fill pattern, acquired with a direct-current current transformer (DCCT) [129] (red curve).

Typically, no measurable THz signal is detected when the laser-electron interaction is set up in multibunch mode, as the number of modulated electrons is too small. However, it was observed that the chirped-pulse beating (CPB) scheme enables the emission by modulating a larger number of electrons due to the extended laser pulse duration. Additionally, the THz frequency can be tuned to the sensitivity maximum of the Schottky diode detector. These optimizations lead to a measurable THz intensity in multibunch mode.

The normalized square root of the THz signal is shown in blue. The square root is plotted because the THz signal scales with the square of the number of modulated electrons due to the longitudinal coherence. The THz signal pattern closely follows the DCCT measurement, demonstrating that bunch charges as low as $10\,\mathrm{pC}$ are sufficient to generate coherent THz pulses detectable with room-temperature Schottky diode detectors.

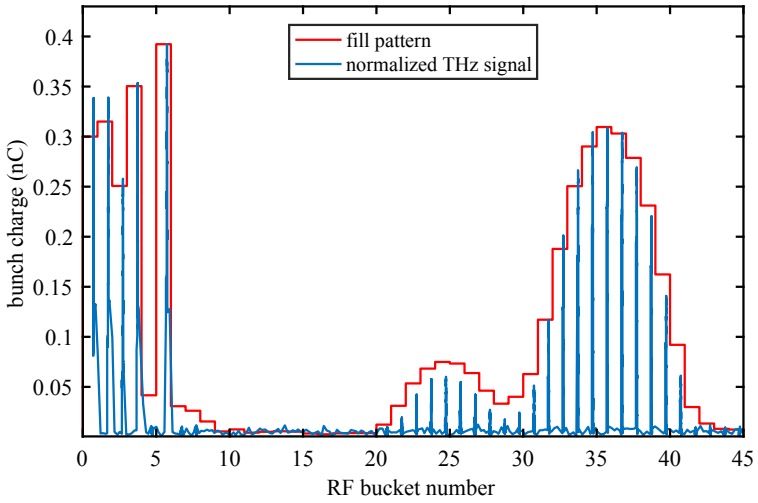

Figure 6.1: During multibunch operation, the beam current is measured using a direct-current current transformer (DCCT). In multibunch mode, the typical charge in a single RF bucket is too low to generate a detectable THz signal. However, by employing the chirped-pulse beating (CPB) scheme, the THz signal was enhanced by modulating a larger number of electrons and tuning the output frequency to the Schottky detector's peak sensitivity range.

6.2 Observation of the longitudinal phase space motion

As pointed out in Chap. 2, the synchrotron oscillation describes the motion of off-momentum electrons in the longitudinal phase space. The momentum deviation induced by a laser-electron interaction thus leads to a rotation in phase space, too. Figure 6.2 [196] shows the evaluation of an `elegant` simulation of the turn-by-turn evolution of the energy-modulated electrons. The oscillation in the longitudinal phase space can be observed. Due to the movement of the energy-modulated electrons off the bunch center, a longitudinal density dip has formed in the bunch center, giving rise to emission of coherent THz radiation. The motion in phase space however causes that this density dip occurs only at distinct phases of the synchrotron oscillation, i.e. after half an oscillation period.

After half a synchrotron oscillation period the density modulation caused by the laser interaction has turned by 180° in the longitudinal phase space (cf. Fig 2.3). The electron density comprises a dip which reoccurs every integer multiple of $T_s/2$. Since the synchrotron radiation spectrum depends on the Fourier transform of the longitudinal charge distribution, THz pulses emitted over multiple turns arise delayed by $T_s/2$. Figure 6.3 shows the simulated spectral evolution of the pulses over time. Each vertical slice corresponds to a simulated false-color emission spectrum of the respective revolution. The simulation was performed first with the higher-order-mode damped cavity

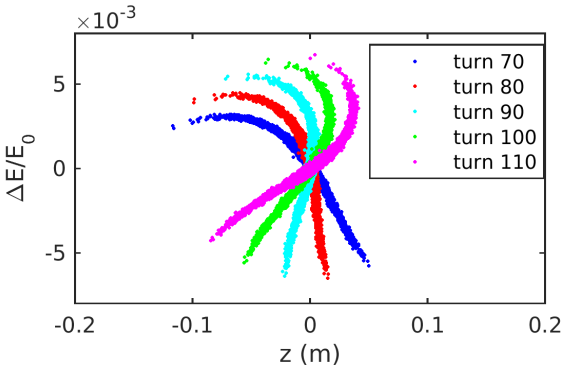

Figure 6.2: Simulation of the longitudinal motion of energy modulated electrons 70 to 110 turns after the initial laser-electron interaction.

being deactivated. The synchrotron oscillation period in this case equals 75 turns. The simulation shows that during the first half of the synchrotron oscillation period the central THz emission frequency shifts downwards for about 40 turns and increases again after a total of about 75 turns.

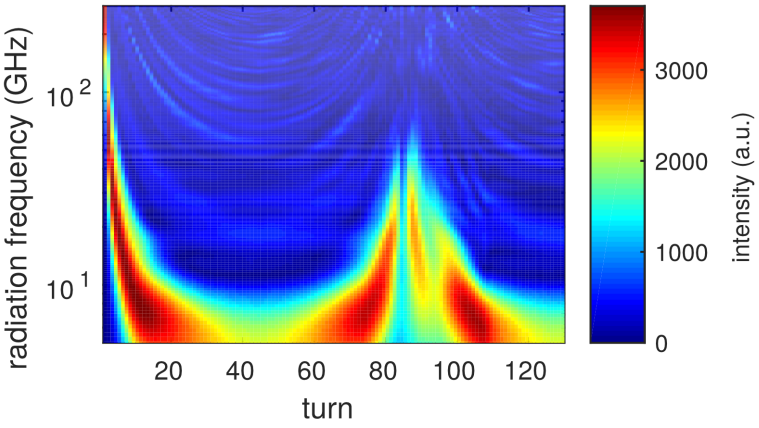

Figure 6.3: Simulated turn-by-turn evolution of THz spectra over 130 turns.

6.2.1 Influence of the RF upgrade in 2019

In autumn 2019, an additional RF system was installed. Besides the DESY-type cavity, the EU higher-order-mode damped cavity is now in operation (cf. Chap. 3). The larger total RF voltage leads to a higher synchrotron oscillation frequency and therefore reduces the repetition period after which the THz signal reoccurs. The synchrotron oscillation frequency can be measured through the data acquisition of a fast bunch-by-bunch feedback system or an RF spectrum analyzer in the DELTA control room. Applying an

RF voltage of $390\,\mathrm{kV}$ to each cavity leads to a synchrotron oscillation frequency of $22\,\mathrm{kHz}$ being equivalent to an oscillation period of $45.5\,\mu\mathrm{s}$.

Figure 6.4 shows a simulation of the central frequency as function of the revolution after the laser-electron interaction. A periodic reoccurence of the central frequency towards about $60\,\mathrm{GHz}$ is visible with a period of half the synchrotron tune.

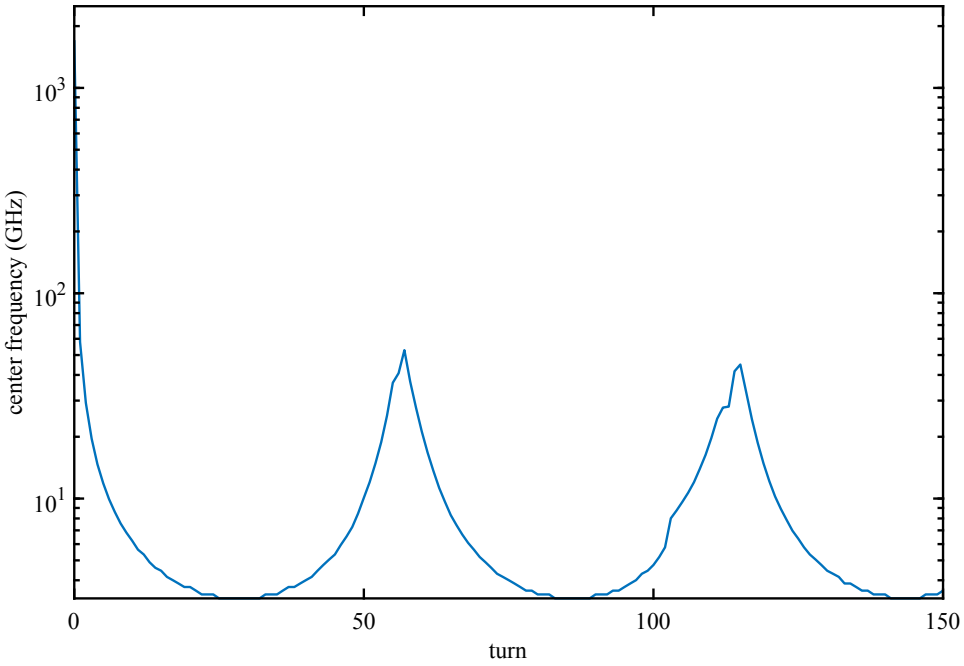

Figure 6.4: Simulation of the central THz emission frequency as function of the turn number after the initial laser electron interaction.

Convolving the spectral response of the Schottky-barrier detector with the simulated spectra gives a simulated response of the Schottky detector which is depicted in Fig. 6.5. Here, it is visible that each „echo" of the coherent pulse train is shortly interrupted because the dip in the longitudinal electron density shortly vanishes due to the phase space rotation.

The shorter oscillation period makes it easier to observe more echos of the energy modulated signals also in the measurement. Figure 6.6 shows a measurement (blue) of the laser-induced THz signal. The measurement was conducted using a 12-bit, 8-GHz real-time oscilloscope[1] with a sampling rate of $20\,\mathrm{GS/s}$. Acquisition over a signal amplitude of 5 decades ($3\,\mu\mathrm{V}$ to $300\,\mathrm{mV}$) was possible by combination of successive datasets with different input gain settings. A calibration of the individual gain settings was done before. The resulting measurements show that the THz signal reoccurs about every 55 revolutions. Between the pulse trains, the noise floor is about $20\,\mu\mathrm{V}$. The sensitivity of

[1] Teledyne LeCroy WavePro 804HD

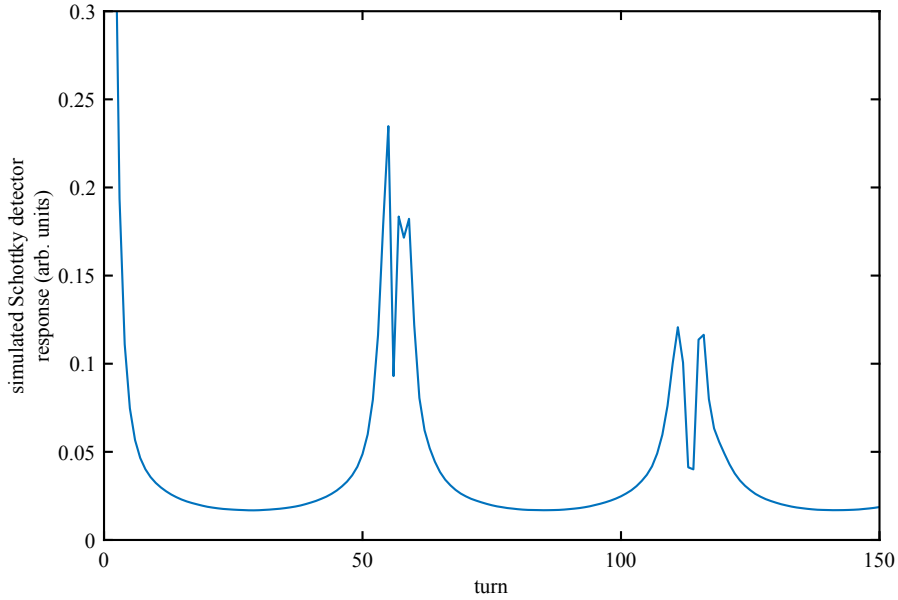

Figure 6.5: Simulated response to THz signals from 150 turns. The THz emission from simulated electron bunches was folded with the known spectral sensitivity of the Schottky diode detector to estimate the signal.

the measurement was further improved by using the arrival time of the THz pulse in the analysis (orange curve). While the blue curve shows the raw measurement, the gated-THz detection selects only these data points which occur at a timing which matches the expected arrival time of a synchrotron light pulse. A similarly narrowband measurement could be realized by using a multi-MHz Lock-In amplifier, but such a device was not available.

The measurement shows that a residual energy modulation is observable for about 400 revolutions after the initial laser-electron interaction. Given that a laser-electron interaction occurs every 2603 revolutions, coherent emission appears during a significant fraction of time. The laser system used for the energy modulation features the possibility to increase the repetition rate from $1\,\mathrm{kHz}$ to $5\,\mathrm{kHz}$ at the cost of peak laser intensity. Still, in this case, coherent emission could be expected with a duty cycle of approximately $80\,\%$.

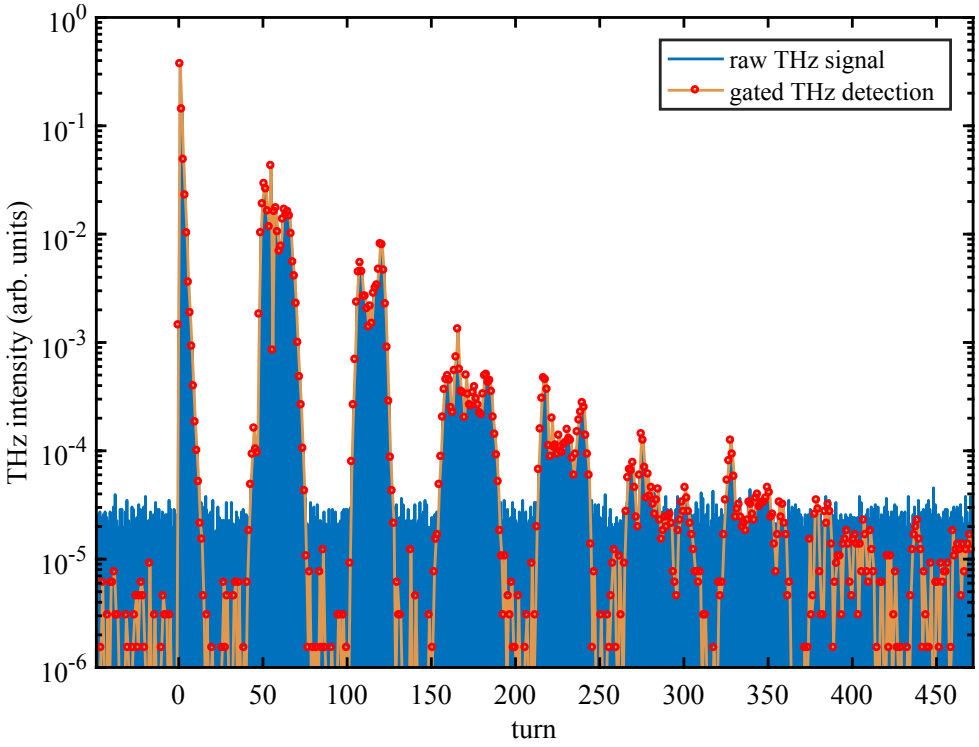

Figure 6.6: Measurement of THz signals from many turns after the initial laser-electron interaction. The signal was detected by the Schottky-barrier diode. To increase the dynamic range the sensitivity of the readout oscilloscope was adapted during the measurement and the combined data are shown.

7 Conclusion & Outlook

Within this thesis, significant enhancements to the THz source at DELTA were implemented. Previously, the THz beamline operated exclusively in a broadband mode. Various approaches to achieving greater control over the THz generation process were developed and studied in detail. Additionally, diagnostic tools for analyzing both the generated THz pulses and the laser pulses were successfully implemented.

7.1 Diagnostics

Before improvements to the spectro-temporal shaping of laser and THz radiation could be realized, an adapted set of diagnostics was designed and commissioned. A laser intensity autocorrelator was built, which provides a very good measurement stability and reliability despite the ambiguities of autocorrelation.

The THz pulses produced at the short-pulse facility of DELTA cover a wide frequency range from about $50\,\mathrm{GHz}$ to $6\,\mathrm{THz}$. While a commercial spectrometer already allowed measurements of the pulses at frequencies larger than $1\,\mathrm{THz}$, additional diagnostics were needed for the sub-THz range. The spectrometer was successfully commissioned and used for the diagnostics of THz pulses. The ability to gate the detector, which can be a silicon bolometer or a Schottky barrier detector, allows for the observation of the temporal evolution of the THz pulses in the spectral domain. Here, in particular, the observation of coherently emitted pulses after half a synchrotron oscillation period and a full oscillation period was studied.

7.2 Pulse shaping

The shaping of laser pulses to influence the coherent emission of THz radiation was successfully studied and realized in a stepwise approach. First, the influence of the laser pulse length was used to shift the broadband THz spectrum. Here, within a certain range from $2\,\mathrm{THz}$ to $3\,\mathrm{THz}$, the centroid of the spectrum was controlled. As many

applications demand better control of the spectrum, an experiment was conducted to generate two THz pulses emitted from the same bunch. The technical challenge was to achieve a stable twofold interaction with the electron bunch approximately $20\,\mathrm{m}$ away from the laser setup. The interference of two THz pulses at a short distance on the millimeter scale led to a broadband spectrum with interference fringes comparable to a frequency comb. Hence, this was a successful implementation of an emission mode offering narrowband spectral features.

In the next step, not only was spectral control improved, but also the emission power. To imprint a THz-frequency intensity modulation on a laser pulse, chirped laser pulses with picosecond duration were generated using a Michelson interferometer. The central frequency of the resulting THz emission was fully tunable via the DELTA control system.

To gain almost full control over the spectro-temporal properties of laser pulses, a programmable pulse shaper was designed and commissioned. The spectral bandwidth of narrowband THz radiation was improved from a relative bandwidth of $10\,\%$ to less than $2\,\%$.

However, the laser pulse energy is limited by the pulse-shaping setup used in this thesis. To address this problem, static, non-adjustable phase pattern glass masks could be designed and manufactured for high-power applications. Lithographic techniques allow for the precise fabrication of phase-shift masks [197], which can withstand high-power laser radiation. A possible approach would be to first design and test the correct phase pattern using the spatial light modulator and then implement this pattern on a static phase mask. Of course, this would come at the cost of flexibility, as the spatial light modulator enables dynamic, computer-controlled optimization.

7.3 Future improvements

7.3.1 Diagnostics

So far, phase-insensitive diagnostics has been used to study the properties of the electron energy modulation. A setup for the coherent measurement of the electron distribution using so-called electro-optic diagnostics would further improve the pulse diagnostics. Here, the interaction of the electric field of the THz pulse or the Coulomb field of the electron bunch is used to modulate a short laser pulse from an Ytterbium (Yb) laser in an electro-optic crystal like gallium phosphide [198], which is then diagnosed using ultrafast detectors [199, 200]. Besides providing an even better understanding

of the longitudinal beam dynamics of the storage ring, it would also allow for precise measurement of the THz pulse energy, as the influence of the electric field on the THz pulse energy can be absolutely calibrated.

7.3.2 Frequency range and further scientific applications

The dispersive properties of the storage ring (cf. Chap. 2) and the spectro-temporal properties of the laser pulse define the THz radiation frequency at the DELTA short-pulse facility. Ongoing studies have allowed for a shortening of the electron bunch duration to approximately $60\,\mathrm{ps}$ (FWHM) [201]. The storage ring optics used here potentially enable an increase in the upper limit of the THz emission range to about $10\,\mathrm{THz}$, while the lower bound remains unchanged. This would enlarge the frequency range further to a regime which would be interesting for spectroscopic studies of solvents allowing for further scientific applications of the THz radiation.

A Appendix

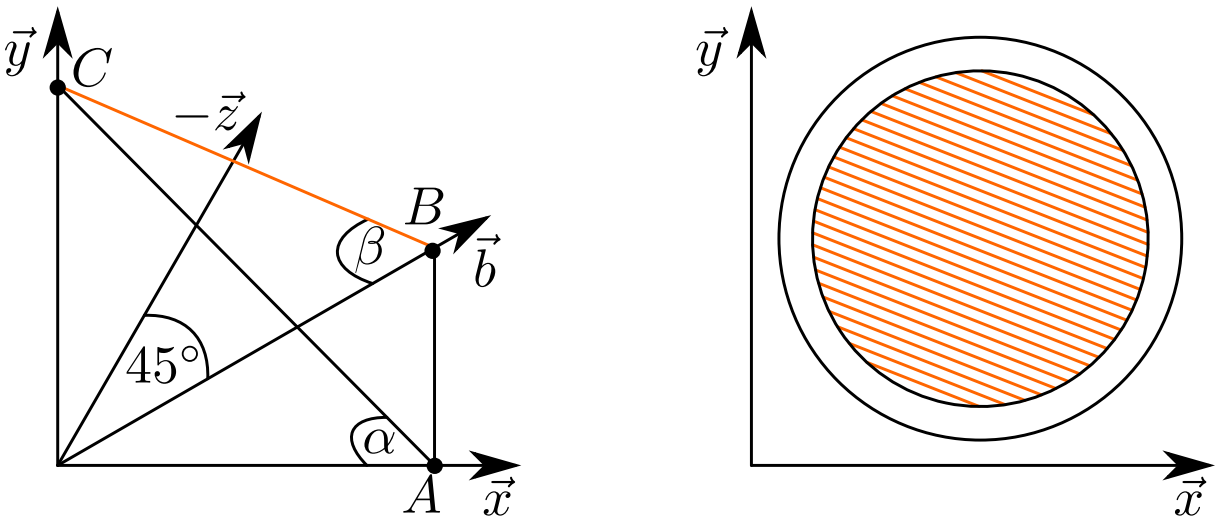

Figure A.1: Correct setup of the wire grid orientation.

The interferometer described in Chapter 4 uses partially reflecting polarizers to split the THz beam. Figure A.1 shows the correct orientation of the wire grid used as a beam splitter. Here, the THz beam enters perpendicularly to the $\vec{x}, \vec{y}$ plane, while the beam splitter is rotated by $45°$ about the $\vec{y}$ axis.

The coordinates are

$$A = \begin{pmatrix} 1 \\ 0 \\ 0 \end{pmatrix}, \quad B = \begin{pmatrix} 1 \\ 0 \\ -1 \end{pmatrix} \quad \text{and because } \alpha \stackrel{!}{=} 45° \quad C = \begin{pmatrix} 0 \\ 1 \\ 0 \end{pmatrix}, \tag{A.1}$$

which leads to

$$\beta = \arccos\left(\frac{\vec{BO} \cdot \vec{BC}}{|\vec{BO}| \cdot |\vec{BC}|}\right) = \arccos\left(\frac{\sqrt{2}}{\sqrt{3}}\right) \approx 35.3° \tag{A.2}$$

List of components

The components of the experimental setups built and used in this thesis are listed in the tables below.

A.1 Schottky-barrier detector

Component	**Type**	**Manufacturer**
Schottky barrier detector	2DL 12C LS 1200 A2 frequency range $50\,\mathrm{GHz}$ to $1.2\,\mathrm{THz}$ internal amplifier bandwidth $4\,\mathrm{GHz}$	ACST GmbH
RF adapter SMA to K-type	PE91009 SMA female to $2.92\,\mathrm{mm}$ male adapter	Pasternack Enterprises

A.2 Silicon bolometer

Component	**Type**	**Manufacturer**
Silicon Bolometer	HDL 5	Infralabs
Dewar	4.2 K Dewar	
Amplifier	LN-6C Low noise amplifier	

A.3 YBCO detector

Component	Type	Manufacturer
Detector	Yttrium barium copper oxide	KIT / Supracon
Wideband amplifier	SHF 804 TL	SHF AG
Bias tee	SHF BT65-B	SHF AG
RF cable	TCF219TTL1500 67 GHz bandwidth, 1.85-mm connector (V-type)	Totoku Electric

A.4 Martin-Puplett interferometer

Component	Type	Manufacturer
Polarizer	GS357206 100 mm clear aperture 5 µm wire, 12.5 µm period	Specac
Alignment beamsplitter	EBS2 2″ diameter	Thorlabs
Fast sampler	SR255	Stanford Research
Integrator mainframe	SR280	Stanford Research
Delay generator	DG645	Stanford Research
Toroidal mirrors	custom made	LTUltra
Translation stage	LSQ150D-E01T3 travel: 150 mm	Zaber Technologies

A.5 Autocorrelator

Component	Type	Manufacturer
Photodiode	PDA25K2 $150\,\mathrm{nm} - 550\,\mathrm{nm}$ $9.5\,\mathrm{MHz}$ bandwidth $2.2\,\mathrm{mm} \times 2.2\,\mathrm{mm}$	Thorlabs
Spectrometer	HR4000CG-UV-NIR spectral range: $200\,\mathrm{nm} - 1100\,\mathrm{nm}$	Ocean Optics
Corner-cube reflector	#49-674 $2''$, tolerance: $1\,\mathrm{arcsec}$, gold coated	Edmund Optics
BBO crystal	90015087 $5\,\mathrm{mm} \times 5\,\mathrm{mm} \times 0.2\,\mathrm{mm}$, $\Theta = 29°$	Newport
Beam splitter	BS1-800-50-2025-45P reflectivity: $(50 \pm 5)\,\%$ angle of incidence: $45°$, non-polarizing	CVI Melles Griot
Translation stage	M-ILS200CCL $200\,\mathrm{mm}$, accuracy: $1\,\mu\mathrm{m}$	Newport

A.6 Michelson interferometer

Component	Type	Manufacturer
Linear stage	M-462-X-SD UTRAlign travel: $25\,\mathrm{mm}$, crossed-roller bearing angular deviation < $100\,\mu\mathrm{rad}$	Newport
Motorized linear actuator	NSA12V6 travel: $11\,\mathrm{mm}$, min. step: $0.2\,\mu\mathrm{m}$	Newport
Piezo positioner	PX 400 travel:$400\,\mu\mathrm{m}$ resolution (closed-loop): $6\,\mathrm{nm}$	Piezosystem Jena
Distance sensor	GT2-H12K range: $12\,\mathrm{mm}$, resolution: $0.1\,\mu\mathrm{m}$	Keyence
Beam splitter	BS1-800-50-2025-45P reflectivity: $(50 \pm 5)\,\%$ angle of incidence: $45°$, non-polarizing	CVI Melles Griot
Delay-line mount	9848-KT	Newport

A.7 Laser pulse shaper

Component	Type	Manufacturer
Spatial light modulator	PLUTO 2 1920×1080 pixels	Holoeye AG
Controller	Raspberry Pi 4B	Broadcom
Gratings	Compression grating No. 715.706.940 grating constant: $1500\,\mathrm{mm}^{-1}$ size: $110\,\mathrm{mm} \times 50\,\mathrm{mm}$	Spectrogon
Grating mount	DGM-1	Newport
Cylindrical lens	LJ4878 $f = 75\,\mathrm{mm}$	Thorlabs

Bibliography

[1] T. H. Maiman, *Stimulated Optical Radiation in Ruby*, Nature 187, 493 (1960).

[2] P. A. Franken, *Generation of optical Harmonics*, Phys. Rev. Lett. 7, 118 (1961).

[3] P. F. Moulton, *Ti-doped Sapphire: Tunable Solid-state Laser*, Optics News 8, 9 (1982).

[4] D. Strickland, G. Mourou, *Compression of amplified chirped optical pulses*, Opt. Commun. 55, 447 (1985).

[5] R. Widerœ, *Über ein neues Prinzip zur Herstellung hoher Spannungen*, Archiv für Elektrotechnik 21, 387 (1928).

[6] D. W. Lynch, *Tantalus, a 240 MeV Dedicated Source of Synchrotron Radiation, 1968–1986*, J. Synchrotron Radiat. 4, 334 (1997).

[7] D. Iwanenko and I. Pomeranchuk, *On the Maximal Energy Attainable in a Betatron*, Phys. Rev. 65, 343 (1944).

[8] A. McPherson et al., *Studies of multiphoton production of vacuum-ultraviolet radiation in the rare gases*, J. Opt. Soc. Am. B 4, 595 (1987).

[9] M. Ferray et al., *Multiple-harmonic conversion of 1064 nm radiation in rare gases*, J. Phys. B 21, L31 (1988).

[10] M. Lewenstein et al., *Theory of high-harmonic generation by low-frequency laser fields*, Phys. Rev. A 49, 2117 (1994).

[11] J. Seres et al., *Source of coherent kiloelectronvolt X-rays*, Nature 433, 596 (2005).

[12] B. Zaks, R. B. Liu and M. S. Sherwin, *Experimental observation of electron-hole recollisions*, Nature 483, 580 (2012).

[13] R. S. Knox, *Introduction to Exciton Physics* in *Collective Excitations in Solids* ed. by B. Di Bartolo, Plenum Press, 1983.

[14] M. Kira et al., *Exciton Formation in Semiconductors and the Influence of a Photonic Environment*, Phys. Rev. Lett. 87, 176401 (2001).

[15] D. Golde, T. Meier and S. W. Koch, *High harmonics generated in semiconductor nanostructures by the coupled dynamics of optical inter- and intraband excitations*, Phys. Rev.

B 77, 075330 (2008).

[16] G. Ramian, *The new UCSB free-electron lasers*, Nucl. Instrum. Methods Phys. Res. A 318, 225 (1992).

[17] G. R. Neil, *Accelerator Sources for THz Science: A Review*, J. Infrared Millim. Terahertz Waves 35, 5 (2014).

[18] J. M. Ortega, F. Glotin and R. Prazeres, *Extension in far-infrared of the CLIO free-electron laser*, Infrared Phys. Technol. 49, 133 (2006).

[19] D. Oepts, A. F. G. van der Meer, P. W. van Amersfoort, *The free-electron laser user-facility FELIX*, Infrared Phys. Technol. 36, 297 (1995).

[20] U. Lehnert et al., *First experiences with the FIR-FEL at ELBE*, in Proc. of FEL Conference 2007, Novosibirsk, Russia, 97.

[21] W. Schöllkopf et al., *The new IR and THz FEL facility at the Fritz Haber Institute in Berlin*, Advances in X-ray Free Electron Lasers Intrumentation III, 95121 (2015).

[22] N. A. Vinokurov et al., *Status of the Novosibirsk high power terahertz FEL*, in Proc. of FEL Conference 2006, Berlin, Germany, 492.

[23] Y. U. Jeong et al., *First lasing of KAERI compact far-infrared free-electron laser driven by a magnetron-based microtron*, Nucl. Instrum. Methods Phys. Res. A 475, 47 (2001).

[24] G. Isoyama et al., *Development of FEL and SASE in the far-infrared region at ISIR, Osaka University*, Infrared Phys. Technol. 51, 371 (2008).

[25] Y. J. Ding, *Progress in terahertz sources based on difference-frequency generation*, J. Opt. Soc. Am. B 31, 2696 (2014).

[26] S. Khan et al., *Generation of Ultrashort and Coherent Synchrotron Radiation Pulses at DELTA*, Synchrotron Radiation News 26, 25 (2013).

[27] P. A. Zyla et al. (Particle Data Group), Prog. Theor. Exp. Phys. 2020, 083C01.

[28] `http://www.lightsources.org` [accessed April 4, 2021].

[29] K. Wille, *The Physics of Particle Accelerators: An Introduction*, Oxford University Press (2000).

[30] H. Wiedemann, *Particle Accelerator Physics*, Springer (2015).

[31] J. A. Serret, *Sur quelques formules relatives à la théorie des courbes à double courbure*, J. Math. Pures Appl. 16, 193 (1851).

[32] F. Frenet, *Sur les courbes à double courbure*, J. Math. Pures Appl. 17, 437 (1852).

[33] A. W. Chao, *Physics of Collective Beam Instabilities in High Energy Accelerators*, Wiley (1993).

[34] S. Khan, *Collective Phenomena in Synchrotron Radiation Sources*, Springer (2006).

[35] W. Magnus, S. Winkler, *Hill's equation*, Dover Publications Inc. (1979).

[36] G. W. Hill, *On the Part of the Motion of Lunar Perigee Which is a Function of the Mean Motions of the Sun and Moon*, Acta Math. 8, 1 (1886).

[37] E. D. Courant, H. S. Snyder, *Theory of the Alternating-Gradient Synchrotron*, Annals of Physics 3, 1 (1958).

[38] D. W. Kerst, R. Serber, *Electronic Orbits in the Induction Accelerator*, Phys. Rev. 60, 53 (1941).

[39] N. M. Blachmann and E. D. Courant. *The Dynamics of a Synchrotron with Straight Sections*, Rev. Sci. Inst. 20, 596 (1949).

[40] J. Feikes et al., *Sub-picosecond electron bunches in the BESSY storage ring*, Proc. of EPAC2004, Lucerne, Switzerland, 1954.

[41] M.-A. Tordeux et al., *Low-alpha operation for the SOLEIL storage ring*, Proc. of IPAC2012, New Orleans, Louisiana, USA, 1608.

[42] A.-S. Müller et al., *Far infrared coherent synchrotron edge radiation at ANKA*, Proc. of PAC2005, Knoxville, Tenesse, USA, 2518.

[43] F. Zimmermann, M. G. Minty, *Measurement and Control of Charged Particle Beams*, Springer (2003).

[44] M. Ries, *Nonlinear momentum compaction and coherent synchrotron radiation at the Metrology Light Source*, doctoral thesis, Humboldt-Universität zu Berlin (2014).

[45] P. Schreiber et al., *Status of operation with negative momentum compaction at KARA*, Proc. of IPAC2019, Melbourne, Australia, 878.

[46] J. D. Jackson, *Classical Electrodynamics*, John Wiley & Sons (1998).

[47] T. Shintake, *Real-time animation of synchrotron radiation*, Nucl. Instrum. Methods Phys. Res. A 507, 89 (2003).

[48] T. Shintake, *Radiation2D*, `https://groups.oist.jp/qwmu/software` [accessed April 4, 2021].

[49] W. Herschel, *Experiments on the Refrangibility of the invisible Rays of the Sun*, Phil. Trans. R. Soc. 90, 284 (1800).

[50] E. F. Nichols, *A study of the transmission of certain substances in the infrared*, Phys. Rev. 1, 1 (1893).

[51] J. C. Maxwell, *A Dynamical Theory of the Electromagnetic Field*, Phil. Trans. (155), 459 (1865).

[52] H. Hertz, *Ueber sehr schnelle electrische Schwingungen*, Annalen der Physik 267, 421 (1887).

[53] E. Bründermann, H.-W. Hübers and M. F. Kimmitt, *Terahertz Techniques*, Springer (2012).

[54] M. Planck, *Zur Theorie des Gesetzes der Energieverteilung im Normalspectrum*, Annalen der Physik 309, 553 (1901).

[55] E. K. Plyler et al., *Radiant energy from sources in the far infrared*, J. Opt. Soc. Am. 52, 859 (1962).

[56] J. Neu and C. A. Schmuttenmaer, *Tutorial: An introduction to terahertz time domain spectroscopy (THz TDS)*, J. Appl. Phys 124, 231101 (2018).

[57] M. Brosi et al., *Fast mapping of terahertz bursting thresholds and characteristics at synchrotron light sources*, Phys. Rev. Accel. Beams 19, 110701 (2016).

[58] H. A. Zahl, M. J. E. Golay, *Pneumatic heat detector*, Rev. Sci. Instrum 17, 511 (1946).

[59] M. J. E. Golay, *A pneumatic infra-red detector*, Rev. Sci. Instrum. 18, 357 (1947).

[60] J. A. Valdmanis, G. Mourou and C. W. Gabel, *Picosecond electrooptic sampling system*, Appl. Phys. Lett. 41, 211 (1982).

[61] I. Wilke et al., *Single-shot electron-beam bunch length measurements*, Phys. Rev. Lett. 88, 124801 (2002).

[62] R. Niemczyk, *Konstruktion eines Aufbaus für elektrooptische Fernfeld-Messungen an der Terahertz-Strahllinie bei DELTA*, master's thesis, TU Dortmund University (2017).

[63] B. Sawadski, *Elektrooptische Strahldiagnose an der Kurzpulsquelle bei DELTA*, master's thesis, TU Dortmund University (2018).

[64] N. Hiller, *Electro-Optical Bunch Length Measurements at the ANKA Storage Ring*, doctoral thesis, Karlsruher Institut für Technologie (2013).

[65] B. Steffen, *Electro-Optic Methods for Longitudinal Bunch Diagnostics at FLASH*, doctoral thesis, Universität Hamburg (2007).

[66] E. Hausmann et al., *Radio phone receiving: A practical handbook for everybody*, D. van Nostrand Company (1922).

[67] R. F. Pierret, *Semiconductor device fundamentals*, Addison-Wesley (1996).

[68] O. Cojocari, *Schottky structures for THz applications based on quasi-vertical design concept*, Proc. of Int. Symp. of Space THz Technology 2005, 490.

[69] M. Laabs et al., *On-chip THz spectrometer for bunch compression fingerprinting at fourth-generation light sources*, J. Synchrotron Radiat. 25, 1509 (2018).

[70] J. Dyson, *The Equiangular Spiral Antenna*, IEEE Trans. Antennas Propag. 7, 181 (1959).

[71] M. Maury, *Microwave coaxial connector technology: A continuing evolution*, Microwave Journal 12/05, 14 (2005).

[72] P. Thoma, *Ultra-fast $YBa_2Cu_3O_{7-x}$ direct detectors for the THz frequency range*, doctoral thesis, Karlsruher Institut für Technologie (2013).

[73] J. Raasch, *Electrical-field sensitive $YBa_2Cu_3O_{7-x}$ detectors for real-time monitoring of picosecond THz pulses*, doctoral thesis, Karlsruher Institut für Technologie (2017).

[74] T. S. Ross, *Laser Beam Quality Metrics*, SPIE Press (2013).

[75] H. Kogelnik and T. Li, *Laser Beams and Resonators*, Appl. Opt. 5, 1550 (1966).

[76] V. E. Rogalin, I. A. Kaplunov and G. I. Kropotov, *Optical materials for the THz range*, Opt. Spectrosc. 125, 1053 (2018).

[77] J. Dai et al., *Terahertz time-domain spectroscopy characterization of the far-infrared absorption and index of refraction of high-resistivity, float-zone silicon*, J. Opt. Soc. Am. B 21, 1379 (2004).

[78] J. B. Shapiro and E. E. Bloemhof, *Fabrication of wire-grid polarizers and dependence of submillimeter-wave optical performance on pitch uniformity*, Int. J. Infrared Millim. Waves 11, 973 (1990).

[79] K. Jacob, M. Kotiranta, *Transmission and Reflection Characterization of Polarizing Beam Splitters at Submillimeter Wavelengths*, IEEE Trans. Terahertz Sci. Technol. 9, 272 (2019).

[80] W. G. Chambers, A. E. Costley and T. J. Parker, *Characteristic curves for the spectroscopic performance of free-standing wire grids at millimeter and submillimeter wavelengths*, I. J. Infrared Millim. Waves 9, 157 (1988).

[81] W. G. Chambers et al., *Theory of the scattering of electromagnetic waves by a regular grid of parallel cylindrical wires with circular cross section* , J. Phys. A 13, 1433 (1980).

[82] P. F. Moulton, *Spectroscopic and laser characteristics of Ti:Al_2O_3*, J. Opt. Soc. Am. B 3, 125 (1985).

[83] H. W. Mocker, R. J. Collins, *Mode Competition and self-locking in a Q-switched Ruby Laser*, Appl. Phys. Lett. 7, 270 (1965).

[84] H. A. Haus, *Theory of mode locking with a fast saturable absorber*, Appl. Phys. 46, 3049 (1975).

[85] A. M. Weiner, *Femtosecond pulse shaping using spatial light modulators*, Rev. Sci. Instrum. 71, 1929 (2000).

[86] S. H. Shim et al., *Femtosecond pulse shaping directly in the mid IR using acousto-optic modulation*, Opt. Lett. 31, 838 (2006).

[87] K. Sala, G. Kenney-Wallace and G. Hall, *CW autocorrelation measurements of picosecond laser pulses*, IEEE J. Quantum Electron. 16, 990 (1980).

[88] Jean-Claude M. Diel, *Control and measurement of ultrashort pulse shapes (in amplitude and phase) with femtosecond accuracy*, Appl. Opt. 24, 1270 (1985).

[89] R. W. Boyd, *Nonlinear optics*, Academic Press (2008).

[90] D. Kane, *Recent progress toward real-time measurement of ultrashort laser pulses*, IEEE J. Quantum Electron. 35, 421 (1999).

[91] R. Trebino, *Frequency-resolved optical gating: the measurement of ultrashort laser pulses*, Kluwer Academic Publishers (2000).

[92] P. O'Shea et al., *Highly simplified device for ultrashort-pulse measurement*, Opt. Lett. 26, 932 (2001).

[93] G. Mourou, W. Knox, *A picosecond jitter streak camera*, Appl. Phys. Lett. 36, 623 (1980).

[94] A. Takahashi et al., *New femtosecond streak camera with temporal resolution of* 180 fs, Proc. SPIE 2116, 275 (1994).

[95] Y. Tsuchiya, A. Takeshima, E. Inuzuka, *Synchroscan streak camera*, SPIE Vol. 348, 245 (1982).

[96] C. Froehly, A. Lacourt and J. C. Vienot, *Notions de réponse impulsionnelle et de fonction de transfert temporelles des pupilles optiques*, J. d'optique 4, 183 (1973).

[97] M. Takeda, H. Ina and S. Kobayashi, *Fourier-transform method of fringe-pattern analysis for computer-based topography and interferometry*, J. Opt. Soc. Am. 72, 156 (1982).

[98] J. L. A. Chilla and O. E. Martinez, *Direct determination of the amplitude and phase of femtosecond light pulses*, Opt. Lett. 16, 39 (1991).

[99] L. Lepetit, G. Cheriaux and M. Joffre, *Linear techniques of phase measurement by femtosecond spectral interferometry for applications in spectroscopy*, J. Opt. Soc. Am. B 12, 2467 (1995).

[100] F. W. Helbing, G. Steinmeyer, U. Keller, *Carrier-envelope offset phase-locking with attosecond timing jitter*, IEEE J. Sel. Top. Quantum Electron. 9, 1030 (2003).

[101] Z. Li et al., *Fourth-order dispersion compensation for ultra-high power femtosecond lasers*, Opt. Commun. 357, 71 (2015).

[102] E. B. Treacy, *Optical pulse compression with diffraction gratings*, IEEE J. Quantum Electron. 5, 454 (1969).

[103] W. Stößel, *Fourieroptik*, Springer (1993).

[104] W. Lauterborn, T. Kurz and M. Wiesenfeldt, *Kohärente Optik*, Springer (1993).

[105] J. W. Goodman, *Introduction to Fourier optics*, 2nd edition, McGraw-Hill (1996).

[106] B. J. Sussman, R. Lausten, A. Stolow, *Focusing of light following a 4-f pulse shaper: Considerations for quantum control*, Phys. Rev. A 77, 043416 (2008).

[107] M. M. Wefers and K. A. Nelson, *Analysis of programmable ultrashort waveform generation using liquid-crystal spatial light modulators*, J. Opt. Soc. Am. B 12, 1343 (1995).

[108] A. V. Oppenheim, R. W. Schafer, *Discrete-Time Signal Processing*, 2nd edition, Prentice Hall (1998).

[109] C. Froehly, B. Colombeau and M. Vampouille, *Shaping and Analysis of Picosecond Light Pulses* in *Progress in Optics 20* ed. by F. Wolf, North Holland (1983).

[110] A. M. Weiner et al., *Programmable Shaping of Femtosecond Optical Pulses by Use of 128-Element Liquid Crystal Phase Modulator*, IEEE J. Quantum Electron. 28, 908 (1992).

[111] D. Zeidler et al., *Adaptive compression of tunable pulses from a non-collinear-type OPA to below 16 fs by feedback-controlled pulse shaping*, Appl. Phys. B 70, 125 (2000).

[112] M. Hacker et al., *Micromirror SLM for femtosecond pulse shaping in the ultraviolet*, Appl. Phys. B 76, 711 (2003).

[113] I. C. Chang, *Acousto-Optic Devices and Applications* in *Handbook of Optics Vol. II* ed. by M. Bass, McGraw-Hill (1995).

[114] C. Mai et al., *Pulse Shaping Methods for Laser-Induced Generation of THz Radiation at the DELTA Storage Ring*, Proc. of 9th International Particle Accelerator Conference, Melbourne, Australia, 1453 (2019).

[115] C. Mai et al., *Towards Arbitrary Pulse Shapes in the Terahertz Domain*, Proc. of 11th International Particle Accelerator Conference, Campinas, Brazil, 3977 (2021).

[116] D. Nölle et al., *Status of the Dortmund Electron Test Accelerator Facility*, Proc. of the 8th European Particle Accelerator Conference, Paris, France, 745 (2002).

[117] M. Tolan et al., *DELTA: Synchrotron light in nordrhein-westfalen*, Synchrotron Radiation News 16, 9 (2003).

[118] D. Schirmer, *Synchrotron radiation sources at DELTA*, DELTA Int. Rep. 001-05, Institute of Acceleratorphysics and Synchrotron Radiation, TU Dortmund University (2009).

[119] T. Weis, private communication (2019).

[120] M. Pedrozzi et al., *Status of the SLS preinjector*, in *PSI Scientific Report VII*, 8 (1999).

[121] A. Jankowiak et al., *Reconstruction of the 75 MeV Linac of the DELTA Synchrotron Radiation Facility*, Proc. of the 7th European Particle Accelerator Conference, Vienna, Austria, 636 (2000).

[122] K. Wille et al., *Initial experience with DELTA*, Proc. of 5th European Particle Accelerator Conference, Barcelona, Spain, 95 (1996).

[123] H. Gerke et al., *Das PETRA-Cavity*, DESY Int. Rep. PET-77/08 (1977).

[124] E. Weihreter, *Status of the European HOM-damped normal conducting Cavity*, Proc. of 11th Euroapen Particle Accelerator Conference, Genoa, Italy, 2932 (2008).

[125] R. Heine, P. Hartmann, T. Weis, *Characterization of the EU-HOM-damped normal conducting 500 MHz Cavity from the Beam Power Spectrum at DELTA*, Proc. of 10th European Particle Accelerator Conference, Edinburgh, Scotland, 2856 (2006).

[126] P. Hartmann et al., *DELTA Radiofrequency Systems*, DELTA Annual Report 2018.

[127] H. Huck, *Optimierung und Charakterisierung des Free Electron Lasers am Speicherring DELTA*, doctoral thesis, TU Dortmund (2009).

[128] J. Friedl, private communication (2020).

[129] J. Bergoz, *Current monitors for particle beams*, Nucl. Phys. A 525, 595 (1991).

[130] D. Martin et al., *Evaluation of Bergoz Instrumentation NPCT*, Proc. of 23rd Particle Accelerator Conference, Vancouver, Canada, 4021 (2009).

[131] S. Kötter, *Orbit correction and response analysis at DELTA*, doctoral thesis, TU Dortmund University (2022).

[132] R. H. Byrd et al., *A limited memory algorithm for bound constrained optimization*, SIAM J. Sci. Comput. 16, 1190 (1995).

[133] L. R. Dalesio et al., *The experimental physics and industrial control system architecture: past, present, and future*, Nucl. Instrum. Methods Phys. Res. A 352, 179 (1994).

[134] R. Coisson, F. de Martini, *Free-electron coherent relativistic scatterer for UV generation*, Phys. Quant. Elec. 8, 939 (1982).

[135] R. Prazeres et al., *Coherent harmonic generation in the vacuum ultraviolet spectral range on the storage ring ACO*, Nucl. Phys. A 272, 68 (1988).

[136] T. Tanikawa et al., *Spectral Measurement of VUV CHG at UVSOR-II*, Proc. of 1st International Particle Accelerator Conference, Kyoto, Japan, 2206 (2010).

[137] M. Höner, *Optical design and construction of a dedicated THz beamline at DELTA and study of laser-electron interaction*, diploma thesis, TU Dortmund University (2011).

[138] P. Ungelenk, *A new THz beamline at DELTA: Tracking simulations, mechanical design, assembly and first measurements*, diploma thesis, TU Dortmund University (2011).

[139] L. H. Yu, *Generation of Intense UV Radiation by subharmonically Seeded Single-Pass Free-Electron Lasers*, Phys. Rev. A 44, 5178 (1991).

[140] R. Molo, *Towards echo-enabled harmonic generation at FLASH1 and DELTA*, doctoral thesis, TU Dortmund University (2017).

[141] B. Büsing, *Teilchenoptische Auslegung und Entwicklung von Dipolkammern für die EEHG-basierte Kurzpulsquelle bei DELTA*, master's thesis, TU Dortmund University (2017).

[142] A. Meyer auf der Heide, *The DELTA Short-Pulse Source: Upgrade Plans from CHG to EEHG*, Proc. of IPAC2019, Melbourne, Australia, 1457.

[143] S. Khan et al., *SPEED: Worldwide first EEHG implementation in a storage ring*, Proc. of IPAC2023, Venice, Italy, 1061.

[144] D. Xiang and G. Stupakov, *Echo-enabled harmonic generation free electron laser*, Phys. Rev. ST Accel. Beams 12, 030702 (2009).

[145] G. Stupakov, *Using the Beam-Echo Effect for Generation of Short-Wavelength Radiation*, Phys. Rev. Lett. 102, 074801 (2009).

[146] K. Wille, *Synchrotron radiation sources*, Rep. Prog. Phys. 54, 1005 (1991).

[147] R. Bonifacio, R. Corsini, P. Pierini, *Theory of the high-gain optical klystron*, Phys. Rev. A 45, 4091 (1992).

[148] M. Huck, *Characterization of VUV pulses from the short-pulse facility at DELTA and steps towards pump-probe experiments*, doctoral thesis, TU Dortmund University (2015).

[149] M. Czerny, A. F. Turner, *Über den Astigmatismus bei Spiegelspektrometern*, Zeitschrift für Physik 61, 792 (1930).

[150] S. Hüfner, *Very High Resolution Photoelectron Spectroscopy*, Springer (2007).

[151] Diamond Materials, Freiburg, Germany, V100-D46-A50 CVD UHV diamond window, datasheet (2016).

[152] International Organization for Standardization (ISO), *International Standard ISO/IEC 14882:2014 – Programming Language C++*, Geneva, Switzerland (2014).

[153] P. Ungelenk, *Generation and detection schemes for laser-induced coherent terahertz radiation at the electron storage ring DELTA*, doctoral thesis, TU Dortmund (2015).

[154] M. Borland, *elegant: A Flexible SDDS-Compliant Code for Accelerator Simulation*, Advanced Photon Source, LS-287 (2000).

[155] W. R. Stevens, *UNIX Network Programming: Interprocess Communications*, Prentice Hall (1999).

[156] P. Ungelenk et al., *Temporal and Spectral Observation of laser-induced THz Radiation at DELTA*, Proc. of International Particle Accelertor Conference, Shanghai, China, 94 (2013).

[157] C. Mai, *Design and Construction of a Polarizing Interferometer for theDELTA Terahertz Beamline*, master's thesis, TU Dortmund University (2015).

[158] V. Vijayan, doctoral thesis in preparation.

[159] J. Murphy, S. Krinsky, R. Gluckstern, *Longitudinal wavefield for an electron moving on a circular orbit*, Part. Accel. 57, 9 (1997).

[160] C. Mai et al., *Observation of Coherent Terahertz Bursts during Low-Energy Operation of DELTA*, Proc. of 14th International Particle Accelerator Conference, Venice, Italy, 1061 (2023).

[161] M. Brosi, *In-Depth Analysis of the Micro-Bunching Characteristics in Single and Multi-Bunch Operation at KARA*, doctoral thesis, Karlsruher Institut für Technologie (2020).

[162] C. Evain et al., *Stabilization of the Bunch Position during the Control of the Microbunching Instability in Storage Rings*, Phys. Rev. Accel. Beams 26, 090701 (2023).

[163] M. Ries et al., *THz bursting thresholds measured at the metrology light source*, Proc. of 3rd International Particle Accelerator Conference, New Orleans, Louisiana, USA, 3030 (2012).

[164] U. Schade et al., *Cross-Correlation of THz Pulses from the Electron Storage Ring BESSY II*, Condens. Matter 5, 24 (2020).

[165] S. Wesch et al., *A multi-channel THz and infrared spectrometer for femtosecond electron bunch diagnostics by single-shot spectroscopy of coherent radiation*, Nucl. Instrum. Methods Phys. Res. A 665, 40 (2011).

[166] S. P. Davis, M. C. Abrams, J. W. Brault, *Fourier Transform Spectrometry*, Academic Press (2001).

[167] K. B. Howell, *Fourier Transforms* in *Transforms and Applications Handbook* ed. by A. D. Poularikas, CRC Press (2010).

[168] C. Mai et al., *Time-resolved Spectral Observation of Coherent THz Pulses at DELTA*, Proc. of 7th International Particle Accelerator Conference, Busan, Korea, 105 (2016).

[169] D. H. Martin, E. Puplett, *Polarised interferometric spectrometry for the millimetre and submillimetre spectrum*, Infrared Phyics 10, 105 (1970).

[170] J. C. G. Lesurf, *Millimetre-Wave Optics, Devices and Systems*, Taylor & Francis (1990).

[171] P. Thoma, *Ultra-fast $YBa_2Cu_3O_{7-x}$ direct detectors for the THz frequency range*, doctoral thesis, Karlsruher Institut für Technologie (2013).

[172] SHF Communication Technologies AG, *Datasheet SHF804 TL, Broadband Amplifier V003*, (2008).

[173] P. Ungelenk et al., *Studies of Ultrashort THz Pulses at DELTA*, Proc. 5th Int. Particle Accerator Conf., Dresden, Germany, 1936 (2014).

[174] C. Mai et al., *A Tunable Narrowband Source in the Sub-THz and THz Range at DELTA*, Proc. of 9th International Particle Accelerator Conference, Vancouver, Canada, 4534 (2018).

[175] A. S. Weling et al., *Generation of tunable narrow-band THz radiation from large aperture photoconducting antennas*, Appl. Phys. Lett. 64, 137 (1994).

[176] A. S. Weling and D. H. Auston, *Novel sources and detectors for coherent tunable narrow-band terahertz radiation in free space*, J. Opt. Soc. Am. B 13, 2783 (1996).

[177] S. Bielawski et al., *Tunable narrowband terahertz emission from mastered laser–electron beam interaction*, Nature Phys. 4, 390 (2008).

[178] C. Evain et al., *Laser-induced narrowband coherent synchrotron radiation: Efficiency versus frequency and laser power*, Phys. Rev. Special Topics - Accel. Beams 13, 090703 (2010).

[179] P. Ungelenk et al., *Continuously tunable narrowband pulses in the THz gap from laser-modulated electron bunches in a storage ring*, Phys. Rev. Accel. Beams 20, 020706 (2017).

[180] S. W. Jolly et al., *Spectral phase control of interfering chirped pulses for high energy narrowband terahertz generation*, Nat. Commun. 10, 2591 (2019).

[181] S. Kamada et al., *On the chirp of narrowband Terahertz pulses generated by photomixing with nonlinearly chirped laser pulse pairs*, Appl. Phys. Express 6, 032701 (2013).

[182] J. McMullen, *Chirped-pulse compression in strongly dispersive media*, J. Opt. Soc. Am. 67, 1575 (1977).

[183] S. W. Jolly, *Spectral phase manipulation of optical pump pulses for mJ-level narrowband Terahertz generation in PPLN*, doctoral thesis, Universität Hamburg (2017).

[184] T. Baumert et al., *Femtosecond pulse shaping by an evolutionary algorithm with feedback*, Appl. Phys. B 65, 779 (1997).

[185] A. Karar et al., *A Programmable Mode-Locked Fiber Laser Using Phase-Only Pulse Shaping and the Genetic Algorithm*, Photonics 7, 69 (2020).

[186] R. E. Ziemer, W. H. Tranter, *Principles of Communications: Systems, Modulation, and Noise*, Wiley (2015).

[187] H. Nyquist, *Certain topics in telegraph transmission theory*, Trans. AIEE 47, 617 (1927).

[188] C. E. Shannon, *A mathematical theory of communication*, Bell Labs Tech. J. 27, 623 (1948).

[189] G. Zhu et al., *Investigation of the thermal and optical performance of a spatial light modulator with high average power picosecond laser exposure for materials processing applications*, J. Phys. D: Appl. Phys. 51, 095603 (2018).

[190] G. Orlandi et al., *Bunch length and energy measurements in the bunch compressor of a free-electron laser*, Phys. Rev. Accel. Beams 22, 072803 (2019).

[191] C. J. Milne et al., *SwissFEL: The Swiss X-ray Free Electron Laser*, Appl. Sci. 7, 720 (2017).

[192] F. Frei, R. Ischebeck, *Electron Bunch Compression Monitors for Short Bunches – Commissioning Results from SwissFEL*, Proc. of 8th International Beam Instrumentation Conference, Malmö, Sweden, 578 (2019).

[193] P. Ball, *Water – an enduring mystery*, Nature 452, 291 (2008).

[194] F. Novelli, B. Guchhait and M. Havenith, *Towards Intense THz Spectroscopy on Water: Characterization of Optical Rectification by GaP, OH1, and DSTMS at OPA Wavelengths*, Materials 13, 1311 (2020).

[195] U. Kaatze, *The dielectric properties of water in its different states of interaction*, J. Solut. Chem. 26, 1049 (1997).

[196] C. Mai et al., *Observation of Coherent Pulses in the Sub-THz Range at DELTA*, Proc. of 6th International Particle Accelerator Conference, Richmond, USA 823 (2015).

[197] L. Stuerzebecher et al., *Pulse compression grating fabrication by diffractive proximity photolithography*, Opt. Lett. 39, 1042 (2014).

[198] D. F. Gordon et al., *Electro-optic and Terahertz diagnostics*, 14th Workshop on Advanced Accelerator Concepts, AIP Conference Proceedings 1299, 67 (2010).

[199] L. Rota et al., *KALYPSO: Linear array detector for high-repetition rate and real-time beam diagnostics*, Nucl. Instrum. Methods Phys. Res. A 936, 10 (2019).

[200] S. Funkner et al., *High throughput data streaming of individual longitudinal electron bunch profiles*, Phys. Rev. Accel. 22, 022801 (2019).

[201] B. Büsing et al., *Optics studies on the operation of a new wiggler and bunch shortening at the DELTA storage ring*, Proc. of 12th International Particle Accelerator Conference, Campinas, Brazil, 2772 (2021).

Acknowledgements

Das Gelingen dieser Arbeit hat von der Geduld, Unterstützung und Hilfe einiger Menschen profitiert, denen ich herzlich danke.

Ich bedanke mich bei Prof. Dr. Shaukat Khan für die Möglichkeit diese Dissertation in seiner Arbeitsgruppe anfertigen zu können. Mit beachtlichem Engagement war er zu jeder Zeit ein geschätzter Unterstützer, Diskussionspartner und Motivator. Ich danke Prof. Dr. Andreas Jankowiak dafür, dass er sich die Zeit nimmt, das Zweitgutachten zu erstellen.

Der Betriebsgruppe von DELTA danke ich für die zuverlässige Bereitstellung der Beschleunigeranlage. Vieles, das wie Zauberei anmutet, ist in Wirklichkeit dem beharrlichen Einsatz erfahrener KollegInnen zu verdanken.

Ich danke insbesondere Peter Ungelenk, Markus Höner und Robert Molo für die freundliche Aufnahme in die Arbeitsgruppe und ihre Beiträge zum Aufbau der Kurzpulsquelle. Meinem Weggefährten Arne Held danke ich für die interessanten Diskussionen und die stetige Hilfe beim Betrieb der Laserexperimente.

Große Unterstützung habe ich von den Koordinatoren und Teilnehmern der Workshop-Reihe zur longitudinalen Diagnostik erfahren. Speziell zu nennen sind hier Miriam Brosi, Franziska Frei, Christopher Gerth, Rasmus Ischebeck, Niels Neumann, Bernd Steffen und Johannes Steinmann.

Ich danke den von mir (mit-)betreuten Studierenden Linus Bölte, Max Bolsinger, Moritz Hagemeier, Lina Heidenreich, Marc Jebramcik, Merlin Kallenborn, Marcel Kebekus, Raffael Niemczyk, Boris Sawadski, Maximilian Schmutzler, Frederik Teutenberg und Dennis Zimmermann für ihre Hilfe.

Ich danke den Mitarbeitern der Firma Holoeye, Stefan Osten und André Klauß, sowie Marc Assmann und Bernd Berger vom Lehrstuhl für Experimentelle Physik 2 für die leihweise Bereitstellung von Flüssigkristallmodulatoren.

Dem Centrum für Entrepreneurship & Transfer (CET) der TU Dortmund und Provendis, der Patentvermarktungsgesellschaft des Landes NRW, danke ich für die Unterstützung bei den in dieser Arbeit entstandenen Patentanmeldungen. Dem Land Nordrhein-Westfalen,

dem Bundesministerium für Bildung und Forschung sowie der Deutschen Forschungsgemeinschaft danke ich für die Förderung und die deshalb guten experimentellen Bedingungen.

Ich danke Roman und Christian für Korrekturvorschläge und Diskussionen über diese Arbeit.

Meiner Familie und insbesondere Nora, Liv und Otis danke ich für die moralische Unterstützung und Ablenkung während der letzten Jahre.